ECAP-2016-023

Simulation of Alpha Particle Scintillation Light in Liquid and Gaseous Xenon with Respect to Surface Reflections

Master Thesis

for the attainment of the academic degree
Master of Science (M. Sc.)

submitted by

Reimund Bayerlein

September, 2016

performed at
Erlangen Centre for Astroparticle Physics
Friedrich-Alexander-Universität Erlangen-Nürnberg
under the supervision of PD Dr Thilo Michel and Prof Dr Gisela Anton

ERLANGEN CENTRE FOR ASTROPARTICLE PHYSICS

FRIEDRICH-ALEXANDER UNIVERSITÄT ERLANGEN-NÜRNBERG
NATURWISSENSCHAFTLICHE FAKULTÄT

At this stage of development
there is nothing more "honorable" and closer to the science
than the simulation leading to the detector optimization!
This is sexy!

Giorgio Gratta

Contents

Abstract

The nEXO experiment for the search for the neutrinoless double beta decay will be using Silicon Photomultipliers (SiPM) for the detection of vacuum ultraviolet (VUV) light at 175-178 nm. The SiPMs have to meet several requirements in order to provide sufficient energy resolution. A characterization of these devices is currently conducted at a cryostat set up in Erlangen. To estimate the contribution of reflections of the copper wall inside the cryostat a GEANT4 simulation is used. Understanding the influence of the geometry and especially its surface properties enables a correct calculation of the photon detection efficiency of the SiPMs.

1. Introduction

"What is matter made of?" – Is a century old question in physics and certainly one of the most fundamental ones. It has been bothering generations of scientists working in the most different fields of research. Thanks to early chemists like Robert Boyle the antique Greek idea of an atom as the elementary component of matter was revived. Some of the best known and most famous researchers have contributed to secure this concept like Daniel Bernoulli, John Dalton, Amedo Avogadro, James C. Maxwell and of course Albert Einstein to only name a few.

However, it quickly became clear that there exist smaller and even more fundamental particles providing a great play ground for physicists up until now. Atomic models by J.J. Thomson, Ernest Rutherford or Niels Bohr prepared the ground for great fields of research like *particle* and *nuclear physics* and lead to successful new theories like *quantum mechanics* – making the early 20th century one of the most exciting and pioneering periods in the history of physics. Theories have been improved, new models have been introduced. And since physicists have always loved smashing and breaking stuff to find out what's inside, a sheer "particle zoo" has been formed being able to explain an uncountable number of fascinating phenomena and interactions of the standard model and beyond.

One of these great milestones in particle physics is certainly the discovery of the *neutrino*. It was proposed by Wolfgang Pauli in 1930 as a hypothetical neutral particle and was at first called "the neutron". Its existence was verified by Reines (Nobel Prize 1995) and Cowan in 1956 using nuclear reactions as neutrino source. After that, a series of different experiments have been searching for unknown neutrino properties. Goldhaber performed a direct measurement of its helicity, while Lederman, Schwartz and Steinberger (Nobel Prize 1988) were able to proof the distinction between electron neutrino ν_e and muon neutrino ν_μ. Another very important experiment with impact on the neutrino picture was established by Wu et al. in 1956 providing evidence for the charge-parity (CP) violation in the lepton sector. The light neutrino family was completed by the discovery of the third neutrino flavour (tau neutrino ν_τ) in 2000 by the DONUT experiment. [Kod+01; Gri08; Sch97; Phy15]

The most recent achievement in neutrino physics is the detection of neutrino oscillations by Takaaki Kajita and Arthur B. McDonald showing that the neutrinos are massive particles [Phy15]. This has lead to a new era of interest in neutrino physics and opened new vistas in theoretical and experimental physics. One of them is the search for the neutrinoless double beta decay which could – if existent – prove the

Majorana nature of neutrinos, i.e. clarify if the neutrino is its own anti-particle. One mandatory prerequisite for this rare nuclear decay is a neutrino mass larger than zero. [GC+12]

Currently, there are several experiments all over the world trying to observe this decay which has far reaching implications on particle and nuclear physics beyond the standard model. One of them is the nEXO experiment using a liquid xenon (LXe) time projection chamber (TPC). The research group in Erlangen is contributing to the development of the detector by characterizing Silicon Photomultipliers (SiPMs) with regard to their applicability to the detection of scintillation light in xenon. A special test stand was developed for this purpose allowing for the operation of SiPMs in xenon gas at cryogenic temperatures. The planned next step is the liquefaction of xenon with this set-up.

The goal of this work is a detailed examination of the inward of the Erlangen set-up using GEANT4 simulations of scintillation light propagation inside the xenon cell. The influence of geometry and surface quality on the detector response and, therefore, on the characterization of SiPMs is investigated. In chapter 2 the theoretical basics on neutrinoless double beta decay are outlined together with an overview of currently operating experiments on that field of research. In this context, also the nEXO experiment is introduced. Chapter 3 comprises the characterization of SiPMs and explains the most important properties of the Erlangen set-up. A detailed description of the simulation as well as its capability and validity range is given in chapter 4. Eventually, chapter 5 describes the performance and analysis of the simulation and presents the results.

2. Theoretical Background and Motivation

2.1. The Search for the Neutrinoless Double Beta Decay

2.1.1. Introduction and Overview

For the last 20 years the search for the neutrinoless double beta decay ($0\nu\beta\beta$) has become a high priority task in neutrino and particle physics in order to understand the neutrino and the origin of its mass. Probably the most important reason for the increasing interest in this topic is the nobel prize winning discovery of the neutrino oscillations by Takaaki Kajita and Arthur B. McDonald showing that the neutrinos indeed have mass [Phy15]. Massive neutrinos are an essential requirement for the existence of $0\nu\beta\beta$ – a hypothetical, rare nuclear decay. A first but unconfirmed claim for its discovery was made by Klapdor-Kleingrothaus et al. in 2001 based on data from the Heidelberg-Moscow experiment using ^{76}Ge as decay isotope [KK+01]. It is still highly controversial [Aal+02] and was recently referred to as "strongly disfavored" by the GERDA experiment [Ago+16]. Since then new experiments have been designed using different approaches, isotopes and techniques in order to confirm or refute this claim. A potential discovery would have huge impact on theory as well as experimental physics, since it is the most practical way to decide if a neutrino ν is the same as its own anti-particle $\bar{\nu}$ – a so called *Majorana particle*. If ν and $\bar{\nu}$ are distinguishable they are called *Dirac particles*. Moreover, Majorana neutrinos would represent physics beyond the standard model of particles, because it would demonstrate the violation of lepton number conservation in physics phenomena (see section 2.1.3) [GC+12].

$0\nu\beta\beta$ provides further theoretical implications beyond the field of neutrino research since a Majorana fermion has never been observed before. Also, one can not pass over a link between Majorana neutrinos and the asymmetry of matter and antimatter in the universe. Via the *sea saw type I mechanism*, which is based on Majorana neutrinos, one can explain the dominance of matter over antimatter in the universe, if CP is violated in the leptonic sector. Finally, the discovery of $0\nu\beta\beta$ could help clarify the ordering of the neutrino mass eigenstates as well as determining the absolute mass scale [GC+12]. The scientific issue of neutrino mass and mass scale is briefly summarized in section 2.1.2.

However, the extraordinary long half-life of this decay provides an enormous challenge for any experiment. Recent results by KamLAND-Zen (2016) set a new lower limit for the half-life of the decay of ^{136}Xe of $1.07 \cdot 10^{27}$ yrs [Gan+16]. For comparison, the age of the universe is 17 magnitudes below that value [Col14b]. All important requirements for a potential measurement of $0\nu\beta\beta$ are outlined in 2.1.4 followed by a brief overview of some of the currently operating experiments searching for $0\nu\beta\beta$.

2.1.2. Massive Neutrinos and the Mass Scale

Information on massive neutrinos and the mechanism of neutrinoless double beta decay are taken from [GC+12], [GC+11], [Sch97], [Gri08] and [QV15] if not indicated differently.

Neutrinos are the lightest known elementary fermions and only observable via weak interaction. From experiments it is known that only three light active neutrino families exist ("light" means mass of the neutrino $< m_Z/2$, with m_Z the mass of the Z-boson). A neutrino of a certain flavour is associated with its corresponding charged lepton (electron e, myon μ or tauon τ). According to neutrino flavour oscillations the three *flavour eigenstates* that are participating in the weak interaction are different from the *mass eigenstates*. A weak eigenstate $|\nu_\alpha\rangle$ can be expressed via a linear combination of the three mass eigenstates $|\nu_i\rangle$ that are propagating through space-time:

$$|\nu_\alpha\rangle = \sum_{i=1}^{3} U^*_{\alpha i} |\nu_i\rangle \tag{2.1}$$

U is the 3×3, unitary *neutrino mixing matrix* and parametrized in two Majorana phases (α_{21}, α_{31}) and a CP-violating *Dirac phase* δ. At the current status of research the ordering of the three mass eigenstates is unknown and also the absolute mass of the lightest neutrino. Experimental results can, however, set some boundaries to the mass scale:
Observation of solar neutrinos and neutrinos from reactor experiments have probed the squared mass difference of the ν_1 and ν_2 state, which is called *solar mass splitting*: $|\Delta m^2_{sol}| = m_2^2 - m_1^2 = (7.58^{+0.22}_{-0.26}) \cdot 10^{-5}\,\text{eV}$. Atmospheric and accelerator based experiments predict the so called *atmospheric mass splitting* $|\Delta m^2_{\text{atm}}| = |m_3^2 - (m_1^2 + m_2^2)/2| = (2.35^{+0.12}_{-0.09}) \cdot 10^{-3}\,\text{eV}$. Figure 2.1 shows the two possible mass orderings: The case where the ν_1 state is larger than ν_3 is referred to as *inverted hierarchy*, the other way round it is called *normal hierarchy*. The flavour content (mixing) of each mass eigenstate is known from neutrino oscillations and due to cosmological observations an upper limit for the sum of all three neutrino masses can be established:

$$m_{\text{cosm}} = \sum_{i=1}^{3} m_i = 1.3\,\text{eV} \tag{2.2}$$

The importance of the investigation of the mass hierarchy lies in the goal of all experiments and theories on neutrinos to formulate a model to explain observed

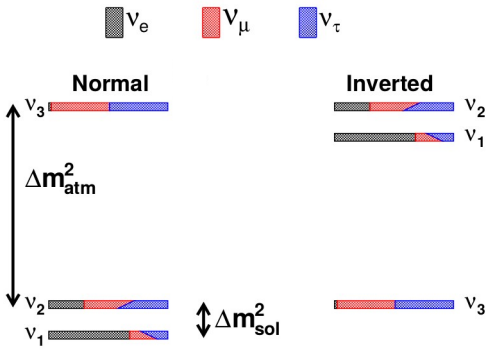

Figure 2.1.: The two possible neutrino mass hierarchies: Normal (left) and inverted mass ordering. From [QV15]

neutrino masses and mixing patterns and relate them to the charged lepton masses. A significant contribution to this attempt can be made by the discovery of the neutrinoless double beta decay.

2.1.3. Mechanism of Double Beta Decays

The neutrinoless double beta decay ($0\nu\beta\beta$) and the neutrino accompanied double beta decay ($2\nu\beta\beta$) are both rare nuclear transitions. They share some basic properties:

A nucleus with Z protons decays into a nucleus with $Z+2$ protons having two neutrons less but still the same mass number $A = Z + N$ (with N, number of neutrons). A fundamental requirement arising from energy conservation is that the decaying nucleus is less bound than the final one. An intermediate nucleus is having a higher atomic mass A than the other two so that a direct transition from the initial to the intermediate state is impossible. Because of higher nuclear pairing force only nuclei with even proton and neutron number can undergo $0\nu\beta\beta$ or $2\nu\beta\beta$ limiting the selection of possible candidates to 35.

The probability of $2\nu\beta\beta$ was first calculated by M. Goeppert-Mayer in 1935 from the Fermi theory of β-disintegration as the standard decay mode with two simultaneous beta decays with a half life of over 10^{17} yrs [GM35]:

$$(Z, A) \rightarrow (Z + 2, A) + 2\,e^- + 2\,\bar{\nu}_e \tag{2.3}$$

Four years later W. H. Furry proposed $0\nu\beta\beta$ by considering the Majorana theory where only the electrons have to be emitted giving rise to the transition probability [Fur39]:

$$(Z, A) \rightarrow (Z + 2, A) + 2\,e^- \tag{2.4}$$

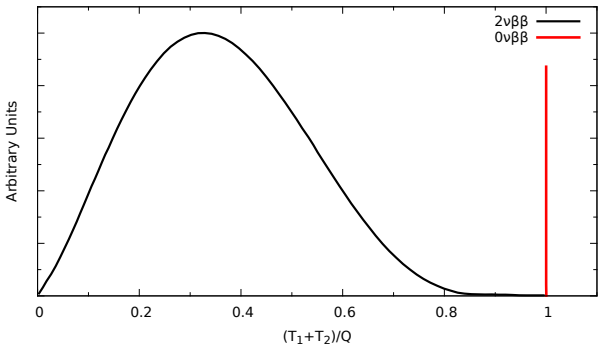

Figure 2.2.: Energy spectra of the sum of the electrons' kinetic energies in the $2\nu\beta\beta$ and $0\nu\beta\beta$ decay modes according to [GC+12].

While $2\nu\beta\beta$ is a possible decay within the standard model of particle physics $0\nu\beta\beta$ goes beyond that because of the violation of lepton number conservation by $\Delta L = +2$. Both processes are second order weak interactions with a rate proportional to G_F^4, where G_F denotes the Fermi constant as a measure of the strength of interaction. Another difference between $0\nu\beta\beta$ and $2\nu\beta\beta$ can be found in the energy spectrum $(T_1 + T_2)$ of the electrons: While the $2\nu\beta\beta$ spectrum is continuous due to the presence of neutrinos carrying away part of the energy the $0\nu\beta\beta$ spectrum is a mono-energetic line at the Q-value of the decay, which is only broadened by the resolution of the detector. A qualitative depiction of the spectra can be seen in figure 2.2.

According to *Schechter-Valle-Theorem* any $0\nu\beta\beta$ process induces an anti-neutrino-to-neutrino transition. This is also called *black box theorem* and implies that irrespective of the exact mechanism that is taking place a neutrinoless double beta decay implies the existence of Majorana neutrinos ν^M. This circumstance is briefly motivated in the following paragraph.

Figure 2.3 shows the standard $0\nu\beta\beta$ mechanism on quark level – the light Majorana neutrino exchange (other possibly existing mechanisms like *Majoron emission* are not further discussed in this scope). The parent nucleus emits a virtual W-boson. These bosons exchange Majorana neutrinos to produce the outgoing electrons. A right-handed anti-neutrino $\bar{\nu}_L$ that is emitted at one vertex is absorbed as a left-handed neutrino ν_L at the other one. This process demonstrates the two necessary conditions for $0\nu\beta\beta$:

- **The neutrino must be its own anti-particle:** $\nu = \bar{\nu} = \nu^M$. At the first vertex the neutron undergoes a single beta decay emitting an anti-neutrino $\bar{\nu}$ which has to be absorbed by the other neutron at the second vertex as a neutrino ν. This is only possible if neutrino and anti-neutrino are identical.
- **The neutrino must be massive.** Since the weak interaction only couples to left-handed fermions (helicity $H = -1$) and right-handed anti-fermions ($H = +1$)

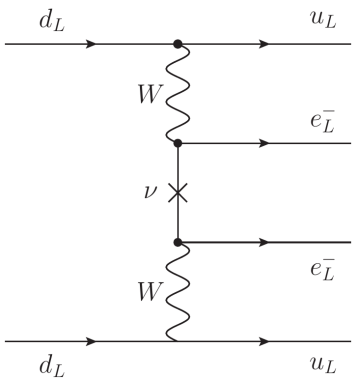

Figure 2.3.: Feynman graph of the neutrinoless double beta decay on quark level showing the standard mechanism based on light Majorana neutrino exchange. d stands for down-quark and u for up-quark respectively while the L indicates the helicity (left-/right-handed). From [GC+12]

due to maximum CP violation, neutrino and anti-neutrino must have different helicity. This means that even if the neutrino is a Majorana particle the decay could not happen for *massless* neutrinos. For $m_\nu > 0$, however, the helicity depends on the reference frame of the observer. For massive particles with velocity $v < c$ a frame B can be found so that $v_B > v$ and in which the helicity is "flipped" (has opposite sign). For $m = 0$ the velocity of the particle is equal to c and no such frame can be found.

Therefore, the above conditions imply a violation of lepton number conservation as well as a helicity-flip. The amplitude of this process is proportional to the *effective Majorana neutrino mass*:

$$m_{\beta\beta} \equiv \left| \sum_{i=3}^{3} m_i \, U_{ei}^2 \right| \tag{2.5}$$

The rate is only non-zero for massive neutrinos and proportional to the square of $m_{\beta\beta}$:

$$\frac{1}{T_{1/2}^{0\nu}} = G^{0\nu}(Q, Z) |M^{0\nu}|^2 \, \frac{m_{\beta\beta}^2}{m_e^2} \tag{2.6}$$

where m_e denotes the electron mass and $G^{0\nu}(Q, Z)$ is a phase space factor depending on the Q-value of the transition and also the nuclear charge Z. It can be calculated analytically whereas the nuclear matrix element (NME) $|M^{0\nu}|^2$ must be evaluated using nuclear models. The NME contains nuclear structure effects and is strongly model dependent. For an experiment with a non-zero $0\nu\beta\beta$ rate the effective Majorana neutrino mass can be obtained. Therefore, the Majorana neutrino exchange in $0\nu\beta\beta$ yields information on the absolute neutrino mass scale, since $m_{\beta\beta}$ is directly connected to m_i. Figure 2.4 shows the $m_{\beta\beta}$ as a function of the mass of the lightest neutrino m_{light}. The green band represents the inverted hierarchy ($m_{\text{light}} = m_3$) and the red one the normal

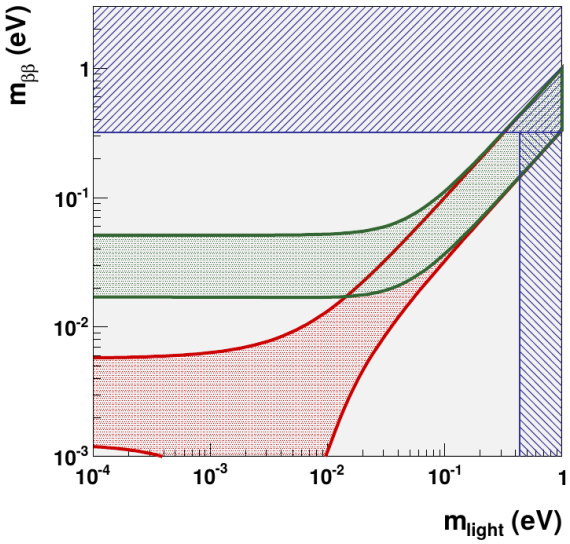

Figure 2.4.: The effective Majorana neutrino mass $m_{\beta\beta}$ as a function of the mass of the lightest neutrino m_{light}. The green (red) band coresponds to the inverted hierarchy (normal hierarchy). From [GC+12]

hierarchy ($m_{\text{light}} = m_1$) respectively. Cosmological observations set a boundary for the lightest neutrino mass at $m_{\text{light}} < m_{\text{cosm}}/3 \approx 0.43\,\text{eV}$, the effective mass is limited due to $0\nu\beta\beta$ constraints to 0.32 eV. The width of the bands originates in uncertainties in the measured oscillation parameters and unknown phases in the neutrino mixing matrix U.

A current upper limit for $m_{\beta\beta}$ of $61 - 165\,\text{meV}$ is set by KamLAND-Zen [Gan+16] close to the inverted hierarchy band. If the inverted ordering is realized in nature the very next generation of $0\nu\beta\beta$ experiments might be able to decide if a neutrino is a Majorana particle.

2.1.4. Experimental Requirements

The discovery of $0\nu\beta\beta$ would be a substantial breakthrough in particle physic providing the proof of Majorana nature of neutrinos and demonstrating the violation of lepton number conservation. However, specific experimental requirements must be fulfilled to compensate for the extremely long half-life. A very large mass $M_{\beta\beta}$ of the emitting isotope (with molar mass $W_{\beta\beta}$) is needed as well as sufficiently long measurement time in the range of years. The number $N_{0\nu\beta\beta}$ of decays that can be detected within a measurement period t depends on the half-life of the decay $T^{0\nu}_{1/2}$ as follows:

$$N_{0\nu\beta\beta} = \log 2 \cdot \frac{M_{\beta\beta} \cdot N_{\text{A}}}{W_{\beta\beta}} \cdot \varepsilon \frac{t}{T^{0\nu}_{1/2}} \tag{2.7}$$

with N_{A}, Avogadro's constant and ε the signal detection efficiency of the detector. In the case of ^{136}Xe the molar mass of the isotope is 135.9 g/mol [GC+11]. A scalability

to large masses is therefore an important property of a successful detector and xenon based experiments may provide the best prerequisites in fulfilling this requirement. In addition to the long exposure time and the large mass the detector needs a very high detection efficiency ε.

Furthermore, background (BG) suppression is crucial, since any radioactive processes could superimpose the signal peak or mimic false $0\nu\beta\beta$ decays. $2\nu\beta\beta$ and $0\nu\beta\beta$ are only distinguishable by energy measurements. This implies that a good energy resolution – usually given as an energy window ΔE around the Q-value – is mandatory for a potential $0\nu\beta\beta$ discovery. Depending on how well the above mentioned qualifications are fulfilled, one can give a value for the sensitivity for probing the effective Majorana neutrino mass:

$$m_{\beta\beta} \propto \sqrt{\frac{1}{\varepsilon}} \left(\frac{c \cdot \Delta E}{M_{\beta\beta} \cdot t} \right)^{1/4} \tag{2.8}$$

c is the BG rate in counts/(keV $\cdot$ kg $\cdot$ yr) and depends on ΔE and the active mass (in fact the distribution of BG throughout the volume containing the active mass). This includes especially contributions from radioactive contaminations in the surfaces or signals induced by external sources. Equation 2.8 allows a comparison of different methods and experiments regarding their sensitivity. In the scope of $0\nu\beta\beta$ experiments the term *sensitivity* does not include an experimental ability to actually measure the decay but exclude a certain region where it is not to be found and, therefore, sets a specific limit for the discovery. This is especially important, if in the worst case no event is detected. The experiment or the measurement method is not counted as failure, because at least a region in the parameter space can be excluded and existing limits can possibly be "pushed". [GC+12; GC+11]

In the following paragraph a few currently operating experiments will be outlined together with the sensitivity they are able to achieve.

2.1.5. Current Double Beta Experiments

As a common working principle all experiments use the detection of the electrons coming from $0\nu\beta\beta$. The electrons with the energy of the Q-value of the decay undergo scintillation. The detection of produced free charges, emitted photons or both is the common ground for all detector types that are outlined in the following. The physical process of scintillation is explained in chapter 4.3 in detail.

GERDA The **GER**manium **D**etector **A**rray located in the Laboratori Nazionali del Gran Sasso (LNGS) is using ^{76}Ge as potential $0\nu\beta\beta$ isotope. Naked germanium detectors are arranged in strings and immersed in pure liquid argon. They are surrounded by a vacuum insulated stainless steel cryostat of 8.9 m height and a diameter of 4.2 m. The whole cryostat vessel is placed inside a large water tank of about 10 m height that

serves as gamma and neutron shield and also as veto against cosmic rays together with Photomultipliers (PMTs) for the detection of Cherenkov light. Finally, plastic scintillators on top of the detector are used as muon veto. [Ber+05b; Ago+16; GC+12]

In GERDA Phase I a total active mass of 17.7 kg was used with 86 % isotopic enrichment in ^{76}Ge from the previous Heidelberg-Moscow experiment. A BG level of 0.06 ± 0.02 counts/(keV · kg · yr) could be achieved. A sensitivity of $2.4 \cdot 10^{25}$ yrs on $0\nu\beta\beta$ half-life was reached with an exposure of 21.6 kg·yrs. The experimental lower limit on the $0\nu\beta\beta$ half-life results in $2.1 \cdot 10^{25}$ yrs (at 90 % C.L.). Correspondingly, the limit on the Majorana neutrino mass is $m_{\beta\beta} < 200 - 400$ meV. GERDA Phase II is planned with 35 kg active mass and improved BG reduction allowing for an improvement of the half-life sensitivity by an order of magnitude and, thus, covering a large region of the inverted mass hierarchy. [Ago+16; GC+12]

KamLAND-Zen This experiment searches for $0\nu\beta\beta$ in ^{136}Xe using 13 tons of a xenon-loaded liquid scintillator containing ≈3 % by weight of xenon with an enrichment of 90.8 % in ^{136}Xe [Gan+16]. The dissolved xenon is placed in a balloon inside the active volume, the latter of which has about 1 kton mass in total. The balloon is made of highly radio-pure material to limit BG contributions and is transparent to enable efficient scintillation light collection for calorimetric measurements. With a total exposure of 504 kg · yr a lower limit for the half-life of the decay of ^{136}Xe of $T^{0\nu}_{1/2} > 1.07 \cdot 10^{27}$ yrs could be set. KamLAND-Zen has the currently best sensitivity on $0\nu\beta\beta$ half-life. This corresponds to an upper limit for $m_{\beta\beta}$ of 61 − 165 meV [Gan+12; Gan+16; GC+12].

The Enriched Xenon Observatory EXO-200 The currently operating EXO-200 $0\nu\beta\beta$ experiment is located in New Mexico, USA, and uses ≈110 kg liquid xenon (LXe) as active source and detection medium. The detection principle is a TPC (time projection chamber) where a simultaneous collection of light and charge signal enables a three dimensional signal reconstruction. Free electrons are drifted towards wire channels using a field strength of 376 V/cm, while the cathode is in the centre of the TPC and the actual collection happens at both ends of the chamber. The charge signal is created via induction in so called V-wires and charge collection in U-wires that are crossed at 60°. For the light detection 468 large area avalanche photo diodes (LAAPDs) are placed at each end of the TCP [Aug+12b]. The design is shown in figure 2.5.

Compared to the design of GERDA, EXO-200 is a monolithic detector which is an essential part of EXO's background rejection especially from surfaces. Hereby, it is taken advantage of the self-shielding property of xenon to define a very clean *fiducial volume* which only has very little background. Only events from that part of the detector are taken into account for further analysis. The 3D reconstruction allows to draw conclusions about the topological event structure: Events with an energy

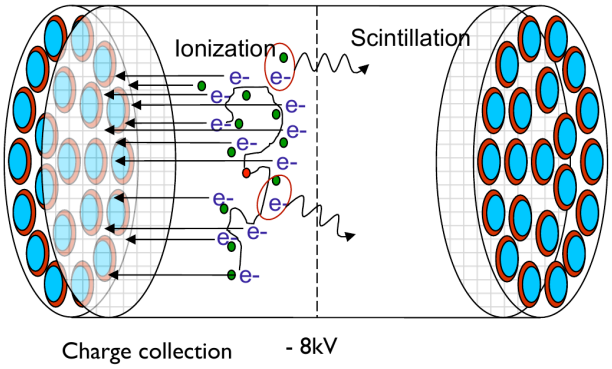

Figure 2.5.: TPC schematics of the EXO-200 experiment. Electrons are drifted towards the anode at each end of the detector, while the cathode is in the middle. Light collection is realized using LAAPDs at the front and back end of the TPC. From [Yia16]

deposition at only one position in the detector (*single site events*) can be discriminated from multiple energy deposits (*multi site events*). Therefore, background gammas with multiple scattering can be detected and rejected.

EXO-200 has provided the longest and most precise measurement of the $2\nu\beta\beta$ half-life of $(2.165 \pm 0.016^{\text{stat}} \pm 0.059^{\text{syst}}) \cdot 10^{21}$ yrs. At the end of the first run with an exposure of 100 kg·yrs the background in the region of interest (ROI: energy interval around the $0\nu\beta\beta$ peak in the spectrum) is $(1.7 \pm 0.2 \cdot 10^{-3})$ counts / (keV · kg · yr) and the limit for the half-life of $0\nu\beta\beta$ could be set to $1.1 \cdot 10^{25}$ yrs. The predicted half-life sensitivity for the current measurement period (Phase II) is $5.7 \cdot 10^{25}$ yrs (depicted in figure 2.7). [Yia16; Col14c; GC+12; Aug+12a]

2.2. The nEXO Experiment

2.2.1. Baseline Concept

nEXO is designed as a 5 ton liquid xenon time projection chamber (LXe TPC). Therefore, nEXO's general configuration is validated by the very successful double beta experiment EXO-200, since it is a monolithic detector making use of the self-shielding property of xenon as well. The TPC of 1.3 m in diameter and length is filled with xenon isotopical enriched of $> 90\,\%$ in ^{136}Xe. But not only will nEXO be about 25 times larger than EXO-200 but will also use a new TPC design with new detection concepts and a highly enhanced sensitivity. The experiment will be located underground in SNOLAB, Canada in a depth of 6000 meter water equivalent to shield from cosmic radiation. In contrast to EXO-200 – having the cathode in the middle of the TPC – nEXO uses a single drift volume with a strong electric field to accelerate free electrons towards the anode where charge collection via read-out tiles takes place. Behind the field-shaping rings at the TPC barrel Silicon Photomultipliers (SiPMs) are located for the purpose of light collection. By combining charge and light measurements a three

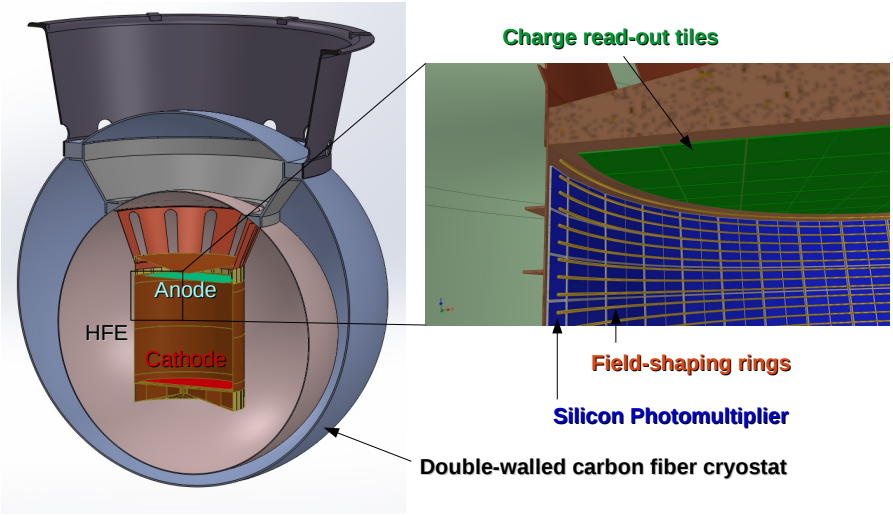

Figure 2.6.: The nEXO time projection chamber filled with 5 tons of liquid xenon. From [Yia16]

dimensional signal reconstruction is possible similar to EXO-200. The whole xenon chamber is placed inside a double-walled vacuum insulated cryostat using the cooling liquid HFE. A large water tank surrounding the cryostat serves as an additional shield from cosmic rays. Figure 2.6 shows the schematic design of the experimental set-up. [Yia16; Lic16]

2.2.2. Expected Sensitivity

The predicted energy resolution of nEXO is $\frac{\Delta E}{E} < 1.0\,\%$ at 2.458 MeV (Q-value of the decay, [Ost+15]). With 5 years of operation the half-life sensitivity is aimed to be $T^{0\nu}_{1/2} > 10^{28}$ yrs. nEXO is expected to cover the full range of the inverted hierarchy after 10 years of measurement time. The calculated background index is in the range of 10^{-5} counts / (kg · keV · yr). A possible improvement to the sensitivity could be achieved by tagging the daughter nuclide ^{136}Ba which constitutes a potential upgrade to the TPC design. The predicted $m_{\beta\beta}$ sensitivity is shown in figure 2.7 as a function of the lightest neutrino mass m_{light}. The red band corresponds to the normal and the blue band to the inverted mass ordering respectively. Also shown is the sensitivity of the currently operating EXO-200 experiment. nEXO's sensitivity will exceed the one achieved by EXO-200 by about an order of a magnitude. [Yia16; Lic16]

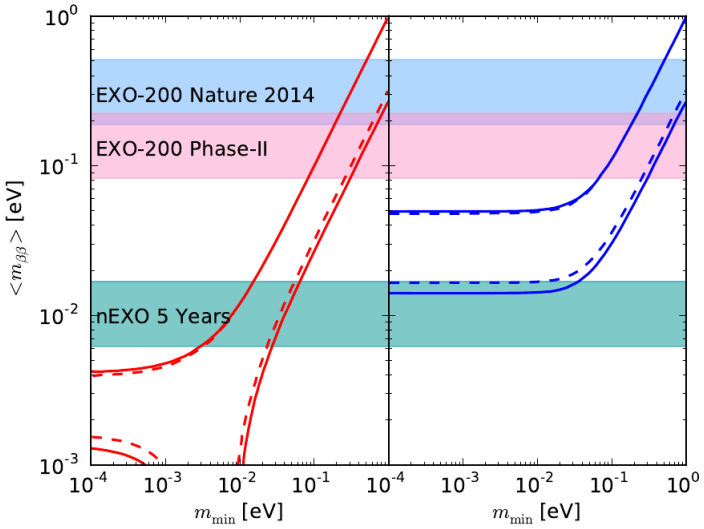

Figure 2.7.: $m_{\beta\beta}$ sensitivity of EXO-200 and nEXO as a function of the lightest neutrino mass m_{light}. The red band corresponds to the normal mass hierarchy, the blue one the inverted ordering. From [Col16]

2.2.3. Specific Technical Requirements

In order to detect $0\nu\beta\beta$ that has such a great half-life, an experiment needs to fulfil a large number of specific requirements to achieve the necessary sensitivity. In nEXO some of the essential demands that are formulated in equation (2.8) are met by a large active xenon mass with enriched ^{136}Xe, a large measurement time of up to 10 years and a good energy resolution, as mentioned above. Two other mandatory ingredients – background suppression and detection efficiency – are outlined in this paragraph together with their technical implementation.

Although nEXO has much better background suppression than EXO due to the improved volume-to-surface ratio, contributions from $2\nu\beta\beta$ decay mode as well as ^{222}Rn and ^{214}Bi on the cathode must be taken into account. For instance, high radio purity of silicon is an essential requirement for the applicability of SiPMs as photon detectors in nEXO. The detection efficiency consists on the one hand of the efficiency to collect drifted charges and on the other hand to detect the scintillation light. In a reaction with impurities in the xenon free electrons can form negative ions and are then not able to contribute to the charge signal. The inverse attachment rate of electrons to these impurities is called *electron lifetime* τ. Together with the strength $|\mathbf{E}|$ of the applied electric field this quantity is used to describe the electron's attenuation length in a medium which is a measure for the travelled distance between liberation and interaction (e.g. ion formation) of the electron [AD10]:

$$\lambda_{\mathrm{att}} \propto |\mathbf{E}| \cdot \tau$$

In nEXO a high attenuation length is realized with a field strength of about 50 kV/cm and high xenon purity providing an electron lifetime of $\tau > 10$ ms. Charge collection at the anode is performed using quadratic read-out tiles consisting of 30×30 channels each of which is formed by a metallized strip on fused silica.

SiPMs located at the barrel behind the field-shaping rings detect the scintillation light. The reason these devices are chosen instead of LAAPDs (used in EXO) or PMTs is that SiPMs are expected to have low radio active content and a higher gain. To some extend EXO's limited resolution is due to noise in the photo detector channels while SiPMs have the potential to achieve a much higher signal-to-noise ratio with a noise level of less than 1 photon equivalent. Besides low dark count rate and high radio purity of silicon, other quantities must be optimized for a reliable application for nEXO – above all the *photon detection efficiency* (PDE) and good timing resolution. Of course, also the usability in LXe must be ensured and tested. [Ret16; Ost+15]
An overview and explanation of all requirements is given in 3.1.2.

The nEXO experiment is currently in research and development (R&D) and not all the requirements are fulfilled, yet. Currently 27 institutes and universities are doing research to improve photo detection, charge collection or the TPC design and the cryostat set-up. In this context it is also necessary to test silicon photomultipliers of different manufacturers for their applicability in nEXO. A characterization of SiPMs with regard to the above mentioned requirements is performed in several test stands throughout the nEXO collaboration, one of which is located in Erlangen, Germany. The test set-up and the principle of determining the PDE of a SiPM is outlined in the following chapter. Beforehand, the working principle of SiPMs is illustrated together with necessary properties for their use in nEXO. Chapter 3 also explains the necessity of a simulation for the use of PDE determination.

3. Characterization of Silicon Photomultipliers

3.1. Introduction to Silicon Photo Multipliers

3.1.1. Design and General Functionality

A Silicon Photomultiplier (SiPM) is a pixelized single photon detection device where each pixel is an Avalanche Photodiode (APD) operated in geiger-mode [Din13]. An APD is a variation of a *pn*-junction photo diode with a reverse-biased voltage supply creating an electric field in the vicinity of the junction. When an optical photon is absorbed and an electron-hole pair is created in the absorption layer via photo-electric effect electrical breakdown occurs. The electron (or the hole) is accelerated in the electric field and can create secondary electron-hole pairs in a process called *impact ionization* [Aul+02]. These secondaries are accelerated as well and an avalanche is triggered. A gain in the order of 10^6 is possible comparable to a common Photomultiplier Tube (PMT) enabling single photon detection. That is possible because an APD is operated a few volts above the breakdown voltage – the point where a *pn*-junction becomes conductive:

$$U_{\text{Bias}} = U_{\text{Break}} + U_{\text{Over}}$$

This is called *geiger mode*. The advantages lie in a very fast signal rise time of nanoseconds or even less and in the reduction of noise from the multiplication process of the electron-hole pairs. A SiPM has about 1000 micro cells per mm^2 where each pixel consists of a photo cathode with a quenching resistor in series to interrupt the avalanches. The high uniformity of the pixels ensures a constant breakdown throughout all cells and, therefore, results in single photon resolution.

One drawback of SiPMs is the high thermal noise at room temperature which causes a dark count rate between 100 kHz and up to several MHz. However, dark count drops rapidly with decreasing temperature. The biggest advantages are the low operating voltage of 20 till 70 volts compared to a PMT with a power supply in the order of 1 keV, the compact dimensions of SiPMs and their independence of magnetic fields. [Eck+10; Aul+02]

In figure 3.1 the design of a SiPM developed by Ketek is depicted. The anti reflective layer maximizes the transmission of light, mostly for a certain wavelength range [Keta].

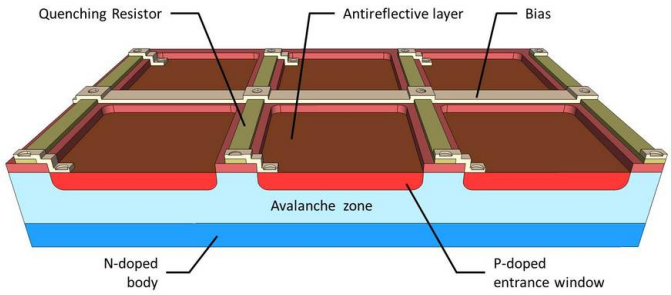

Figure 3.1.: Schematic illustration of a SiPM by Ketek. From [Ketb]

Two further effects have to be considered, though, that play an important role in the characterization of SiPMs (from [Eck+10]):

Cross-talk: During an avalanche in one pixel a few photons are randomly emitted due to recombination of electron-hole pairs. In a fraction of cases one of these photons can be caught by a neighbouring pixel and trigger another avalanche leading to an additional signal.

After-pulsing: If the silicon has a defect in the lattice an electron from an avalanche can be caught and trapped there. In a subsequent release it causes another delayed avalanche.

Both effects are summarized within the term *correlated avalanches* and have to be taken into account in the experiment and especially in the analysis of the produced data. The probability for correlated avalanches decreases with temperature. Cross-talk can be limited by *trenches* that are placed between the pixels while after-pulsing depends on the purity of the silicon. Calculating the probability for cross-talk and after-pulsing is essential for SiPM characterization and the determination of the correct photon detection efficiency (PDE), the last one of which will be discussed in 3.1.3 and 3.3.

3.1.2. Required Characteristics for the nEXO Experiment

Since high energy resolution is necessary for nEXO to achieve maximum sensitivity, also the SiPMs have to meet certain requirements to make them a reliable component of the experiment. The most important characteristics are outlined in this section (from [Ost+15] and [Ret16]):

High Radiopurity: Any radioactive content in the Silicon material would contribute to the background and must therefore be limited as well as possible. Compared to other sources like the vessel itself the SiPMs must give only minor contributions. The current guideline sets a limit to the specific activity at values in the order of

$\approx 10\,\mu$Bq/kg for ^{232}Th and ^{238}U which can not be fulfilled by other photon detectors like PMTs or LAAPDs as they are used in EXO-200.

Dark count rate: As mentioned above thermal noise is a big issue at room temperature and only decreases for lower temperatures. The requirement for nEXO is a dark count rate of no more than $50\,\mathrm{Hz/mm^2}$. A value that can be achieved at the temperature of liquid xenon i.e. lower than 165.05 K (=-108.1 °C) at 1 atm [AD10]. This automatically leads to another important necessity:

Compatibility with liquid xenon: SiPMs and all other instruments and materials in the vessel must have very low out-gassing levels, since any pollutants will limit the electron life time in the TPC, which is necessary due to the potentially long drift distance towards the anode. SiPMs must therefore be tested for their applicability in LXe. Furthermore, solutions with additional coatings or packaging materials like wavelength shifters or anti-reflective coatings are disfavoured because of their higher risk to be unsuitable for the operation in noble gas detectors compared to bare detectors.

Suitable detector size and electronics: Since most parts of the inward of the TPC will be covered by SiPMs a lot of read out channels and feedthroughs are needed. In order to limit their number the size of one single detector should be at least $1\,\mathrm{cm^2}$. The maximum size is limited by the increasing noise scaling with the capacitance per channel. Timing resolution is handicapped by higher capacitance due to slower signals. So, a capacitance less than $50\,\mathrm{pF/mm^2}$ is needed as well.

Probability of correlated avalanches: Cross-talk and after-pulsing cause additional, correlated avalanches contributing to the signal. Their probability must be limited to 20 % so that they will not influence the energy resolution of the whole detector.

Photon detection efficiency (PDE): The efficiency of the SiPMs for the detection of scintillation light at 175-178 nm should be at least 15 % to be able to achieve a desired overall detection efficiency for scintillation light in nEXO of 10 %. The PDE is discussed in more detail in the following section.

3.1.3. Definition of the Photon Detection Efficiency

The information in this section is mainly based on [Eck+10] if not indicated differently.

The photon detection efficiency, or short PDE, is a probability for an incoming photon of wavelength λ to be detected by the SiPM. This quantity is strongly wavelength dependent and is in general defined as

$$PDE(\lambda) = \epsilon_{\mathrm{Geo}} \cdot \mathrm{QE}(\lambda) \cdot \epsilon_{\mathrm{Trigger}} \ , \tag{3.1}$$

where the three constituent factors are:

- **the geometric efficiency** ϵ_{geo} (also called *geometric fill factor*) describing the fraction of active to total area. That means that not the whole SiPM surface is sensitive to photons but a significant fraction is occupied by trenches, circuit path for bias voltage and the quenching resistors (compare figure 3.1). This factor can vary a lot between different SiPM models. *Hamamatsu Photonics* for instance quantify the geometric efficiency of their models in a wide range of 30-80 % [Sla16].
- **the quantum efficiency QE** which is the probability that an incident photon generates an electron-hole pair and depends on the wavelength λ.
- **the trigger probability** $\epsilon_{\text{Trigger}}$ that is a combined likelihood of electron and hole to initiate an electric breakdown. That means every created electron-hole pair triggers an avalanche only with a certain probability.

The PDE as defined in equation 3.1 basically describes the fraction of incident photons that is actually detected. Therefore, the PDE can also be expressed as follows [Yan+14]:

$$PDE = \frac{N_{\text{Detected}}}{N_{\text{Incident}}} \tag{3.2}$$

which makes it a quantity that can be measured with a set-up like the one described in the following sections 3.2 and 3.3. Note that the number of detected photons N_{Detected} is the number of photons that were captured by the SiPM and causing a signal minus the number of photons N_{Dark} representing the dark count, i.e. the photons detected by the SiPM when operated in total darkness [Yan+14]:

$$N_{\text{Detected}} = N_{\text{SiPM}} - N_{\text{Dark}}$$

3.2. Design Properties of the Erlangen Set-Up

In the following paragraphs the configuration of instruments is introduced which is used for the characterization of silicon photomultipliers in gaseous Xenon at cryogenic temperatures. At the time this work was created gas at about -100 degrees was used in the experiment. Therefore, the main focus in this work and especially of the programme explained in chapter 4 lies on the simulation of the processes in gaseous xenon, although the simulation is also capable of treating the liquid case (see chapter 4.4).

The experimental set-up shall provide a cooled chamber filled with gaseous xenon which hosts the required electric instruments for the characterization of SiPMs. A reliable cooling system that ensures stable temperatures, a gas system with feed-throughs for

read out electronics and a thermally shielded xenon cell are required. The inward of the cell should contain a reasonable set-up for SiPM characterization and a light source producing vacuum ultra-violet (VUV) light in xenon. It will be introduced in section 3.2.2.

3.2.1. Cryogenic Set-Up

The whole cryostat contains of a vacuum-insulated chamber in which the xenon cell is placed and that provides some thermal shielding from the outside. Figure 3.2 shows the whole set-up as a computer-aided design (CAD). The xenon cell itself is mostly separated from the outer vessel and the only points of contact are at the top and lower end of the outer vacuum chamber. The cell is wrapped in a metallized film based on polyethylene terephthalate to shield from infrared radiation. In order to cool the system to cryogenic temperatures an aluminum rod of 8 cm diameter is used that is placed in liquid nitrogen. The rod is connected to a copper rod which is finally connected to the bottom of the xenon chamber. The use of two rods was necessary due to the transition from the external air to the insulating vacuum. A binary heating system placed around the copper rod regulates the temperature and keeps it constant with a deviation of less than 1°C. At the top of the outer vacuum vessel the gas inlet system and the pumps connect to the outer metal body. The xenon is flowing from the top downwards into the system through a metal pipe.

3.2.2. Design and Inward of the Xenon Cell

While the outer wall of the xenon cell is made of stainless steel the inward is entirely made of copper allowing for a small temperature gradient throughout the cell. Inside this copper cup all further instruments for the SiPM characterization are placed. The cell is depicted in figure 3.4 and consists of the following main parts:

- **Photomultiplier tube as reference**
  This photon detection device, that is commonly abbreviated with PMT, is basically an evacuated tube with an entrance window for photons. Incoming light creates an electron on the photocathode via the external photoelectric effect which is then accelerated towards a dynode. Secondary electron emission causes a multiplication of the first electron before they get accelerated to further dynodes. After a cascade of dynodes all emitted electrons get collected by the anode at the end of the tube and create a signal roughly proportional to the amount of incident light [K.K07].
  The reference PMT must have a well-known *photon counting efficiency*[1] to be able to compare the photon fluxes between SiPM and PMT which is the important quantity for PDE determination (details on the exact approach will be given in section 3.3). The PMT used in this set-up is the model R8520-406 by Hamamatsu Photonics K.K. and has a measured quantum efficiency of

[1] Also simply called *detection efficiency*. These terms were adapted from [K.K07]

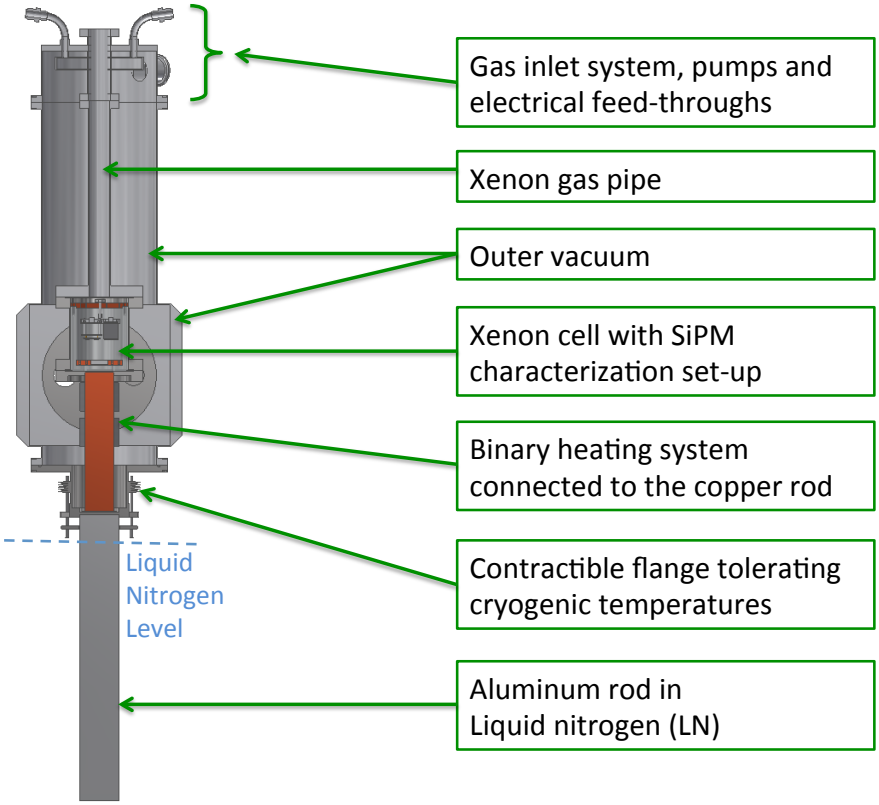

Figure 3.2.: Design of the cryostat used for SiPM characterization in cold xenon gas.

QE= 32.1 % which is defined as the ratio between the number of photo electrons emitted from the photocathode and the number of incident photons. The photon counting efficiency is expressed by the following relation [K.K07]:

$$\varepsilon_{\mathrm{PMT}} = \mathrm{QE}(\lambda) \cdot \varepsilon_D \ , \tag{3.3}$$

where ε_D denotes the collection efficiency of the dynodes, for which the manufacturer provides a value of about 70 %. The sensitive area of this PMT has a size of $20.5 \times 20.5\,\mathrm{mm}^2 = 420.25\,\mathrm{mm}^2$. It is calibrated for the detection of VUV scintillation light in liquid and gaseous xenon [Ham; Apr+12].

- **Silicon Photomultiplier and amplifier board**
  Next to the PMT the SiPM that is to be examined is located on a board made of the flame retardant material FR-4. Interchanging of SiPMs and its board is possible enabling the test of different types of SiPM in one set-up. The simulation in this work implements a SiPM from Ketek (model PM3350) which has a size of $3.0 \times 3.0\,\mathrm{mm}^2$, but is coated with Lumogen – a wavelength shifter. As a matter of fact these SiPMs were optimized for blue light and therefore have a maximum sensititivity at around 420nm. The PDE is therefore strongly wavelength dependent [Ketc]. For that reason, a wavelength shifter is used that absorbs an incoming photon and re-emits it with a different wavelength – ideally close to the most sensitive range. The actual size of this Lumogen coated SiPM could then be determined to be $3.6 \times 3.6\,\mathrm{mm}^2 = 12.96\,\mathrm{mm}^2$ using a calliper square and was then implemented with these measures (see section 4.2.2).

- **Hardware**
  Both detectors are held in place by a teflon holder attached to an aluminum spacer which is replaceable by longer or shorter versions. The variable space is used to adjust the distance between the radioactive source and the detectors and therefore to increase or decrease the light yield on the detectors. This feature was assembled because it could not be estimated beforehand what the ideal distance between light source and detectors was and with an interchangeable spacer optimization is possible without large effort.

- **Alpha source**
  The scintillation light that is to be detected by the SiPMs is created by alpha particles of three different energies coming from a radioactive source at the bottom of the chamber. The source consists of Americium, Californium and Plutonium in different proportions. The source has a circular, flat form with a diameter of about 5 mm and is covered with a foil reducing the alpha energy by about 1 MeV. The contents of the source and the corresponding measured alpha energies of the isotopes are listed in table 3.1. The source is placed on top of an aluminum holder that fits in the hole in the bottom of the cell that can be seen in the CAD drawing 3.4. The contributions of the different alpha particle energies are investigated in 4.4.

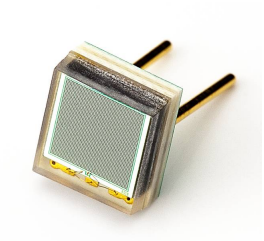

Figure 3.3.: Silicon Photomultiplier by *Ketek GmbH* model PM3350. One of the devices that was characterized with this set-up.

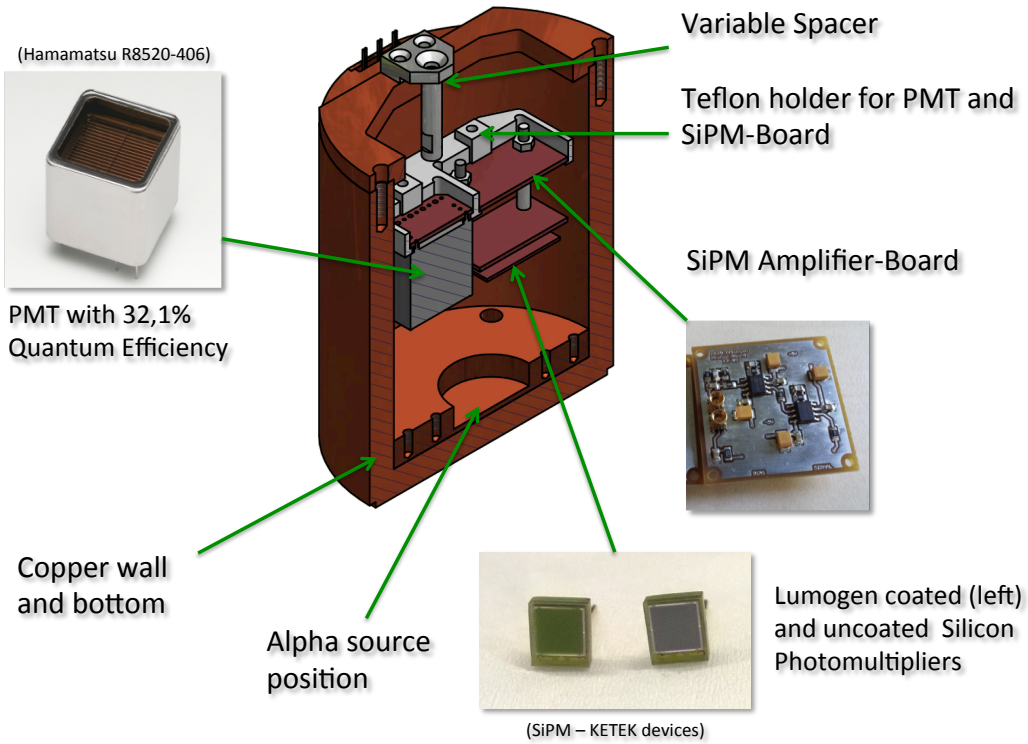

Figure 3.4.: The inward of the Xenon cell with its components: SiPM, PMT and alpha source.

Measured Energy	Isotope	Measured Relative Activity
4.15 MeV	^{239}Pu	40.5 %
4.48 MeV	^{241}Am	47.4 %
4.8 MeV	^{244}Cm	12.1 %

Table 3.1.: Energy of the different alpha particles, the decay isotope and their contribution to the total activity.

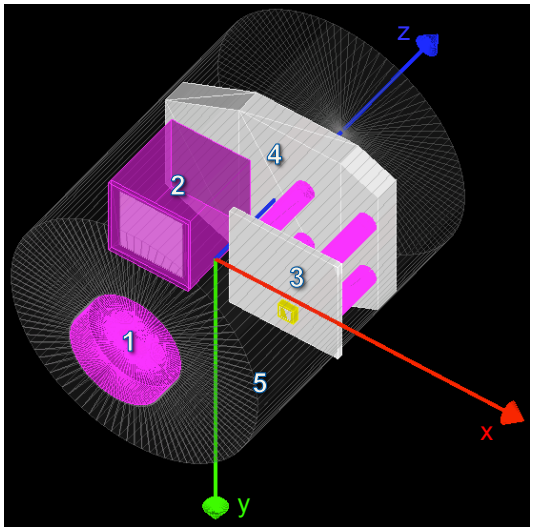

Figure 3.5.: The xenon cell as implemented in GEANT4 – 1: Aluminum holder with alpha source. 2: PMT. 3: SiPM and board. 4: Teflon holder. 5: Xenon gas/liquid (can easily be changed in the simulation). The surrounding copper cylinder was hidden in this representation to improve the visibility of the xenon and the equipment inside the chamber.

The xenon cell and its inward was implemented in GEANT4 for the simulation. The whole structure of the code will be outlined in section 4 in much detail. The measures of all parts and their location are entered as exactly as possible with a precision of up to 0.1 mm in order to match the real experiment. This counts especially for size and position of the detectors and their distance to the source. The teflon holder and the spacers which are above PMT and SiPM were implemented as well, but some details were neglected. It was assumed that contributions to the signals originating in reflections from behind the detectors are very little and, therefore, not significant. Thus, the temporal expenditure for realizing inconsiderable details clearly outweighs the small benefit. The implemented set-up is shown in figure 3.5. The colours are chosen randomly and do neither correspond to any colour of the actual detectors and components of the cell nor their materials.

The next paragraph explains and motivates the surface properties of the copper wall and the aluminum holder chosen for the simulation as well as the xenon material.

Liquid and Gaseous Xenon

The most essential ingredient in the simulation is xenon – whether liquid or gaseous – that produces the necessary scintillation light for the experiment. The mean atomic mass of xenon is 131.3 u [Dat] where ^{136}Xe has a natural abundance of 8.87 % [AD10]. The measurements with gaseous xenon were performed with cooled gas at about -100°C and a pressure of 1.1 bar where the density lies at about $6.488 \cdot 10^{-3}\,\mathrm{g/cm^3}$ (density at 1 atm: $5.898 \cdot 10^{-3}$ [Dat]). That is two magnitudes less than the density of liquid xenon of about $3\,\mathrm{g/cm^3}$ at 1 bar and -108.1°C [AD10]. All important physical properties as well as the values used in the simulation are listed in table 4.1. Details on all optical xenon properties and the implementation in the code are given in chapter 4.

Copper and Aluminum

The two most important and also the largest surfaces of the inner chamber are the copper wall and the aluminum component containing the source. Although, no propagation of optical photons is possible through any of them, they are expected to contribute to the light signals via reflections. The difficulty of dealing with surfaces is summarized in section 3.3.2 and the implementation is carried out in 4.3.4.

A copper vessel was chosen because of its high thermal conductivity of $398\,\mathrm{W/(m\,K)}$ [Chu01] providing a low temperature gradient throughout the chamber. This property enables a temperature stabilization within the desired interval. Especially for liquid xenon it is crucial to control the temperature, since the interval between boiling point and solid state is only about 4 °C [AD10] at 1 bar pressure.

3.3. Determination of the Photon Detection Efficiency

Several different techniques for determining the photon detection efficiency of SiPMs and other single photon detection devices have already been used and tested by other groups yielding different results with varying reliability. One could name the photocurrent method by Yamamoto et al. (2006) which according to their own scientific report happens to overestimate the PDE of the multi-pixel photon counter they were developing [Yam+06]. A photon counting method by Eraerd et al. (2007) used several lenses to focus light of 532 nm wavelength onto the SiPM and onto an avalanche photodiode (APD) as reference respectively. They report uncertainties due to unmeasured fluctuations in the irradiance on the sensitive areas of their detectors [Era+07].

The following paragraphs explain the general approach for the determination of the PDE of a silicon photomultiplier using the Erlangen test stand for SiPM characterization.

The special nature of this set-up is outlined as well as its imposed requirements on the measurement method. A formula for the PDE determination is derived and motivated.

3.3.1. Basic Principle

Equation (3.2) defines the PDE of a photo detection device as the fraction of detected to incident photons. The number of detected photons N_{Detected} on the SiPM can be expressed in terms of the measured photon flux M and the size of the sensitive area A:

$$M = \frac{N_{\text{Detected}}}{A} \quad \Leftrightarrow \quad N_{\text{Detected}} = M \cdot A \tag{3.4}$$

The area A includes the whole front face of the SiPM without considering the geometry factor. A similar relation like (3.4) applies to the *total* number of photons N_{Incident} impinging on the detection layer of the SiPM:

$$\Phi = \frac{N_{\text{Incident}}}{A} \quad \Leftrightarrow \quad N_{\text{Incident}} = \Phi \cdot A \tag{3.5}$$

here, the photon flux Φ includes all photons on the detector area, no matter if they were detected or not. Therefore, equation 3.2 can be written as

$$PDE = \frac{M \cdot A}{\Phi \cdot A} = \frac{M}{\Phi} \tag{3.6}$$

The numerator is gained from the measurement. In order to determine the denominator one must extract the total number of photons impinging on the SiPM from the one on the reference PMT. Since the latter has a well-known detection efficiency the total flux Φ_{PMT} can be calculated from the measured photon flux M_{PMT}. Afterwards, the expected total photon flux Φ_{SiPM} can be estimated via the photon flux ratio R defined as:

$$R := \frac{\Phi_{\text{SiPM}}}{\Phi_{\text{PMT}}} \quad \Leftrightarrow \quad \Phi_{\text{SiPM}} = \Phi_{\text{PMT}} \cdot R \tag{3.7}$$

Finally, using the above definitions the formula for the PDE calculation of the SiPM can be rewritten as follows:

$$PDE_{\text{SiPM}} = \frac{M_{\text{SiPM}}}{M_{\text{PMT}}} \cdot PDE_{\text{PMT}} \cdot \frac{1}{R} \tag{3.8}$$

Conceived in general terms that means that a PDE is determined via a comparison of the measured photon fluxes. One must also be acquainted with the detection efficiency of the reference PMT. The only unknown factor to be established is R describing the ratio of the total photon fluxes.

Normalizing the number of detected photons to the sensitive area of the detector – i.e. determining the photon flux – and calculating the flux ratio R is a common practice and

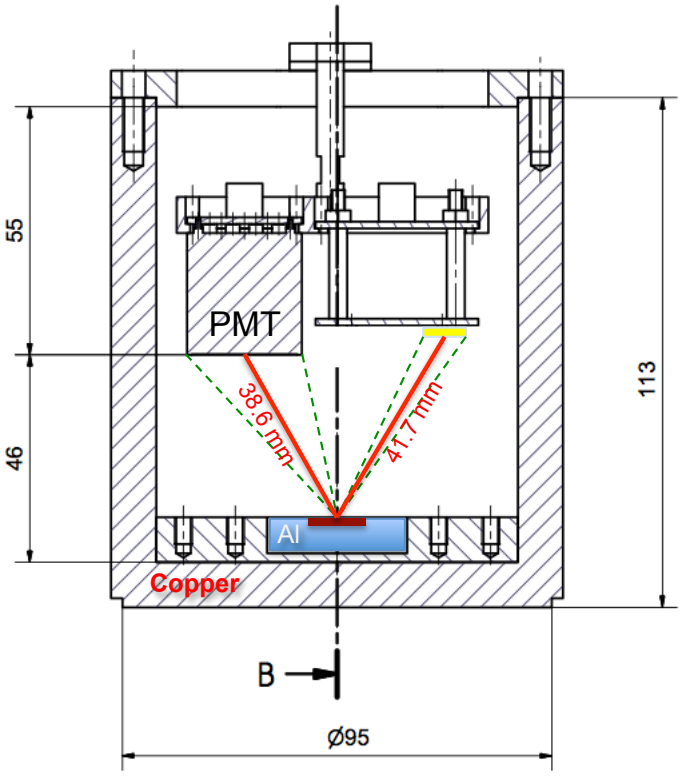

Figure 3.6.: Profile of the inward of the xenon cell with the asymmetric detector set-up and the extended alpha source. The green dashed lines indicate the solid angle between the detectors and the alpha source (if assumed point-like).

has already been utilized for PDE measurements in other set-ups. Yang et al. (2014) have used a reciprocal definition of the photon flux ratio for a PDE determination using two integrating spheres [Yan+14]. That measurement principle is as well based on the comparison of photon fluxes between the examined SiPM and a reference PMT. In their work they claim that "a fair amount of systematics, particularly from R," is needed for the determination of N_{Incident} and, therefore, also Φ_{SiPM}. As will be shown in the next section, the Erlangen set-up which is pretty different compared to the one used by Yang et al., also requires a well understood measurement procedure and special focus on the determination of the photon flux ratio R.

3.3.2. Influences of Specific Properties

One of the main problems of the PDE measurement is the correct determination of the photon flux ratio R which of course differs for every set-up and depends on various factors. Many influences and the special properties of the set-up that are summarized below make an analytical calculation impossible.

Asymmetric Design: In the Erlangen set-up the PMT has a different lateral position and also a slightly different height above the source than the SiPM as seen in figure 3.6. That means that the distance r of the sensitive areas from the source differs as well. If the length of the alpha particles is neglected for now and, so, all photons originate roughly from one single spot, one can roughly estimate the flux on the detectors using the following approximation: Defining the distance as the length between the centre of the detector to the centre of the source and bearing in mind that the flux on an area scales with $1/r^2$ the flux ratio reads:

$$R_{\text{approx}} = \frac{r_{\text{PMT}}^2}{r_{\text{SiPM}}^2} = \frac{(38.6\,\text{mm})^2}{(41.7\,\text{mm})^2} \approx 0.86 \tag{3.9}$$

For equal height and symmetric lateral position of both detectors the above approximation would give 1 as a result. However, as seen in figure 3.7 the mean value of the flux ratio distribution is unequal to 1 even for the symmetric case. The graph shows histograms of simulated flux ratios of the actual set-up using 25000 alpha events, each of which is creating a certain photon flux on the detectors. This was then compared to the simulated flux ratios of a fictitious symmetric construction. Liquid xenon was used, because the alpha has a negligible track length and the photons of an event originate from one point only so that the above approximation can be examined. The problem of extended trajectories will be discussed towards the end of this section in more detail.

The deviation of the mean flux ratio value from 1 has two main reasons: Firstly, the flux ratio is not exactly equal to the square of the inverse ratio of distances between source and centre of the sensitive detectors. The above equation is therefore an approximation, only. To estimate the flux ratio one has to consider the amount of photons emitted into the solid angle Ω between source position and the detector front-face. This angle can be found indicated in the figure as green dashed lines. The solid angle is defined as the partial surface S on a sphere with radius r divided by the radius squared:

$$\Omega = \frac{S}{r^2} \tag{3.10}$$

In case of the detectors S can be pictured as the shadow of a square on the surface of a sphere which the light source in its center. Assuming a point-like source emitting photons isotropically in all directions (at least for high statistics) only those photons can contribute that get emitted in the solid angle of the detector. Here, the solid angle is the one of an oblique pyramid. The number of these photons normalized to the size of the detector surface give the photon flux on one detector. Thus, the flux ratio estimation using solid angle consideration reads as follows:

$$R_{\text{solid angle}} = \frac{\Omega_{\text{SiPM}} \cdot A_{\text{PMT}}}{\Omega_{\text{PMT}} \cdot A_{\text{SiPM}}} \approx R \tag{3.11}$$

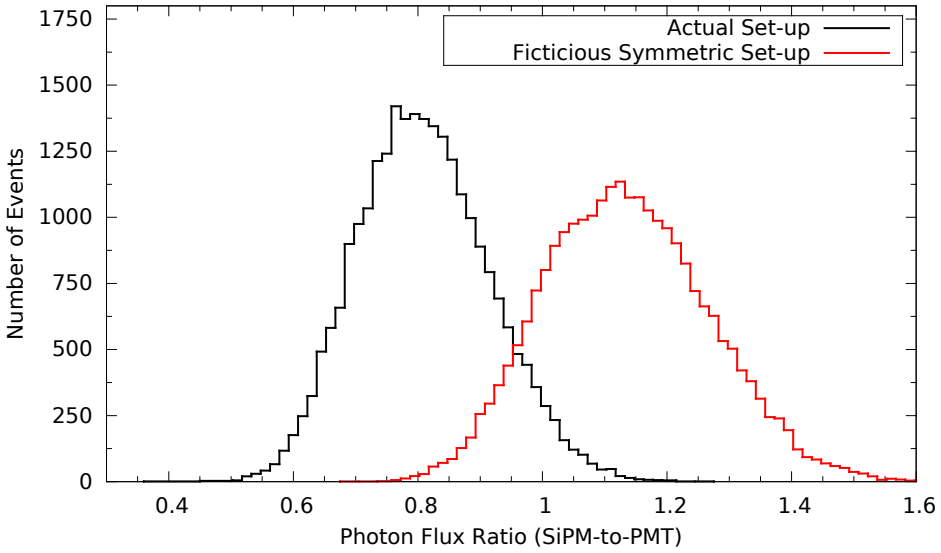

Figure 3.7.: Asymmetric and fictitious symmetric set-up. Even for a symmetric set-up the flux ratio is not equal to 1 due to the different solid angles of the detector surfaces.

This angle can be computed using the expression by Oosterom and Strackee from 1983 for the calculation of a plane triangle [VOS83]:

$$\tan\left(\frac{\Omega}{2}\right) = \frac{\det[\mathbf{r_1}\,\mathbf{r_2}\,\mathbf{r_3}]}{r_1\,r_2\,r_3 + (\mathbf{r_1}\cdot\mathbf{r_2})\,r_3 + (\mathbf{r_1}\cdot\mathbf{r_3})\,r_2 + (\mathbf{r_2}\cdot\mathbf{r_3})\,r_1} \tag{3.12}$$

where the vectors $\mathbf{r_1}$, $\mathbf{r_2}$ and $\mathbf{r_3}$ specify the triangle's corner points. One divides the square surface of each detector into two triangles and calculates the solid angle of each. The sum of both results gives the solid angle of the square. For the PMT a solid angle of 0.23864 sr was calculated and a value of 0.00798 sr for the SiPM. For comparison, a sphere has a solid angle of $4\,\pi \approx 12.57$ sr. Thus, equation 3.11 can be evaluated and the estimated photon flux ratio reads:

$$R_{\text{solid angle}} = 1.08$$

This calculation corresponds to the simulation seen in figure 3.7 which shows a mean flux ratio of about 1.12. The different peak heights are a result of the bin width of the histogram: The relative width of each distribution (i.e. the ratio of the width to the peak position) is pretty much the same, but this causes the left peak to have an absolute width smaller than the one on the right. Since the bin width is constant its values are distributed into a smaller amount of bins and the peak is slightly higher, although 25000 events vere simulated for each configuration.

To sum it up, even if the ratio of squared distances were 1 the solid angle would differ. Therefore, the different sizes of the detectors cause the deviation of the flux ratio from 1 even for a symmetric case.

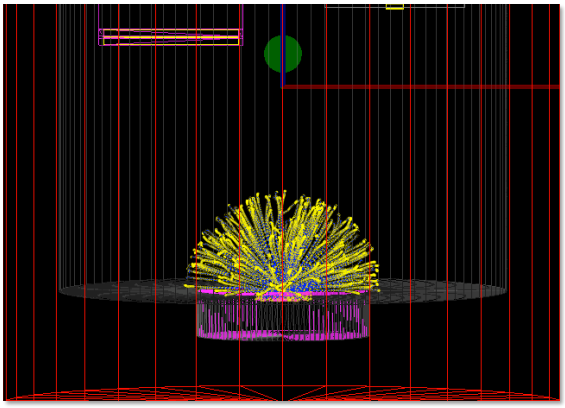

Figure 3.8.: Simulation of 500 alpha tracks in gaseous xenon. Light production was switched off in this case.

Extended Source: The second reason that the flux ratio is not 1 even for a symmetric design is in fact anything else than point-like. That means the alpha particles are emitted randomly from a surface with about 5 mm diameter (see dark red line on the bottom of the cell in figure 3.6). This causes the distances between detector and location of photon production to change as well as the solid angle. This furthermore explains the relatively broad distribution.

Non-negligible Alpha-Trajectory: In xenon gas alpha particles in the energy range of several MeV have track lengths up to several centimetres depending on the density. In the simulation this property could be reproduced as shown in figure 3.8. Scintillation takes places along the whole track of the alpha particle until it is stopped. Since photons are produced all along the trajectory that also means that the momentum direction of the alpha particle has a huge impact on the photon count of each detector. When the alpha is emitted rather towards the SiPM the PMT receives less photons and vice versa. This is the main reason for fluctuations of the photon flux ratio R in this set-up.

Reflections: In all foregoing paragraphs no reflections were considered. But not only light coming directly from the interaction sites of the alpha with the medium can contribute to the signal but also reflected photons from the copper wall of the inner vessel and from the source holder made of aluminum. These are the two surfaces that have the potentially largest influence on the photon counts, since all other components are behind the sensitive areas of the detectors.

Unfortunately, none of the reflectivities is well known for this set-up and the structure of the surfaces was not investigated. A precise measurement of the reflectivities of the copper wall for example would require that a test sample is examined under the same conditions as inside the actual chamber. i.e. using the same wavelength, temperature, density, medium etc. Furthermore, that test sample would be required to have the same

surface structure as the inner wall of the xenon cell. Since that might change already by just using different polishing methods, a reliable surface investigation is hardly possible. Moreover, during the performance of the measurement it was seen that the surface appearance had slightly changed due to deposits of dust. That could have had a huge impact on the reflection properties of the material (and also on the purity of the xenon).

Especially the last one of these four main influences on the flux ratio R can not be calculated or approximated. Only a simulation of the physical processes can give reliable predictions. This includes the alpha trajectory, the scintillation process and the tracking of the photons, similar to S. Yang et al. using a ray tracing Monte Carlo simulation and taking the exact geometry of the instrument into account [Yan+14].

The main task of this work is therefore, to determine the ratio of photon fluxes and examine its behaviour under variable surface properties using simulations. R shall in the following be refered to as the *correction factor* since it corrects the deviation from an ideal case where the photon flux is equal on both detectors or can at least be calculated using geometric arguments (see equation (3.7)). This is surely not the case in this set-up. R therefore enables a sensible comparison of the photon fluxes of SiPM and reference detector.

The next chapter describes the necessary simulation tools, summarizes the basic structure of the programme and how it implements the required physical processes. The physical validity is tested until finally in chapter 5 the correction factor R is determined.

4. Simulation of the Erlangen Set-Up

4.1. Setting up a Monte-Carlo-Simulation Using Geant4

4.1.1. Introduction to the Simulation Toolkit Geant4

GEANT stands for *Ge*ometry *an*d *T*racking and is a toolkit based on Monte Carlo simulations of physics detectors and physical processes. Its basic application is the simulation of the passage of particles through matter and their interactions. The software framework provides a vast set of long-lived particles and physical processes, like electromagnetic, hadronic and optical processes. It covers a wide range of energy up to TeV and is designed to deal with complex geometries and physics models. Therefore, GEANT4 is used for many different applications ranging from particle and nuclear physics to medical sciences and also space engineering.

The increasing size and complexity of experiments especially in modern particle and nuclear physics demand solid software frameworks for accurate simulations of particle detectors. Based on the predecessor and benchmark GEANT3, modern computing techniques have been investigated with regard to their applicability for particle simulation starting in 1993. The resulting world wide project RD44 – run by about 100 scientists and engineers – adapted object-oriented programming in the practical C ++ language and finished its R&D phase in 1998. Since January 1999 the GEANT4 Collaboration develops and improves the toolkit and provides servicing and user support. The massive scope of the code and the amount of contributors make this tool "one of the largest and most ambitious projects of its kind" [Ago+03].

As the word "toolkit" suggests researchers can set up their own programs using a vast set of various cohesive components. The size of these applications can range from small laboratory studies to detector simulations for experiments like the Large Hadron Collider. All important aspects can be included in the simulation like geometry, material and the particles of interest as well as particle tracking, detector response, generation and storage of event data and visualization of trajectories. [Ago+03]

In the following the working principle of this software framework, the functionality of the tracking process of particles as well as the code structure of the application to the Erlangen set-up will be outlined.

4.1.2. Structural Aspects of the Simulation

The modular and flexible architecture of GEANT4 enables the users to only pick components that are needed for their specific application. The framework can therefore be customized and extended in all domains. All key domains are linked by a unidirectional flow of dependencies and build a hierarchical structure for the toolkit. The most important aspects of the design are listed below:

Events: Represent the main unit of the simulation. An event contains primary vertex and particle and, after processing, provides hits, digitizations and trajectories. For performance reasons the content is not permanently stored and the user must implement a user action class to access it.

Geometry and detector representation: For describing the geometrical structure and the particle propagation through it, the concept of *logical* and *physical* volumes is used. While the logical volume contains size, shape and material of an object, the physical volume is responsible for its spatial position inside a so called *mother volume*. A hierarchical tree structure of volumes is formed.

Tracking: The performance of a simulation depends on the time spent per step. Thus, particles in GEANT4 are transported rather than considered self-moving and the tracking domain steers the invocation of transportation processes from step to step. The step length is chosen by the `SteppingManager` according to the materials and the physics processes that were implemented by the user. Ideally it is as large as possible to limit the number of steps for each particle but should still be small enough to keep the accuracy of the simulation. Step lengths are proposed by processes in form of a mean distance to an interaction in the current material or to the closest geometric boundary.

Physics processes: Conform to a basic interface `G4VProcess`. Users can apply one of the 7 major process categories `Geant4` provides or construct own processes. In this work `G4EmStandardPhysics` is used handling basic processes for electrons, positrons, photon and hadron interactions together with a self-made `PhysicsConstructor` especially for optical processes like scintillation and Rayleigh scattering.

Particles and Materials: Are a facility to describe physical properties of particles and materials to simulate their interaction. In the `G4ParticleDefinition` class basic particle properties like mass or charge are stored as well as a list of processes that apply to it. Particles are always defined as a *singleton* to make all processes refer to the same particle properties. Materials carry a so called `MaterialPropertiesTable` managing its composition and surface properties for optical photons and are passed to the detector construction together with the logical volume. [Ago+03]

The interplay of the above mentioned domains is summarized in the following paragraph with a main focus on the tracking procedure of particles based on the corresponding physics processes.

4.1.3. Functionality of Tracking and Stepping

All information on this chapter is taken from [Ago+03], [Col14a] and [Col] if not indicated differently.

Tracking Hierarchy As already mentioned the *Event* is the most important unit of the simulation and contains all tracks of all particles and secondaries that are to be simulated starting form the first vertex until the moment a particle is absorbed or interacts. The tracking process has a hierarchical structure. When an event is started the `G4EventManager` passes a track to the `G4TrackingManager` which contains information like current position or time since start. Since any particle is simulated step by step providing an efficient and unbiased way of simulation a track is basically the sum of all steps. The `G4SteppingManager` controls the step-wise simulation and selects the process that proposes the shortest step length to preserve maximum precision. The shortest unit in any simulation is represented by `G4Step`, a class containing all transient information between two steps. These are amongst others the coordinates of the particle, the current volume, total and deposited energy as well as the momentum and its direction. All information can be accessed by so called UserAction classes described in 4.1.4.

Interactions and Step Length Any interaction of the particle with the medium is based on a *physics process* and a certain physics model. The latter one implements the production of secondaries. The physics process, however, is defined by a particular initial and final state of the particle undergoing that process and therefore has a well-defined cross-section and mean lifetime. Processes determine the interaction and influence `G4SteppingManager`'s choice of the step length:

Considering a particle in flight one can calculate the distance to the interaction or the decay, which is characterized by the mean free path λ. The probability that the particle has not undergone an interaction within a distance s can be expressed as follows:

$$P(s) = e^{-n_\lambda} \tag{4.1}$$

$$\text{where} \qquad n_\lambda = \int_0^s \frac{\mathrm{d}s'}{\lambda(s')} \tag{4.2}$$

n_λ denotes a multiple of the mean free path λ, the latter of which varies with the energy of the particle and is not continuous at boundaries of volumes. Furthermore, the mean free path depends on the cross-section and the density of the medium. All

that is provided by the physics processes used. The probability distribution of n_λ is exponential according to 4.1. Therefore:

$$n_\lambda = -\ln(\eta) \tag{4.3}$$

$$\eta \in (0;1) \tag{4.4}$$

where η is a random number uniformly distributed using Monte-Carlo methods. This way, the distance to the point of interaction is simulated for all processes associated with the particle (each one with a different random number). Other processes like *continuous energy loss* contribute as well to limit the step length and to preserve precision. The process with the smallest distance is invoked by `G4SteppingManager`. Then, the particle either interacts, produces secondaries or is absorbed or – if none of these applies – its energy and momentum information is updated and the particle gets another change to interact in the next step. In the latter case the above algorithm starts again. [Ago+03; Col]

A particle is tracked to the end of its range (i.e. until the end point of their trajectory), but for performance reasons a range cut can be applied: When interactions occur and secondary particles are created, all particles with a range below a user-defined value are suppressed. A cut value can be applied to individual particles or physics processes. In this simulation the range cut value was set to $1\,\mu$m.

The Standard Electromagnetic Process implements a variety of interactions between electrons, positrons, photons, and charged hadrons and can be registered in GEANT4 via the `G4EmStandardPhysics` in the Physics List. A photon for instance can undergo Compton Scattering or photo-electric effect, for an electron processes like bremsstrahlung, ionization or synchrotron radiation are provided. Effects of shell structures of atoms are averaged in this physics package.

At the beginning of a simulation run the electromagnetic process sets up tables of particle ranges and photon absorption lengths for each material. The particle range – for example for an alpha particle in xenon – is computed by numerical integration of the energy loss per travelled distance. During the simulation the process of energy loss imposes a limit on the step size, while the energy loss ΔT per step is calculated using an approximation for sufficiently small step sizes s called *linear loss limit*:

$$\Delta T \approx s \left| \frac{\mathrm{d}E}{\mathrm{d}x} \right| \tag{4.5}$$

In general the energy loss per covered distance is described via a retarding force on the particle called *stopping power*:

$$\mathrm{S}(E) = -\frac{\mathrm{d}E}{\mathrm{d}x} = -\left[\left(\frac{\mathrm{d}E}{\mathrm{d}x} \right)_{\mathrm{NR}} + \left(\frac{\mathrm{d}E}{\mathrm{d}x} \right)_{\mathrm{ER}} \right] \tag{4.6}$$

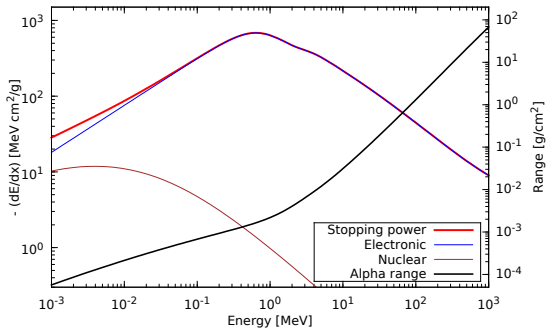

Figure 4.1.: Stopping power together with its two components (electronic and nuclear recoils) and particle range (normalized to the density) for alphas in xenon depending on their energy. From [Ber+05a]

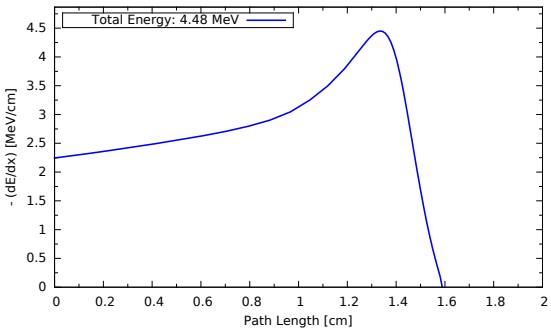

Figure 4.2.: Stopping Power versus path length for an alpha particle at 4.48 MeV in GXe with a density of 6.48 g/cm^3; Total range: 1.59 cm. From [Ber+05a]

It contains energy losses due to nuclear recoils (NR) in which the target atom collides as a whole and the corresponding electronic component (electron recoil ER) [Szy+11]. The latter describes the energy transfer to electrons via ionization or excitation which is explained in connection with the scintillation mechanism in section 4.3. For alpha particles NR only contributes to about 30 % [Ber+05a] of the total energy loss per unit path length for low energies in the keV range and is even more rapidly decreasing for higher energies. This means the fraction of NR of the total energy deposit is negligible [Apr+07; CA13].

The total energy of a particle is either user-defined (for the primary particle) or calculated (for secondaries). Either way, with given energy GEANT4 computes the total range of the particle by integrating the inverse stopping power over the energy of the particle:

$$\Delta x = \int_0^{E_{tot}} \frac{\mathrm{d}E}{\mathrm{S}(E)} \tag{4.7}$$

The range of an alpha particle in xenon gas depending on its energy can be seen in figure 4.1. The stopping power (red) is normalized to the density of the material and given in MeV cm^2 / g. The range is usually obtained by assuming that the energy loss is continuous along the track and that fluctuations can be neglected. It is also called *Continuous slowing down approximation* range and is measured in g / cm^2 [Icr]. For this work alpha particles with energies between 4.15 and 4.80 MeV were used (compare section 3.2.2) resulting in ranges from 1.44 cm and 1.73 cm respectively. These values are valid for GXe with a density of 6.48 g/cm^3. In LXe the range is only between 31 μm and 38 μm. In graph 4.2 the stopping power is plotted against the path length for gaseous xenon. The stopping power of an alpha track in LXe has basically the same shape but the absolute values of S(E) are much higher and the range correspondingly

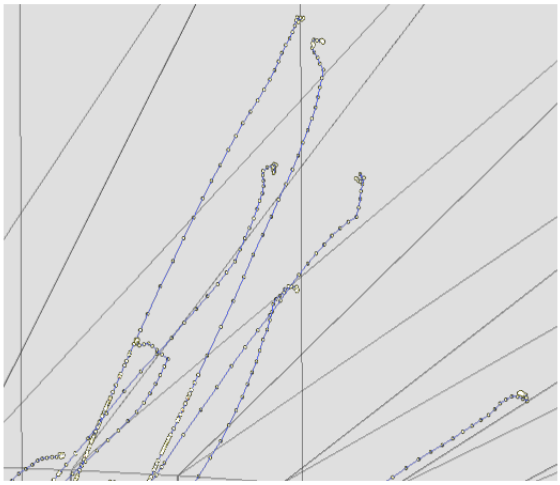

Figure 4.3.: Simulated alpha particles in gaseous xenon. The step length between interactions decreases with decreasing particle energy towards the end of the range.

shorter. The energy deposit is continuous but not constant along the trajectory and increases towards the end of the range. The maximum is usually called the *Bragg peak*. The larger derivative around the Bragg peak explains why equation (4.5) can only be an approximation. However, GEANT4 preserves the precision of the simulation by lowering the step size in that region leading to more interactions on shorter distance and, thus, reproducing the Bragg peak. The integral over the path length – i.e. the area under the curve – gives the total energy of the alpha particle. [Icr]

Figure 4.3 shows tracks of simulated alpha particles in GXe to demonstrate the behaviour of a particle at the end of its range. The yellow spots are the interaction sites of the alpha particle with the medium. The step size gets smaller towards the end of the range to preserve the validity of the approximation in (4.5). The almost linear trajectory gets more and more curvy towards the end where the particle has only a small part of its energy left. Still, the largest fraction of the energy is deposited at the end of the track. One can also see that there are more interaction sites at the lower left of the picture. This is the part of the track where the alpha particle produced electrons via scintillation that are able to exceed the cut value and therefore are not suppressed. Towards the end no electron production takes places any more and the energy just gets deposited in the material. It is worth noting that the total range of the particle is not the distance between start point and endpoint of the trajectory but the total path length covered by the particle, i.e. the sum of all step lengths.

The range of a particle depends, besides its energy, also on charge and mass. For low mass particles like electrons the trajectory is curved and contains multiple scattering. Also, the density of the medium has an impact on the track length which is why alpha

particles in LXe only cover a total path length in the range of μm [Apr+07]. The next part explains how a simulation is built in GEANT4 and which parts of the toolkit were applied to the simulation of the Erlangen set-up.

4.1.4. Application Development for the Erlangen Set-Up

This section explains the construction of the code for the simulation of scintillation light in the Erlangen set-up based on the existing framework, interface and the design structure given by GEANT4. It outlines how the framework is customized and extended for this purpose.

To set up an own application, GEANT4 provides an abstract interface for eight user classes, three of which are mandatory for the program to work. They are initialized at the very beginning of each simulation. The other five so called UserAction classes allow the user to modify the default behaviour of the simulation and gather data. The three necessary classes are:

`G4VUserDetectorConstruction:` This class constructs all geometrical shapes together with their materials and allocates a specific position to them. A `G4Material` can either be established by the user via constructing molecules and defining a density or chosen from the a data base via `G4NistManager`. Surfaces and their behaviour are set in the detector construction as well and defined as the geometrical border between two volumes. Also the colour and other visualization attributes can be assigned here.

`G4VUserPhysicsList:` All particles, physics processes and models are loaded within this class. The user can again choose a predefined physics list, but usually applications demand special requirements and processes leaving the user with no other option but to set up an own physics list. As a physics process, `G4EmStandardPhysics` was registered (for details see section 4.1.3) together with a self-made collection of optical processes called `PhysicsConstructor`. Here, all particles necessary for the simulation of scintillation are registered: Electrons, alpha particles and optical photons, whereby a photon is considered optical if its wavelength is larger than the typical atomic spacing, otherwise called *gamma* and described by a separate class [Col]. This constructor for optical processes contains absorption and Rayleigh scattering as well as boundary interactions with surfaces implemented in the detector construction. Scintillation is generated by use of the NEST-Add-On, where NEST stands for *Noble Element Simulation Technique*. Its contents and working principles are described in 4.3.3.

The Physics list also sets the range cut explained in 4.1.3 to suppress particles whose range is lower than the user-defined value. For the purpose of energy conservation the energy is then added to the amount of energy deposited in the medium by the primary particle.

`G4VPrimaryGeneratorAction:` This class creates the first vertex of the simulation. This includes the primary particle, its energy and momentum direction starting at a certain position. For the Erlangen set-up alpha particles with three different alpha energies were used according to the composition of the source. For each event the energy and the starting position is chosen randomly with respect to the expansion of the source located on the aluminum holder. Also, the particle momentum direction gets randomly selected each time, whereby only emissions into the upper half space are possible, because otherwise the particles would be stopped and absorbed by the aluminum immediately and no light production could take place.

All the above mentioned mandatory user classes have to be passed to `G4RunManager` in the main function so that they get initialized with the run kernel at the beginning of the run. A *Run* is the largest unit containing as many events (i.e. several single simulations of alpha particles in xenon) as the user wants to process and is started by the `G4RunManager` using the method `beamOn()`. Also initialized at the beginning are *UserAction Classes* which are virtual classes the user may override to control different parts in different stages of the simulation. These are:

- `RunAction`
- `EventAction`
- `TrackingAction`
- `SteppingAction`
- `StackingAction`

The last one customizes the access to the track stacks but was not used in this simulation and will not be further discussed. The empty default implementation of these classes enables the user to only inherit from classes that are needed. In this work the required UserAction classes are implemented all within one singleton class which was part of a larger comprehensive programming unit called *Measurement Analysis and Run Control Interface*. This self-made class composition is explained in 4.1.5 in more detail.

4.1.5. Measurement, Analysis and Run Control Interface (MARCI)

The reason this interface was implemented is to build a connection between the rudimentary particle simulation on the one side and the data analysis procedure on the other side. It is an interconnection point of program parts provided by GEANT4 and the user-defined code that is customizing the simulation for the own application. It consists of four classes depending on each other and which are connected to the rest of the code: `Analysis, RunControl, Messenger` and `ScriptWriter`. In order

to give an overview of the functionality, the name of the interface is motivated as follows:

The *Measurement* part of this interface is responsible for the data taking process. It implements the user action classes providing data in orderly manner and handing them to the analysis. The *Analysis* contains a set of methods writing scripts individually for each run in order to prepare the data analysis with C++ programs after the simulation has finished. These programs which are no integral component of the GEANT4-application are invoked afterwards and analyse the pre-processed data, thus, producing the final results. *RunControl* manages all parameters for the simulation which can either be set via arguments in the `main()` function or the stored default values are used. Program parts like the detector construction of the primary generator collect the parameters from there at the beginning of a run and set up the simulation with these values. By doing so, a large amount of parameters can be changed without the need for re-compiling of the whole code.

`RunControl` is implemented as a singleton which means only one object can be instantiated once the program is started. This is necessary since this `RunControl` functions as an administrator of all parameters which are then distributed to the individual parts of the simulation. 25 different parameters can be changed using arguments for the `main()` function when starting the program. If no value is passed or the entered value is not valid the default setting is used. Variable parameters reach from organizational adjustments like output path and file name to properties that can modify an entire run: The user can now decide if GXe or LXe is to be used and can set its density. Particle energy and type, cut value and scintillation yield can be changed as well as optical and surface properties. Settings for the tracking and the amount of command line outputs can be altered and also crucial properties of the detector construction like the position of the SiPM and the efficiency of the detectors. `RunControl` also implements a method creating a seed for the random engine using current date and time. Also, to prevent data from getting overwritten, `RunControl` creates a default output file for each run, by using time and date as file name.

`Analysis` implements the UserAction classes. It is constructed as a singleton to make sure only one instance gathers data and writes them to file. Treating all UserAction classes in one single class makes the access to the different stages of the simulation much more comfortable and easier to handle. This class is the essential part of the interface since it collects all important values from the steps and the tracks of each event that are relevant for the analysis.
Therefore, at the beginning of the simulation a new run is prepared setting file path and output name in the `PrepareNewRun()`-method. When a run is finished `EndOfRunAction()` invokes methods from the `ScriptWriter` to build `C++` and `GnuPlot` scripts for the pre-analysis of the data and also prints conclusive command line outputs. During an event – which consists of one alpha particle getting emitted into the xenon by the source – the `PreUserTrackingAction()` counts the number of photons, electrons,

gammas or other particles that are emitted and that the user is interested in.
Finally the `SteppingAction()` counts the photons that hit the detectors. For the calculation of the photon flux ratio R *all* photons are counted, but each of the detectors can also be equipped with a specific efficiency. GEANT4 actually provides interfaces for sensitive areas and detector hits but the implementation in MARCI is faster and easier to handle, since from the preparation of a run till the scanning of each step all data gathering happens in one class.
It is also possible to connect further analysis and read-out classes to this one and centrally handle all within one class. For instance this was done to set up a method calculating the particle ranges of all particles the user is interested in.

`Messenger` creates header and footer for data files containing all parameters that were used and also prints out error messages. For example if the entered parameters were wrong or out or range the method `PrintMainArgError()` explains the mistake and gives a list of all variable settings and the required commands to change them.

`ScriptWriter` is a class that automatically creates scripts that can be loaded after the run to create histograms of the different detector signals or scatter plots where the detector signals are plotted against each other etc. This enables a quicker analysis and an easier access to a first visualization of the data produced. This is a useful tool, since for the determination of R 121 runs are necessary (compare chapter 5) each of which is producing a vast amount of data. The `Scriptwriter`, therefore, speeds up the analysis process and simplifies error-treatment and debugging.

4.2. Materials and Detector Construction

4.2.1. Liquid and Gaseous Xenon

Liquid xenon is chosen as detector medium for the nEXO experiment and is used in Erlangen as well, therefore, also implemented in this simulation. Its most important property, which it has in common only with argon, is that it produces scintillation light as well as free charges in response to radiation. Simultaneous measurement of both signals with sufficient efficiency gives information on the particle's type, energy and location of interaction. Due to its high density liquid xenon has a high stopping power making it an efficient medium to stop penetrating particles. The downside of xenon is its solubility in water. Trace amounts of water are very difficult to remove. Therefore, limits to the performance are set by water being the main impurity. [Apr+07; AD10].

Of similar importance are the optical properties of xenon, above all, attenuation length λ_{att} for scintillation light and refractive index n. Several different values can be found for n in LXe: Baldini et al. (2005) measured a refractive index of 1.65 ± 0.03 [Bal+05], whereas, Solovov et al. in the year before gave a value of 1.69 ± 0.02 [Sol+04]. In this simulation $n = 1.68$ was used which corresponds to the experimental results from

Hitachi et al. [Hit+05] who also performed measurements for the attenuation length. Furthermore, they determined the refractive index of gaseous xenon to be close to 1.

The attenuation of light with intensity I travelling through a medium can in general be described by

$$I(x) = I_0\, e^{-x/\lambda_{\text{att}}} \tag{4.8}$$

$$\text{where} \qquad \frac{1}{\lambda_{\text{att}}} = \frac{1}{\lambda_{\text{scat}}} + \frac{1}{\lambda_{\text{abs}}} \tag{4.9}$$

[Bal+05]. Here, λ_{abs} denotes real absorption that leads to photon loss, whereas λ_{scat} describes elastic scattering processes without loss of photons. The scattering processes are dominated by Rayleigh scattering. Therefore, in GEANT4 a *Rayleigh Scattering Length* λ_{R} is defined and used for the purpose of representing the scattering length λ_{scat}. Unfortunately, none of the above defined lengths is known exactly from experiments for scintillation light in xenon, especially no value for λ_{abs} was ever determined until 2005 Balbini et al. could set a lower limit for the absorption length of $\lambda_{\text{abs}} > 100\,\text{cm}$ at 90 % confidence level (C.L.). Actually, xenon is transparent for its own scintillation light at 175-178 nm, but impurities like water or oxigen can absorb VUV light, even if their amount is in the range of parts per milion (ppm). This sets a limit to the absorption length, which is strongly dependent on the purity of xenon. Balbini et al. gave the above mentioned value after a lengthy procedure of xenon purification. Before that process an absorption length of only $12.0 \pm 1.8\,\text{cm}$ was determined in a prior measurement. In an individual process they calculated an attenuation length of $54^{+14}_{-9}\,\text{cm}$ using a comparison with measurements in gas, where an infinite absorption length was assumed. However, a Rayleigh scattering length of 45 cm was set for gas [Bal+05]. According to their own report, overestimation of λ_{att} is possible due to inaccurate photon measurements.

The scattering length in LXe could only be narrowed down to an interval of 20-50 cm, although theoretical estimations provide a value of 30 cm [AD10]. In this thesis the value for λ_{scat} in GXe is the same as in LXe and was set to 40 cm.

Unknown impurities in the xenon could explain why Solovov et al (2004) determined a deviating attenuation length of $36.4 \pm 1.8\,\text{cm}$ [Sol+04]. Furthermore, conclusions on the relative contributions of absorption and scattering to λ_{att} were not possible with their experiment. Since the actual impurities in the xenon used for the experiments in Erlangen were unknown and it was also obtained that purity can change with time probably due to out-gassing parts in the chamber, the absorption length was set to a high value of 2000 cm. This represents ideal, ultra pure xenon conditions. Still, the resulting attenuation length according to formula (4.9) is 39.2 cm and lies between the experimental results by Balbini and Solovov. An overview of all optical properties can be found in table 4.1.

Physical Properties	**Symbol**	**GXe**	**LXe**	**Unit**
Mean atomic weight	m_{A}	131.3 [(a)]		u
Atomic number	Z	54 [(b)]		-
Boiling Point	T_{b}	165.05 [(b)]		Kelvin
Pressure	p	1.1	1.0	bar
Temperature	T	173.15	163.2	Kelvin
Density				
normal conditions	ρ	$5.898 \cdot 10^{-3}$ [(a)]	3 [(b)]	g/cm^3
at used p and T		$6.4878 \cdot 10^{-3}$	3	g/cm^3
Optical Properties				
Absorption Length	λ_{abs}	–	> 100 [(d)]	cm
used in this work		2000	2000	cm
Scattering Length	λ_{scat}	–	29-50 [(d)]	cm
used in this work		40	40	cm
Refractive Index	n	≈ 1.0 [(c)]	1.68 [(c)]	-

Table 4.1.: Properties of liquid and gaseous xenon and the values that were used in the simulation. Note that absorption and scattering are negligible in gaseous xenon [Bal+05]. [(a)][Dat], [(b)][AD10], [(c)][Hit+05], [(d)][Bal+05]

4.2.2. Detectors

Additional to the medium in which photons are produced and propagate the detectors are implemented in the simulation for the detection of the scintillation light. For the SiPM a lumogen coated model by KETEK was used while the PMT is the HAMAMATSU device R8520-406. The SiPM and the PMT are implemented with the exact size and proportion as the detectors in the actual set-up. The total sensitive area of the SiPM was measured to be $3.6\,\mathrm{cm} \times 3.6\,\mathrm{cm} = 12.96\,\mathrm{cm}^2$. The photo cathode area of the PMT is $20.5\,\mathrm{cm} \times 20.5\,\mathrm{cm} = 420.25\,\mathrm{cm}^2$ [Ham] which makes its sensitive surface 32.4 times larger than the one of the SiPM.

The detector positions inside the xenon cell were established using CAD drawings together with further measurements. The asymmetric positioning of SiPM and PMT was discussed in section 3.2.2 and 3.3.2. The absolute distances of the center point of the sensitive area of each detector from the alpha source are 38.6 mm for the PMT and 41.7 mm for SiPM (also compare section 3.3.2).

PMT and SiPM have a specific sensitivity spectrum, i.e. the efficiency to detect photons depends on the wavelength of the incoming light. Since scintillation light only has a limited spectral range (see section 4.3) the change in detection efficiency throughout this range is neglected. For the determination of the photon flux ratio the efficiency of photon detection was set to 100 % for both devices to capture all photons impinging

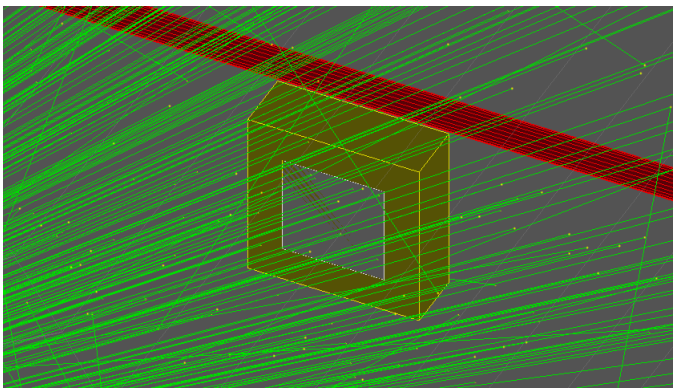

Figure 4.4.: Implementation of the SiPM in the GEANT4 simulation: geometrical shape and measures correspond to the real SiPM. The light collecting part is defined as a sensitive volume (grey square) that is able to count entering photons (green lines).

on the sensitive area. However, the simulation provides the option to set a user defined efficiency if needed. The detection of photons in the simulation is performed by defining sensitive volumes that are able to increment a counter when a photon has entered the volume. The front face of the volume matches the actual size of the sensitive area of each detector. When a photon is counted its track-ID is saved by the analysis class of the interface MARCI so that no photon can accidentally be counted twice during the tracking process. Exemplary the SiPM is depicted in figure 4.4: The SiPM frame (yellow) denotes the border of the sensitive volume (grey square). Photons that are shown in green colour impinge on the surface. The implementation of the PMT is analogous.

4.3. Scintillation and Light Propagation

This chapter contains explanations on the production of scintillation light in liquid and gaseous xenon. Details on the implementation on GEANT4 are given as well as a discussion of optical processes at surfaces and boundaries of media.

4.3.1. Energy Dissipation in Xenon

An energetic particle like an alpha transfers energy to the atoms of the medium in two ways: *ionization* and *excitation*. While ionization removes an electron from an atom leaving a positively charged ion and a free electron, excitation raises an electron to a higher energy state without removing it from the atom. Both electron-ion recombination and deexcitation happen through a cascade process under emission of a photon. Light coming from this process has a wavelength characteristic for the medium and also its physical state (liquid or gaseous). Free electrons may as well have enough energy to generate electron-ion pairs themselves or perform excitation [Apr+07].

Property	**Symbol**	**GXe**	**LXe**	**Unit**
Atomic ionization potential	E_i	$12.13^{(a)}$	$11.67^{(a)}$	eV
Excitation potential	E_{ex}	$8.32^{(a)}$	$8.32^{(a)}$	eV
Ionization efficiency	W_i	-$^{(*)}$	$15.6 \pm 0.3^{(a)(b)}$	eV
Minimum scint. efficiency	W_{ph}	-$^{(*)}$	$13.8 \pm 0.9^{(a)(d)}$	eV
for α (5 MeV)	W_{ph}^{α}	-$^{(*)}$	$17.9 - -39.2^{(d)}$	eV
Excitation-to-ionization ratio	$\alpha = \frac{N_{ex}}{N_i}$	$0.19 - 0.69^{(e)(*)}$	0.06 (calc.)$^{(d)}$	eV
			0.20 (meas.)$^{(d)}$	eV
Scint. light peak wavelength	λ	$175^{(c)}$	$178^{(c)}$	nm

Table 4.2.: Scintillation Properties of Xenon. $^{(a)}$[Apr+07], $^{(b)}$[Dok+02], $^{(c)}$[Jor+65], $^{(d)}$[CA13], $^{(e)}$[Mim+09], $^{(*)}$These quantities have a strong density dependence and can not be further specified in this scope.

The total energy E_0 transferred to the xenon by an impinging alpha particle is split up in three main contributions which are expressed by Platzmann's equation:

$$E_0 = N_i E_i + N_{ex} E_{ex} + N_i \, \varepsilon \ , \tag{4.10}$$

where E_i is the mean expenditure for the ionization process and E_{ex} for excitation respectively. ε denotes the average kinetic energy of a subexcitation electron that has an energy lower than the excitation potential of xenon atoms. Below an energy of ε a free electron can only undergo elastic collisions with atoms and therefore increase the thermal energy of the medium but not ionize or excite atoms. E_i is larger than the ionization potential owing to excited or multiply charged ions. Typical values for E_i and E_{ex} can be found in table 4.2.

The ratio of excited to ionized atoms $N_{ex}/N_i =: \alpha$ for LXe lies between 0.06 and 0.20 [CA13; Szy+11]. For gas α is strongly density dependent and the variety of values available in cited literature is even larger (compare section 4.4). Although the partitioning of the deposited energy into the excitation and ionization channel depends on the particle type, it does not change with different starting energy E_0 [CA13]. The effectiveness of the absorbed energy to be transferred into a certain number of electron-ion pairs is described by the so called *W-value*.

$$W_i = \frac{E_0}{N_i} \tag{4.11}$$

Some readers may notice that in literature this quantity is often designated *without* the index i, though it only refers to the number of electron-*ion* pairs that are created per absorbed energy. Thus, equation 4.10 reads:

$$W_i = E_i + \alpha \, E_{ex} + \varepsilon \tag{4.12}$$

In a TPC like the one used in EXO-200 or the one designed for nEXO, a high electric field is applied to drift free electrons and read out the charge signal. In the Erlangen set-up only light signals are of interest. Without an electric field it can be assumed that all electrons recombine with xenon ions (recombination probability $r \approx 1$). So, the total number of produced scintillation photons coming from $r \cdot N_i$ recombined electron-ion pairs and N_{ex} excited atoms may be described as

$$N_{ph} = rN_i + N_{ex} = N_i(r + \alpha) \overset{r\approx 1}{\approx} N_i(1 + \alpha) \ . \tag{4.13}$$

Using (4.13) one can define a W-value for the average required energy for production of a scintillation photon following the example of equation (4.11):

$$W_{ph}^{min} = \frac{E_0}{N_{ph}} = W_i/(1 + \alpha) \tag{4.14}$$

This is also referred to as *minimum scintillation efficiency* and corresponds to the smallest possible mean energy needed for the production of a scintillation photon, i.e. at zero field and when there is no quenching which depends on the topology of the track and the ionization density along the path of the particle. For lower ionization densities some electrons escape the recombination even at zero field. This is why in general $N_{ph} < N_i + N_{ex}$ and the value for the scintillation efficiency is larger. An electron not recombining with an ion decreases the light signal but on the other hand contributes to the charge signal in a TPC like in nEXO. This is why an anti-correlation between light and charge signal is expected. Recombination is discussed in more detail in section 4.3.3 together with a valid justification why a recombination probability of ≈ 1 can be assumed for alpha particles at the given conditions in the Erlangen set-up.

The ionization efficiency W_i is a pressure dependent quantity as can be seen in figure 4.5. A change of density from $0.12\,\mathrm{g/cm^3}$ to $1.7\,\mathrm{g/cm^3}$ gives a decrease to the energy spent for electron-ion formation by $\approx 15\,\%$. This graph also shows a changing slope at about $0.5\,\mathrm{g/cm^3}$ due to formation of electronic bands for elevated densities which is lowering the ionization energy and the photoconductivity threshold. A linear extrapolation towards higher densities gives a value for LXe of $W_i = 15.3\,\mathrm{eV}$ at a density of $3.06\,\mathrm{g/cm^3}$ which is in good agreement with measurements ($15.6\,\mathrm{eV}$ [Dok+02]).

Furthermore, density influences the light yield as well which is defined as the total energy deposited by the particle divided by W_{ph}: The yield of scintillation photons increases with densities up to $0.1\,\mathrm{g/cm^3}$. Note that in some literature the scintillation yield is also simply defined as $1/W_{ph}$. For alpha particles in xenon gas the yield decreases again above $0.1\,\mathrm{g/cm^3}$. The pressure dependency is tested in the simulation for the lower density range. Details are shown in part 4.4. [CA13; Apr+07]

4.3.2. Scintillation Mechanism

The two processes leading to the emission of scintillation light – ionization and excitation – result in the formation of diatomic excited molecules, so called *excited dimers*

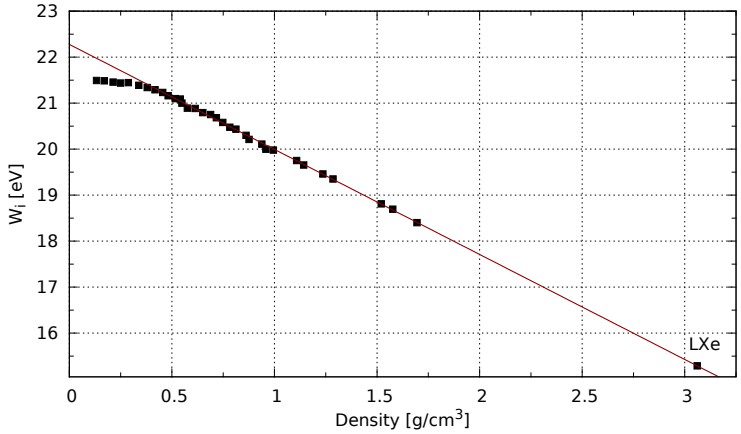

Figure 4.5.: Pressure dependency of the W-value. From [BR97]

or short *excimers*. The cascade process forming such excimers and the deexcitation under the emission of VUV light is explained in the following paragraphs.

Impact excitation leads to the formation of an excited Xenon atom Xe^*, which then undergoes the following cascade:

$$Xe^* + Xe \rightarrow Xe_2^{*,\nu} \qquad \text{excimer formation} \qquad (4.15)$$

$$Xe_2^{*,\nu} + Xe \rightarrow Xe_2^* + Xe \qquad \text{relaxation process} \qquad (4.16)$$

$$Xe_2^* \rightarrow Xe + Xe + h\nu \qquad \text{VUV light emission} \qquad (4.17)$$

Here, ν denotes the vibrational excitation of an excited state. The emission of the photon is part of the transition of one of the electronic excited states ${}^3\Sigma_u^+$ (singlet state) or ${}^1\Sigma_u^+$ (triplet) with $\nu = 0$ to the ground state ${}^1\Sigma_g^+$. Since a direct transition from the triplet state ${}^3\Sigma_u^+$ is forbidden the decay happens through a mixing state between ${}^3\Sigma_u^+$ and ${}^1\Pi_u$ through spin-orbit coupling. This gives rise to the decay time of the triplet state. For alpha particles in LXe the singlet state has a decay time of 4.3 ns while the triplet state is reported to have 22 ns [CA13]. The decay times give slightly different values when measured for electrons instead of alphas and also the partitioning of the fast and the slow component is particle and energy dependent. Despite the different decay times the scintillation light coming from these decays is spectroscopically indifferent. There is however a difference in the emission spectra between gaseous and liquid xenon as shown in figure 4.6. GXe emits scintillation light at a mean wavelength of 175 nm while in LXe it is 178 nm.

The second process involved in the light production is the recombination of electrons e^- with xenon ions Xe^+. Here, also a cascade of interim steps involving the scattering

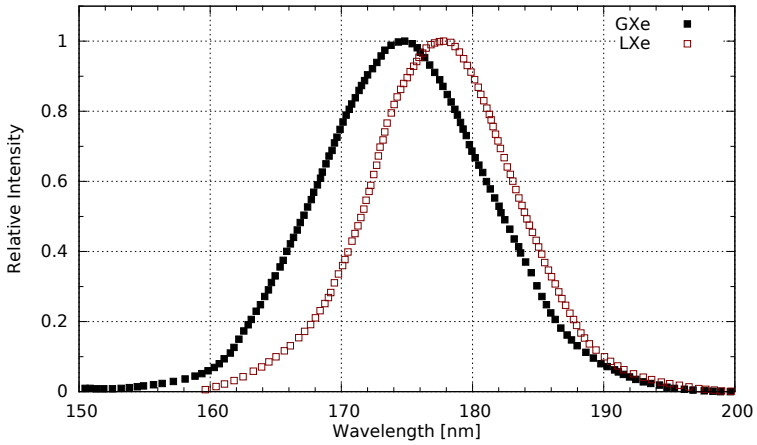

Figure 4.6.: Emission spectra for liquid and gaseous xenon. The peak wavelength of scintillation light for LXe is at 178 nm, while in GXe photons with 175 nm are produced. From [Jor+65]

with other xenon atoms is necessary:

$$Xe^+ + Xe + Xe \rightarrow Xe_2^+ + Xe \qquad \text{molecular ion formation} \qquad (4.18)$$

$$e^- + Xe_2^+ \rightarrow Xe^{**} + Xe \qquad \text{recombination} \qquad (4.19)$$

$$Xe^{**} + Xe \rightarrow Xe^* + Xe + heat \qquad \text{deexcitation} \qquad (4.20)$$

$$Xe^* + Xe + Xe \rightarrow Xe_2^* + Xe + heat \qquad \text{excimer formation} \qquad (4.21)$$

$$Xe_2^* \rightarrow Xe + Xe + h\nu \qquad \text{VUV light emission} \qquad (4.22)$$

In the first step molecular ions are formed only picoseconds after the ionization of atoms by a passing particle. The last process in the cascade is very similar to direct excitation and wavelength and decay times are the same as well. However, the ratio of occupied states is different. For alpha particles in LXe about 31 % of the scintillation light originates from the decay of the singlet state and 69 % from the triplet state. The recombination time is shorter than the decay time of excited dimers. This circumstance and the fact that alpha particles have higher ionization densities – and that recombination cannot be prevented completely even for field strengths higher than 10 keV/cm – make it impossible to experimentally distinguish the two scintillation mechanisms. On the other hand the high density of LXe causes alpha particles to have a very short track length which means light emitted along the path of the particle can be approximately seen as a point source. If charge carriers are drifted, higher ionization density also leads to a better spacial resolution making LXe a very good detector medium for a TPC.
[CA13]

4.3.3. Noble Element Simulation Technique

For the simulation of light production in liquid and gaseous xenon a comprehensive model for scintillation light in liquid xenon was used, called *Noble Element Simulation Technique* (NEST). It contains all processes involving electrons as well as nuclear recoils and is designed as an add-on for GEANT4. An advantage of NEST claimed by Szydagis et al. (2011) is that this model is able to treat other media as well by a change of only few parameters. It takes care of the fact that the scintillation light yield has a non-monotonic dependency on stopping power especially for lower energies. It is able to deal with different particles and energies and is capable of estimating the recombination probability depending on electric field (if applied), path length and ionization density of the track. NEST does not implement the complex processes of recombination and de-excitation in detail but uses models to calculate the number of produced electrons and photons.

Energy loss as heat or due to sub-excitation electrons is compensated in a higher value for E_i. NEST includes an energy dependent light yield. One reason for this dependency is the distribution of the ionization electrons between escape and recombination. These processes vary with particle energy and stopping power. As mentioned in 4.3.1 the more electron-ion pairs recombine the more light is produced (anti-correlation) [Szy+11].

The number of produced photons is calculated using a fixed excitation to ionization ratio α of 0.06 and a value of 13.7 eV as joint mean efficiency W (also called *work function* in the first paper of NEST, 2011 [Szy+11]) for both the production of an electron-ion pair and an excited atom so that

$$E_0 = W(N_{ex} + N_i) \tag{4.23}$$

This makes sense, since it is also the minimum required energy to produce a scintillation photon if recombination is assumed to be 100 % and no other effects limit the yield (compare equation 4.14). The exact value for W originates Fano statistics, while N_{ex} is chosen based on α and a binomial distribution. The total number of photons produced by NEST is then described as

$$N_{ph} = N_{ex} + r\,N_i \tag{4.24}$$

$$\Rightarrow N_{\text{electrons}} = N_i + N_{ex} - N_{ph} = N_i(1 - r) \tag{4.25}$$

with r the recombination probability. $N_{\text{electrons}}$ denotes the number of free electrons that escaped the recombination process. In experiments including electron drift, escape electrons give rise to the charge read out signal and therefore lower the light yield.

The choice of models used to determine the recombination probability r depends on the track length. For long particle tracks a model by Doke et al. is used based on Birks' law from 1964. The recombination probability is expressed as follows:

$$r = \frac{A \cdot \left|\frac{\mathrm{d}E}{\mathrm{d}x}\right|}{1 + B \cdot \left|\frac{\mathrm{d}E}{\mathrm{d}x}\right|} + C = \frac{A \cdot S}{1 + B \cdot S} + C \tag{4.26}$$

$$\lim_{S \to \infty} r = 1 \quad \Leftrightarrow \quad C = 1 - \frac{A}{B} \tag{4.27}$$

The first term in equation (4.26) describes the recombination of an electron with an ion other than the parent ion somewhere along the particle track or in the "ionization cloud". This is also referred to as *volume recombination*, whereas the second part is called *Onsager recombination* and represents recombination of the electron with its own parent ion. This process is assigned a fixed probability which is independent of $\mathrm{d}E/\mathrm{d}x$. Yet, there is always a certain amount of electrons that are able to escape the Coulomb field of the ionized xenon atoms even if no field is applied. However, this fraction is very small for high stopping powers (ergo alpha particles) due to a higher ionization density. For comparison, for gammas of 122 keV about 10 % of the ionization electrons will not recombine.

In LXe as well as GXe alpha particles have high stopping powers as can be seen in figure 4.1 from section 4.1.3 which results in a high recombination probability with a peak value of 99.7 % and at least 95 % throughout the track (compare figure 4.7) except the very last few micrometers where the energy drops to zero and the recombination becomes independent of ionization density. This justifies the neglection of r in equation 4.13 in connection with energy dissipation of alpha particles in xenon.

For track lengths smaller than the mean ionization electron-ion thermalization distance the *Thomas-Imel box model* is used. This is the average path length of a secondary electron that does not have enough energy to produce an electron-ion pair and dissipates its energy via elastic scattering. The electron keeps loosing energy until the point of thermodynamic equilibrium with the surrounding medium is reached [Apr+07]. This distance is fixed to 4.6 μm in the NEST model. Here, the recombination is calculated in the following way:

$$r = 1 - \frac{\ln(1 + \xi)}{\xi}, \quad \text{where} \quad \xi = \frac{N_i \, e^2}{4 \, a \epsilon k T} \tag{4.28}$$

N_i is the number of created electron-ion pairs, ϵ is the dielectric constant and e is the electron charge. a describes the length scale of the ionization density volume, k is Boltzmann's constant and T is the temperature. While Doke's model depends on the stopping power S(E), Thomas-Imel is independent of both S as well as the actual track length. For low energies recombination becomes independent of ionization density. This is accommodated in the Thomas-Imel model where recombination probability depends on the energy via number of ions and not on $\mathrm{d}E/\mathrm{d}x$. Therefore, the track length is irrelevant if it is smaller than the thermalization density of ionization electrons.

The understanding of light yield (and therefore, r) is important not only for double beta decay experiments but also for dark matter search – especially in the low energy range. This is the region of interest containing the largest part of the spectrum for NR and WIMPs (Weakly Interactive Massive Particle). [Szy+11]

However, there might be some limitations regarding the applicability of NEST to the simulation of alpha particles in LXe and GXe. The main reason is that NEST was designed and tested for gammas and electrons in liquid xenon and its reliability of reproducing values cited in literature (like scintillation light yield) was confirmed mainly for low energy recoil regions that are interesting for dark matter experiments using dense noble gases as a detector medium. Therefore, in this work alpha particles with energies in the MeV range have caused problems with producing sensible numbers of photons when the model was first applied to the code which made some alterations necessary. Another reason is the use of a fixed value of $\alpha = 0.06$ which is arguably consistent with literature especially for xenon gas [Mim+09]. Also, the point at which a track length is switched from being considered *long* and treated by Doke's model to being *short* and processed by Thomas-Imel model is a fixed distance of 4.6 μm. That value is used for gammas in LXe and might need to be changed for other particles and different conditions of media.

The following paragraph summarizes processes an optical photon undergoes while propagating in the chamber and outlines surface reflections until section 4.4 discusses a series of tests of the physical validity of the simulated processes and of the applicability of NEST to alpha particles in xenon gas or liquid.

4.3.4. Optical Processes

The major unknown quantity that is potentially influencing any measurement in the set-up is the amount of reflections from copper wall and aluminum holder. Problems with simulating the interaction of scintillation light with dielectric boundaries is no unknown problem: Levin et al. 1996 already reported a "lack of realism and flexibility in dealing with the surface finish and reflector coating of photon counters" [LM96]. In case of the Erlangen set-up material and geometric dimensions of both surfaces are well known, but not their purity and the texture of the surface. Although the material was polished and cleaned thoroughly before placed inside the experiment, the microscopic structure is unknown which decides if specular or diffuse reflection takes place. Also, after a SiPM characterization was performed and the xenon gas was removed the surface seemed to have changed due to dust or deposit of dirt. It might, therefore, be possible that surface and reflection properties have changed during a measurement. One can summarize the task as follows:

Both surfaces have unknown properties that furthermore change during the duration of a measurement but nevertheless need to be treated by the simulation as realistically as possible. This is to check, if and to what extend the surface properties influence the

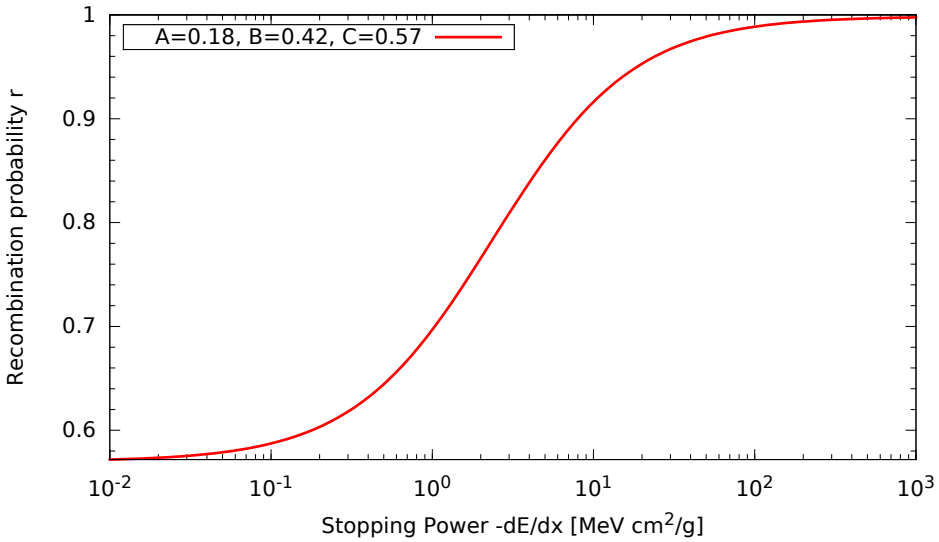

Figure 4.7.: Recombination probability r according to equation (4.26) described by Doke's model for zero electric field (from [Szy+11]). For alpha particles in the MeV range r is larger than 95 % for almost the whole track length (Compare also figures 4.1 and 4.2).

light yield on the detectors and the ratio of the photon fluxes R. Therefore, a mixture of educated assumptions and the test of various parameter combinations is applied to the implementation of optical processes.

GEANT4 provides a set of configuration options the user can choose from. The type of surface was set to *dielectric-metal* for the interface between xenon and copper or aluminum respectively. The surface model called UNIFIED was chosen to describe the optical processes at the boundaries and manage their finish type. It can be loaded via `G4MaterialPropertiesTable` and assigned to a surface. This model was originally designed for DETECT a Monte-Carlo simulation for modelling the optics of scintillation detectors. It was optimised for purely dielectric boundaries but provides the possibility to simulate optics on metal surfaces to some extend as well. It is capable of dealing with micro-facets and the simulation of a wide range of surface roughness values [LM96].

It should be noted that a surface in GEANT4 is always defined as a boundary between two media including a direction of incidence. The direction defines from which side of the boundary optical photons arrive at the surface. Of course, in the case of copper and aluminum photons approach the surface only from the xenon medium and never from the metal, but for a purely dielectric boundary the transition from either way must be implemented separately. [Col]

To treat the finish of the surface the user can chose between *ground*, a setting for rather diffuse reflections and *polished* which implements specular reflections. The latter one is used if the surface is "perfectly polished" [LM96] and can be considered smooth

which means that irregularities in the surface are small compared to the wavelength of the light. Then the angle of incident light equals the reflected one. A diffuse reflection occurs for surfaces that are rough compared to the wavelength. However, real surfaces always posses a surface behaviour in between these two extremes [Hec98; Col]. In the finish *ground* which was finally chosen for the simulation a mixture of backscattering, diffuse and specular reflection is implemented. Since the exact type of reflection is not known – especially because of the temporal change during a measurement – the ability of the materials to reflect or absorb optical photons was controlled via reflectance settings of the material.

For a description of the reflection properties of a surface one firstly has to consider the power of light arriving on an area A under an angle of incidence θ_i. It is described as

$$P_i = I_i \, A \, \cos\theta_i \,, \tag{4.29}$$

where I_i is the radiant flux and expressed as

$$I_i = v_i \, \varepsilon_i \, E_{0,i}^2/2 \tag{4.30}$$

with ε_i the permittivity of the medium (here: Xenon), v_i the speed of light in that medium and $E_{0,i}$ the amplitude of the field vector of the incident electro-magnetic wave. The *reflectance* $\mathcal{R}$[1] of a surface is defined as the ratio of reflected to incident power as follows:

$$\mathcal{R} = \frac{P_r}{P_i} = \frac{I_r \, A \, \cos\theta_r}{I_i \, A \, \cos\theta_i} = \frac{I_r}{I_i} \tag{4.31}$$

incident and reflected power are considered with respect to the same area A and the wave is reflected back into the same medium. According to *Snellius' Law* incident and reflected angle are equal ($\theta_r = \theta_i$). Furthermore, one can express $I_{r/i}$ in terms of the electric field amplitude using (4.30) and the fact that $v_i = v_r$ and $\varepsilon_i = \varepsilon_r$. Then, the reflectance reads:

$$\mathcal{R} = \left(\frac{v_r \, \varepsilon_r \, E_{0,r}^2/2}{v_i \, \varepsilon_i \, E_{0,i}^2/2} \right) = \left(\frac{E_{0,r}}{E_{0,i}} \right)^2 = \rho^2 \tag{4.32}$$

ρ denotes the *amplitude reflection coefficient* and can be split up into two components ($\rho_\perp$, $\rho_\parallel$) regarding the polarization of the incident field. $\rho_\perp$ ($\rho_\parallel$) is the ratio of reflected to incident amplitude treating only the perpendicularly (parallel) polarized part of the electric field. The coefficients can be calculated using *Fresnel Equations*.
The corresponding components of the reflectance are subsequently expressed as:

$$\mathcal{R}_\perp = \rho_\perp^2 \qquad \mathcal{R}_\parallel = \rho_\parallel^2 \tag{4.33}$$

In GEANT4 a scintillation photon is emitted with a random linear polarization [Col]. That means on average over many photons scintillation light is unpolarized or in other

[1] A distinction has to be made between the reflectance $\mathcal{R}$ and the photon flux ratio R.

words perpendicular and parallel polarized components occur in an equal presence. For the reflectance the following relation then holds:

$$\mathcal{R} = \frac{1}{2}(\mathcal{R}_\perp + \mathcal{R}_\parallel) \tag{4.34}$$

In the case of two dielectric media the above set of equations could also be set for the *transmittance* $\mathcal{T}$ analogously which would cover the part of the light that is transmitted through the surface so that

$$\mathcal{R} + \mathcal{T} = 1 \tag{4.35}$$

[Hec98]
However copper and aluminum are not considered optical media so that $\mathcal{T}$ can be seen as the fraction of incident light getting absorbed at the boundary. This is compensated in both finish settings *polished* as well as *ground* which reflect or absorb photons according to the entered setting (no refraction takes place). In GEANT4 the quantity $\mathcal{R}$ is defined in the material properties as "REFLECTIVITY" and can be set by entering a value between 0 and 1.0 (i.e. 0 % 100 %). This means that each incident photon is reflected with a certain probability according to the entered value for "REFLECTIVITY" and the chosen surface model and finish. [Col; Hec98]

To check the influence of the reflectance (or reflectivity as it is called in GEANT4) on the photon flux ratio various combinations of reflection parameters $\mathcal{R}$ were tested in the simulation. Performance and analysis of this procedure can be found in chapter 5.

4.4. Discussion of physical validity

The simulation has to comply with certain requirements in order to represent and reproduce a measurement in the real experimental set-up. Therefore, in this chapter a series of test runs is performed and analysed with regard to important quantities like the number and the energy of emitted photons. Also, the behaviour of the simulation under variation of conditions like gas density and particle energy is investigated and compared to cited literature to proof the physical reliability and validity of the program.

4.4.1. Topology of the Distribution of Measurement Points

At first, the basic properties of a measurement and the general topology of the distribution of the data points is explained. For each alpha particle emitted from the source into the xenon, scintillation light is produced according to section 4.3. The detectors count all photons that hit their sensitive areas. For the purpose of determining the photon flux ratio R both detectors have 100 % sensitivity, i.e. every photon is counted. In a first data analysis a so called *scatter plot* is created where the SiPM signal is

plotted against the PMT count of each event. A histogram of the photon counts on a detector in each event is also useful for understanding of the measurement signals. In figure 4.8 the scatter plot for a simulation of alpha particles in gaseous xenon of 1.1 bar is shown. The particles have energies of 4.15 MeV, 4.48 MeV and 4.80 MeV representing the three isotopes the source consists of (for details on the source see section 3.2.2). 25000 events have been simulated each of which is represented by a point in the graph. Reflectivities were set to zero for all runs in this section. Their influence on the measurements is discussed in chapter 5 in all detail. The corresponding PMT histogram can be seen as well to exemplary show the distribution of the photon numbers on a detector surface. In the simulation as well as in the measurements in the actual experiment a distinct, characteristic topology of the distribution of data points was observed: An accumulation on the right showing an anti-correlated structure and a smaller pile up at the lower photon count region. The anti-correlation between SiPM and PMT photon count can be explained mostly by the trajectory of the alpha particle of up to 1.84 cm at these conditions. The PMT photon count is increased if the alpha travels towards its sensitive area giving a decrease to the SiPM signal and vice versa. But also the expansion of the circular source of 0.5 cm contributes to the anti-correlation. This was explained in detail in section 3.3 already and can be retraced when looking at the scatter plot for LXe (figure 4.9): Although the alpha particle trajectory is very short (between 31.24 μm and 37.50 μm) and the photons can be considered as coming from a point source, there is an anti-correlation in the SiPM-to-PMT counts. The only explanation for this behaviour is the expansion of the source, since the different solid angles of the detector or in general the asymmetric positioning of detectors only influence the photon flux ratio but do not introduce a certain topology to the distribution. Depending on the start position of the alpha particle the distance to the center point of the SiPM surface for instance varies by more than 2 mm. Since the flux on a detector scales with the inverse of the distance squared this imposes a small but significant flux difference.

The accumulation on the left lower end of the graph can only be seen for gaseous xenon. A simple explanation is the presence of the aluminum holder and especially its edge. As seen in picture 4.10 a certain amount of alpha particles is emitted directly towards the edge of the holder and is absorbed there transferring its kinetic energy to the material. The track length of these particles is limited and therefore the scintillation yield and the total number of emitted photons is smaller. This plays an important role when analysing the photon flux ratio in the next chapter 5. There is no anti-correlation in the left accumulation since the track length varies depending on the start position of the alpha. Furthermore, alphas that are scattered downwards into the aluminum could be stopped earlier than others. The number of photons produced by one of these alphas therefore varies (see also figure 4.12) and the anti-correlation is only seen in the right cluster.

Finally one observes horizontal lines in both graphs for GXe and LXe originating in the discreetness of photon numbers. This structure exists for both detectors but is

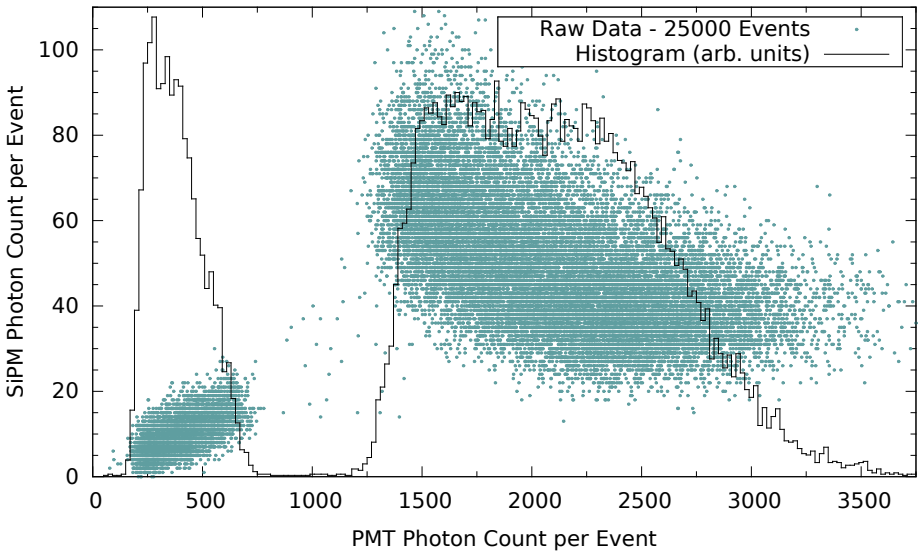

Figure 4.8.: Scatterplot of photon counts on SiPM and PMT in GXe with raw data of 25000 simulated events without any surface reflections. Each point represents one event. The general topology of a measurement can be seen in the two clusters and in the shape of the histogram of the PMT counts.

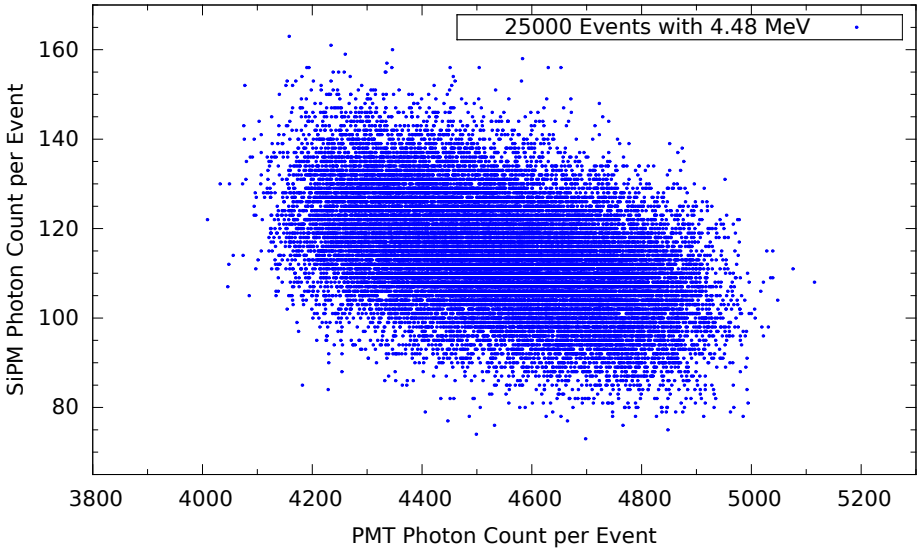

Figure 4.9.: Scatterplot of photon counts on SiPM and PMT in LXe with raw data of 25000 simulated events without any surface reflections. Each point represents one event. The general topology of a measurement can be seen in the two clusters and in the shape of the histogram of the PMT counts.

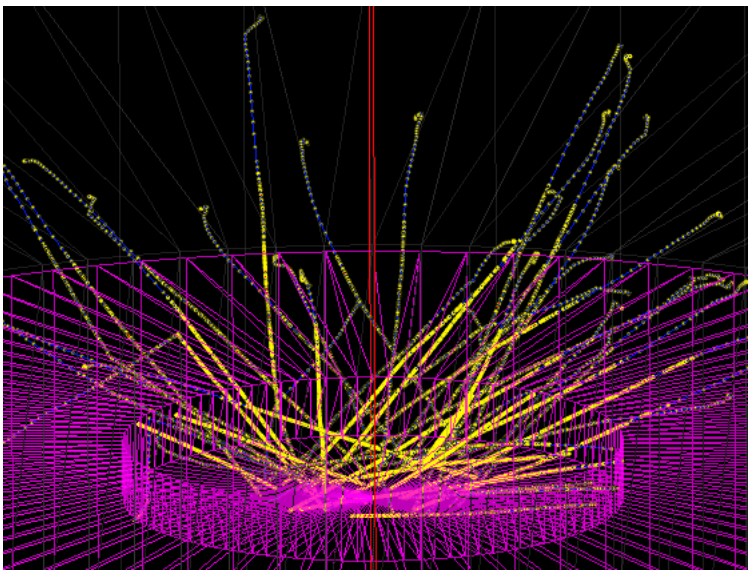

Figure 4.10.: Alpha particles emitted from the aluminum holder simulated in GEANT4. A significant fraction of tracks has limited path length: The alpha is stopped by the edge of the holder.

only visible for the SiPM since the PMT counts are much higher and the discrete structure can not be resolved in this depiction.

4.4.2. Energy Dependencies

The particle's energy has an influence on several important quantities: The number of photons that are produced by an alpha particle and the total covered path length until the alpha is absorbed by the medium. Furthermore, it has an impact on the shape of both the scatter plot and the histograms. Using three different energies of alpha particles causes a broadening of the right peak and a shift towards higher photon numbers. This is shown in figure 4.11: Again 25000 events were simulated with the partitioning of the energies according to their abundance in the source (40.5 % ^{239}Pu (4.15 MeV), 47.7 % ^{241}Am (4.48 MeV) and 12.1 % ^{244}Cm (4.80 MeV)).

The higher the particle's energy the more photons are produced according to equation 4.14. In figure 4.12 the number of produced photons per event is plotted as a histogram. The peak height represents the abundance of the corresponding isotope. The simulation reproduces the fact that a higher particle energy gives rise to the number of produced photons. Exact values for the number of photons are given in section 4.4.3 together with a discussion of the density dependency. Furthermore, a scatter plot for the SiPM count and PMT count respectively versus total number of produced photons is shown. It can be seen that for higher energies more photons are counted. Moreover, it can show the continuously varying number of photons for the left accumulation, i.e. for

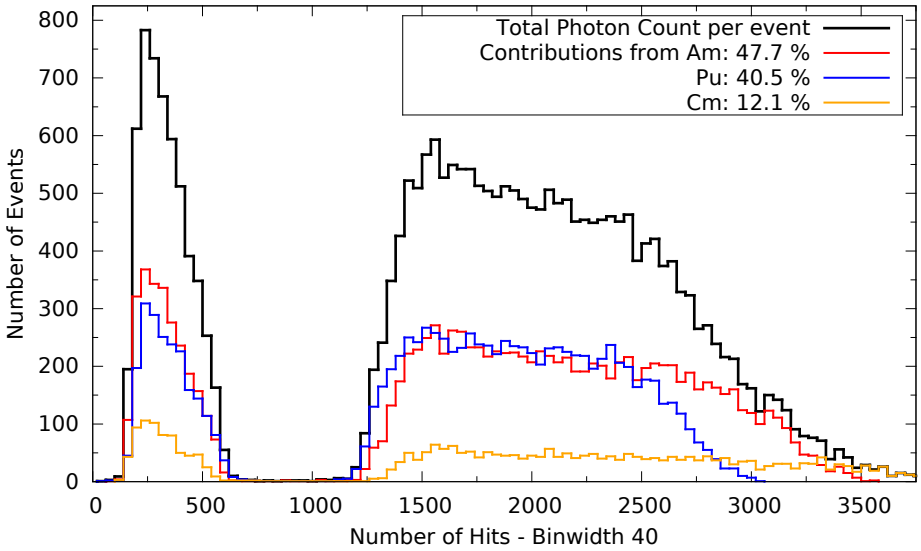

Figure 4.11.: Different energies of the alpha particle from the three different isotopes ^{239}Pu (4.15 MeV), ^{241}Am (4.48 MeV) and ^{244}Cm (4.80 MeV) and each of their contribution to the total photon count on the PMT.

tracks with limited range due to the aluminum holder. A last significant structure in this scatter plot can be found in the vertical pile ups on the right side of each graph where the alphas could travel the total distance: Measurement points at the lower end of the accumulation correspond to alpha trajectories that were directed away from that detector lowering its count, while points at the top show photon counts from events where the alpha particle travelled towards that detector increasing the count.

The third energy dependence mentioned at the start of this paragraph is the track length. Table 4.3 shows the ranges of alpha particles of the three energies in GXe at 1.1 bar and in LXe and compares the simulation to the calculated expectation (from [Ber+05a]). In both media the range only deviates a few percent from the calculations. It can be seen that higher energies result in larger ranges. This implies a stronger anti-correlation of the SiPM and PMT photon count for higher energies and causes the right peak in the histogram (figure 4.11) to be broadened. Since all three energies are used for experiment and simulation the anti-correlation is to some extent "washed out". However, alpha ranges in xenon gas also strongly depend on the density of the gas. Its influence on the measurement is outlined in the following paragraph.

4.4.3. Density Dependencies

The distance alpha particles can travel in xenon gas decreases for higher densities. In the actual experiment a pressure of 1.1 bar is used. According to the ideal gas law this results in a density of $6.4878 \cdot 10^{-3}\,\mathrm{g/cm^3}$. For these conditions an expectation value of 1.588 cm could be calculated using values for the ranges from the NIST database

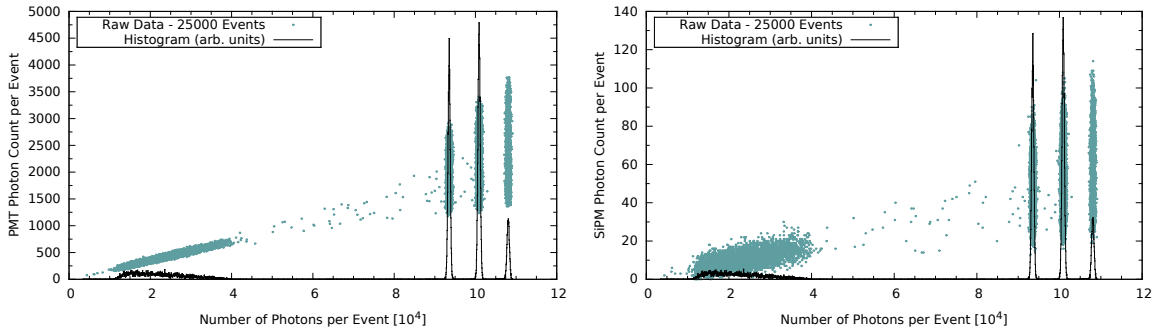

Figure 4.12.: Number of photons counted by the PMT (left) and the SiPM respectively in xenon gas. The number of photons produced per event correspond to the three different energies of the alpha particle. The heights of the peaks in the histogram represent the occurrence of the isotopes each of which emits alphas of a different energy. Values of the left pile up correspond to ranges that were limited by the aluminum holder.

	Gaseous Xenon			**Liquid Xenon**		
Energy [MeV]	Exp [cm]	Sim [cm]	Dev [%]	Exp [μm]	Sim [μm]	Dev [%]
4.15	1.44	1.52	5.5	31.2	29.8	4.5
4.48	1.59	1.68	5.9	34.4	33.2	3.3
4.80	1.73	1.84	6.1	37.5	36.7	2.3

Table 4.3.: Ranges of alpha particles in xenon gas at 1.1 bar and in liquid xenon at 1 bar. Values from the simulation are compared to the expectations according to NIST database [Ber+05a].

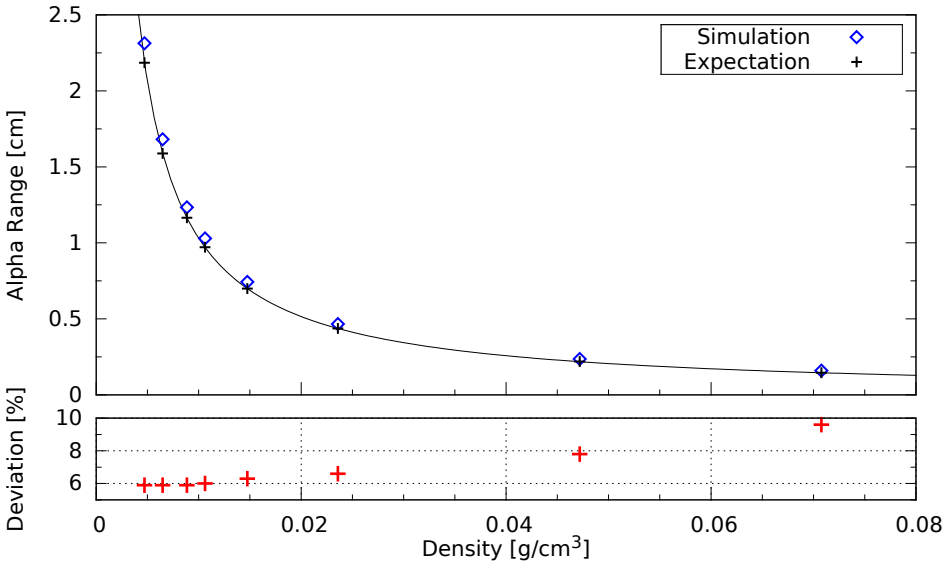

Figure 4.13.: Ranges of simulated alpha particles with 4.48 MeV in xenon gas. A reciprocal dependency of the range on the density can be obtained consistent with the calculated expectation especially in the lower density range that is of interest in this work (data for reference taken from [Ber+05a]).

(compare figure 4.1). In general an inverse relation between density and particle range is expected which is shown in figure 4.13. Ranges of simulated events for 8 different densities are compared to the expectation values each of which consists of 10000 alpha particles with an energy of 4.48 MeV. For this simulation alpha particles were strictly emitted upwards so that all alphas have their full range and are not stopped by the aluminum holder. Deviations of the ranges from the data base values are in the lower percent region – especially for the density of interest. The reciprocal relation between density and range can be well reproduced.

The density of the gas also has an impact on the total number of photons that are produced by an incoming particle. However, an exact estimation of the number of produced photons is difficult for several reasons: In literature no consistent values for the scintillation yield (produced photons per deposited energy) can be found. Often the inverse of the scintillation yield is used to quantify the efficiency of light production which is a measure for the mean energy required to produce a scintillation photon and is given in electron volts. It was also referred to as work function by Szydagis et al. [Szy+11] (compare equation 4.23). While Saito et al (2002) [Sai+02] report an efficiency of 34.3 eV at a pressure of 1.01 bar ($6.05 \cdot 10^{-3}$ g/cm^3), Miyajima et al. (2004) [SNM04] give a value of 49.6 eV under similar conditions. Their values as well as contributions by Mimura et al. (2009) are shown in graph 4.14 together with results from the simulation: At a density of 6.48 g/cm^3 a photon number of 100880 ± 15.14 was obtained for 5100 alphas with 4.48 MeV. For energies of 5.49 MeV the mean photon number per event was 123235 ± 13.19 using the same amount of events. Both results

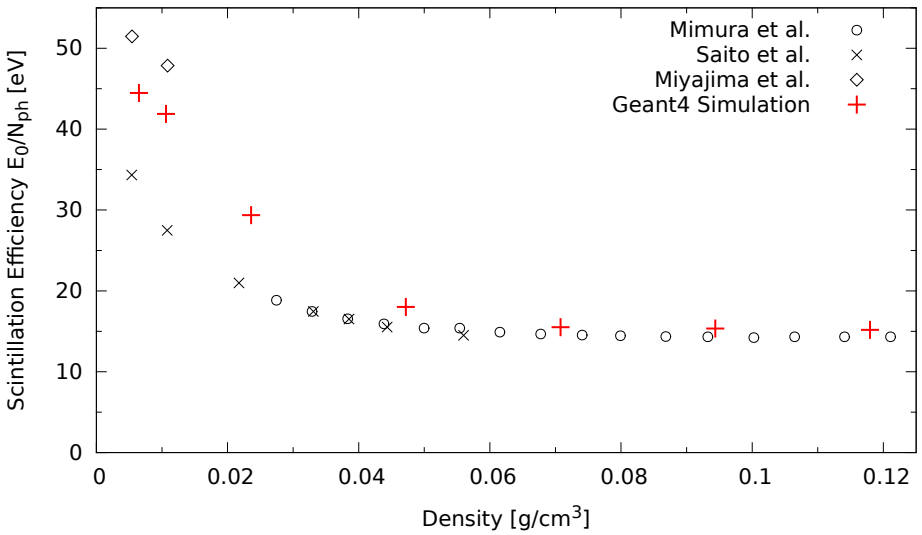

Figure 4.14.: Scintillation efficiency (mean energy required to produce a scintillation photon: E_0/N_{ph}) depending on the density. Shown are measurements by Mimura et al. (2009) [Mim+09], Saito et al. (2002) [Sai+02] and Miyajima et al. (2004) [SNM04] as well as the values obtained by the simulation.

combined yield an efficiency of 44.5 eV.

Another reason why photon numbers in GXe are hard to estimate is because there is no reliable average energy expended per excited atom in gaseous xenon even at low densities as used in this work due to inconsistent values reported in cited literature [Mim+09]. Furthermore, according to Bolotnikov et al. (1999) the partitioning of the energy in excited atoms N_{ex} and produced electron-ion pairs N_i varies with the density of the gas as well [BR99]. This value of partitioning was denoted with the greek letter α earlier in this work and was introduced in paragraph 4.3.1.

Another comparison of the results obtained by the simulation to measurements performed by Kobayashi et al. (2004) and Bolotnikov et al. (1999) yields that the simulation reproduces the general dependency of the number of produced photons very well. Both research groups used alpha particles of 5.49 Mev and determined the number of scintillation photons for a large density range up to 0.55 g/cm^3. A comparison of their measurements to the simulation is shown in figure 4.15.

Luckily, knowing the exact number of photons produced by alpha particles in xenon gas at certain conditions is not necessary. Since only a comparison of photon fluxes on the sensitive detector areas is performed, knowing and precisely recreating the correct photon number is not mandatory. Using a sufficiently high number of events for the simulation compensates for eventual statistical fluctuations that might occur if the number of photons was significantly lower than in the real experiment. Also, it is

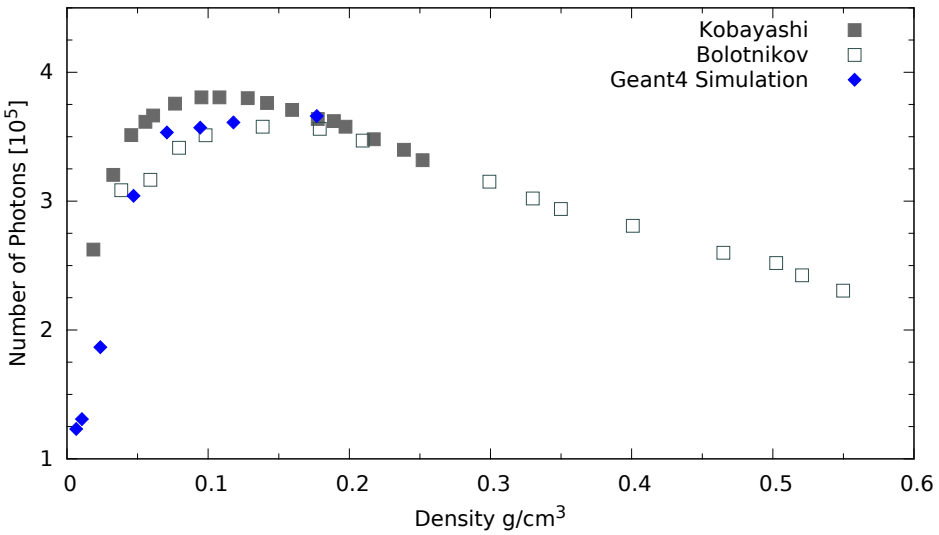

Figure 4.15.: Density dependence of the total number of produced photons in high density xenon gas. Measurements by Kobayashi (2004) [Kob+04] and Bolotnikov (1999) [BR99] using alphas with 5.49 MeV are compared to simulated values.

almost impossible to make assumptions on the xenon impurity in the chamber which limits the mean free path length of photons in the medium. For details see section 4.2.1. Therefore, the default values and settings in the NEST code were taken to simulate alpha particles in xenon gas leading to the above results for photon numbers.

A variation in pressure also causes a change in the topology of a measurement that was introduced earlier in this section. Figure 4.16 shows the simulation of 25000 events in GXe for either 1.1 bar and 1.8 bar which corresponds to densities of 5.898 g/cm^3 and 6.4878 g/cm^3 respectively. Two aspects of density dependence that were mentioned in this paragraph take effect here: Firstly, a higher density means shorter track length which implies a weaker anti-correlation. This can be seen in the right pile up where the measurement points are drawn closer together for higher density (in red colour). If density is increased even further both "blobs" would eventually merge resulting in a topology similar to LXe. The second aspect is the increased number of scintillation photons for higher density manifesting in the accumulations being shifted towards higher photon counts.

For liquid xenon a constant density of 3.0 g/cm^3 is used. At this density a number of 260329 ± 16 photons was obtained in the simulation of alphas with 4.48 MeV. This is in good consistency with literature: Aprile et al. (2010) report a value for W_{ph}^{α} of 17.9 MeV [AD10] which equals a number of 250279 produced photons. The number from the simulation is about 4 % above this value. However, Chepel (2013) et al. provide a value of $W_{ph}^{\alpha} = 17.1$ MeV resulting in a number of 261988 photons lowering

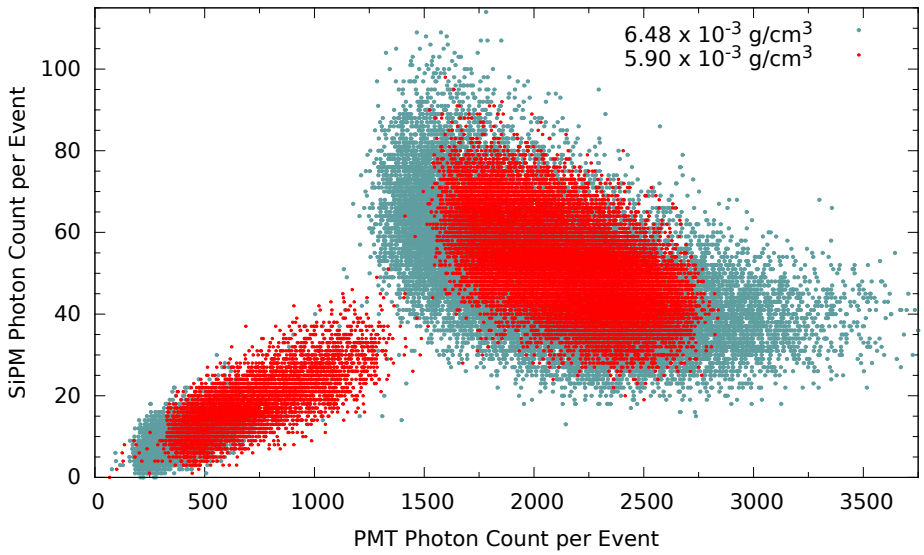

Figure 4.16.: Comparison of two simulations using different density. The number of scintillation photons increases for higher density which can be seen in the left accumulation. For 1.8 bar (corresponding to 6.4878 g/cm^3) the anti-correlation is not as incisive as for 1.1 bar (5.898 g/cm^3) causing the points in the right pile up to be drawn closer together.

the deviation of the simulation to less than 1 %.

4.4.4. Photon Wavelength of Simulated Scintillation Light

The produced scintillation light has wavelengths which are in good consistency with the expected values: In LXe photons with a mean wavelength of 177.7 nm are emitted while Jortner et al. (1965) measure a peak value of 178 nm. In GXe the simulation produces on average photons with 174.5 nm which is consistent with the expectation of 175 nm [Jor+65] (figure 4.6). The energies of the photons produced in LXe and GXe of one event are shown in figure 4.17.

Summary:
It could be shown that the simulation of alpha particles in xenon together with the production and propagation of scintillation light is capable of reconstructing the conditions of the actual experiment within the boundaries of expectations. Energy and density dependencies are reproduced correctly with only little deviation. The wavelength of scintillation light matches experimental results. A comparison of the number of produced photons with expectations is difficult due to inconsistent values given in cited literature. The extraordinary shape of the distribution of simulated measurement points could be explained by alpha particles stopped by the aluminum holder. These test results justify a reliable applicability of the simulation for the

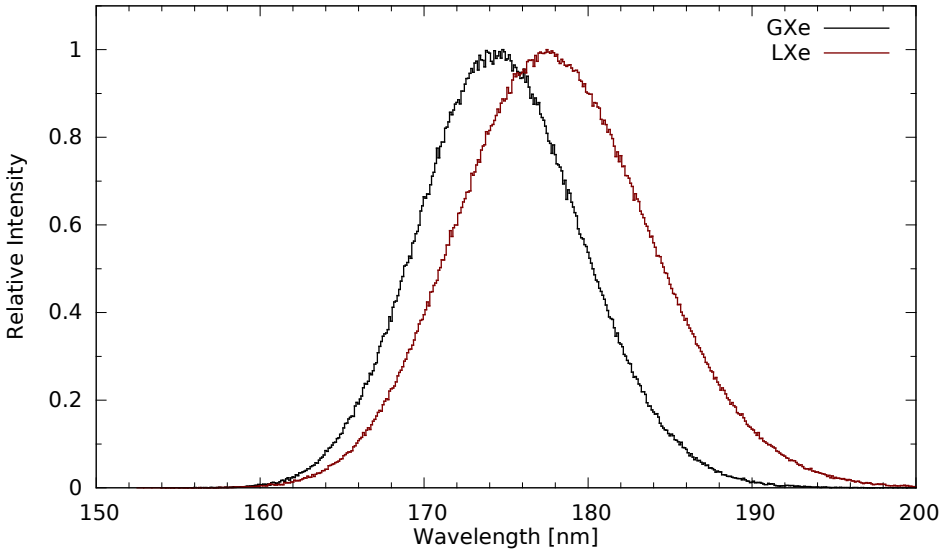

Figure 4.17.: Wavelengths of scintillation light in liquid and gaseous xenon. The peaks' wavelengths are at 174.5 nm for GXe and 177.7 nm for LXe in good consistency with literature [Jor+65] (Compare figure 4.6).

determination of the photon flux ratio. Performance and analysis of this procedure is explained and discussed in the following chapter.

5. Performance and Analysis

5.1. General Overview

In section 3.3 the problem of inequivalent photon flux was introduced and is briefly recapped in this paragraph.
Due to the asymmetry of the set-up as well as the different solid angles of the sensitive detector surfaces, the average flux on the PMT is higher than the one on the SiPM. An additional deviation in the photon fluxes on both detectors originates from the trajectory of the alpha particle and the fact that photons are produced all along its flight path. Therefore, the direction of flight of the alpha particle has a significant influence on the number of photons hitting each of the detectors. Furthermore, the alpha source on the bottom of the chamber from where the particles are randomly emitted has an expansion which contributes to the asymmetric character of the set-up. In addition to this the influence on a change of photon flux due to reflections from the wall and the bottom of the chamber can merely be estimated since the reflection properties of the surfaces are unknown.

The process of determining the *photon detection efficiency* (PDE) explained in section 3.3 requires that the photon fluxes on both sensitive areas can be assessed in relation to each other. A correction factor R therefore is needed to enable a reliable calculation of the PDE using formula (3.8) derived in section 3.3. By definition this factor expresses the ratio of the actual photon fluxes $\frac{\Phi_{\mathrm{SiPM}}}{\Phi_{\mathrm{PMT}}}$ (equation (3.7)). In the following the process of determining R with help of the simulation is described.

Since the photon flux ratio can not be measured or calculated for given reasons it has to be simulated so that:

$$\frac{F_{\mathrm{SiPM}}}{F_{\mathrm{PMT}}} = \frac{\Phi_{\mathrm{SiPM}}}{\Phi_{PMT}} =: R \tag{5.1}$$

where $\Phi_{\mathrm{SiPM/PMT}}$ denotes the total photon flux on SiPM or PMT respectively as it occurs in the experiment and $F_{SiPM/PMT}$ is the flux simulated in GEANT4 which are equally defined as the number of photons P impinging on the detector area A. Under consideration of equation (3.7) this supposition leads to the required correction factor R.

The largest uncertainties in this optical set-up originate in the unknown reflectivities of both the copper wall and the aluminum holder. Their influence on the photon flux

and especially the flux ratio is determined in the next section, before eventually the correction factor R is simulated. A further investigation is focused on the application of this factor to determine the detection efficiency of SiPMs according to the method introduced in chapter (3.3). The basic analytic principles in this work apply to liquid as well as gaseous xenon but since experimental data exist only in gas phase yet the next paragraphs mainly concentrate on simulations in GXe at a pressure of 1.1 bar.

5.2. Influence of Surface Reflections on the Photon Flux

The first step in the surface investigation was to get an overview of how the outcome of a measurement varies if the surface properties inside the xenon cell are changed. Therefore, 25000 alpha events were simulated, each of which produced about 10^5 photons in gaseous Xenon (compare section 4.4). The photon flux on each detector surface was investigated by counting all photons reaching the sensitive part of that detector. This was done for various reflectivities. Thus, a comparison of the simulated PMT- and SiPM-signal for different reflection configurations is possible.

For this purpose, the interface MARCI (for details see section 4.1.5) manages corresponding counters for each detector and each run and passes them to the read out process where histograms are created automatically once a run has ended. As an example, figure (5.1) shows the histogram for the PMT in gaseous xenon without any surface reflections, i.e. both the reflections of copper wall and aluminum holder were set to zero and every photon hitting these surfaces was absorbed. The left peak corresponds to alpha tracks stopped by the aluminum holder and, therefore, not having full scintillation yield while the right peak forms a plateau-like structure which originates from the three different energies of the alpha particles as well as the expansion of the source. Alpha particles with only one energy produce a narrower peak as was shown in section 4.4.

In this first analysis the reflectivity of the copper wall was varied between 0 % and 100 % in steps of 20 % and the change in detector response was observed. Again, histograms were created for PMT (figure 5.2) as well as for SiPM photon counts (figure 5.3). By increasing the reflections of the surface the photon flux is increased as well. This goes for both detectors since reflections from the copper wall contribute to both photon counts and in each case give rise to the photon flux according to the size of the detection area. For coefficients larger than zero, a photon reaching the wall is not necessarily stopped and absorbed but reflected according to the value the reflectivity was set to. So, not only photons emitted directly towards the detectors are counted but also reflected photons. The contribution to the signal due to reflections outweighs direct irradiation when the reflectivity exceeds 60 %. Also, for each of the reflectivities the PMT counts more photons than the SiPM which is again due to the asymmetric

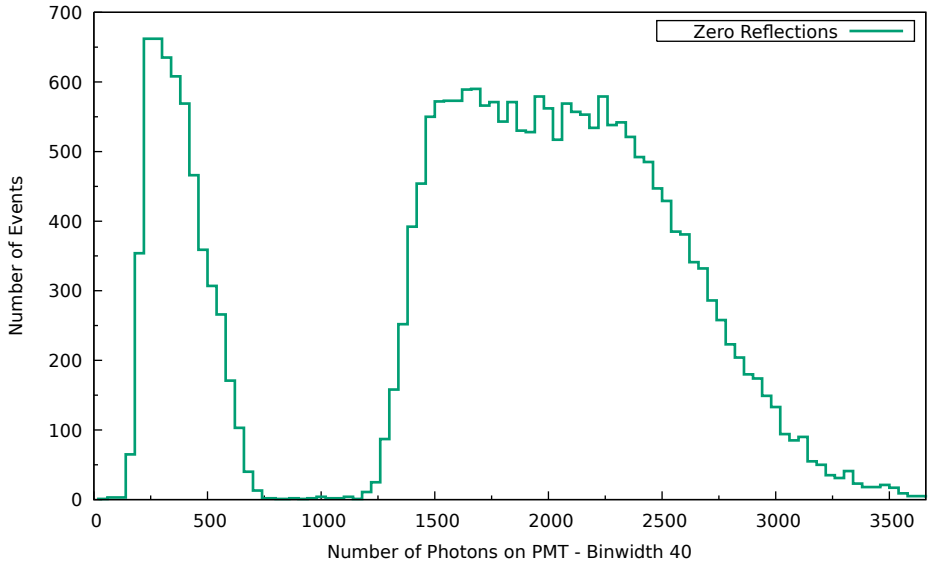

Figure 5.1.: Example of a histogram of counted photons on the PMT for 25000 events in xenon gas: The copper wall and aluminum surface both have a reflectivity of zero. The characteristic shape of the histogram corresponds to the specific design of the set-up and the fact that the alpha source emitted three different energies. Compare sections 4.4 and 3.2

geometry. Furthermore, the photon flux does not seem to increase proportionally to the reflectivity. One also obtains a broadened distribution leading to smeared-out peaks in the histogram.
The result above shows that the surface properties of the inner vessel have massive influence on the total number of photons impinging on the sensitive areas and, therefore, on the photon flux of each of the detectors. Without simulations, the impact of reflections is unpredictable since not only copper reflects photons but aluminum as well. An important issue is to find out how changing the reflection behaviour impacts the ratio of the photon fluxes R on the sensitive areas which according to section 3.3 is equal to the desired correction factor. The procedure of its determination is outlined on the next section.

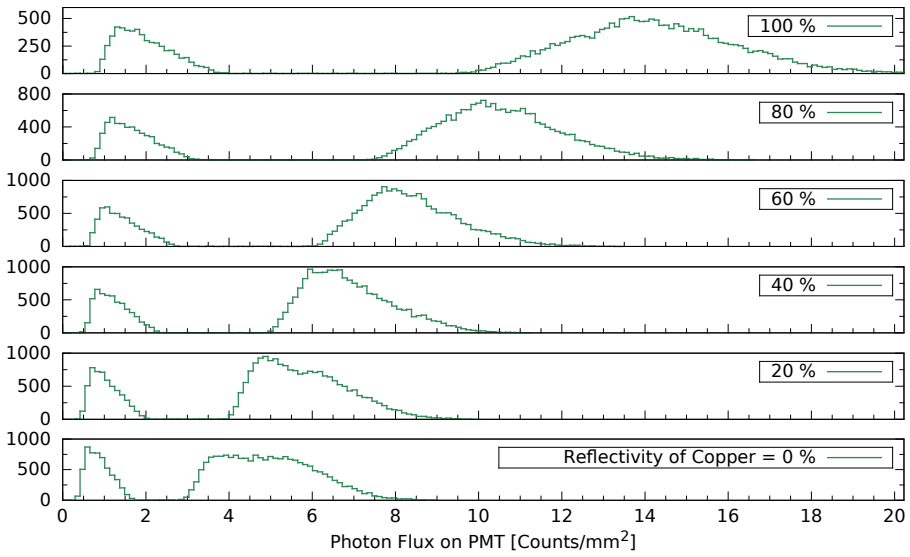

Figure 5.2.: Histogram of the PMT photon flux for different reflectivities of the copper wall. The photon flux rises with increasing reflections, but not proportionally.

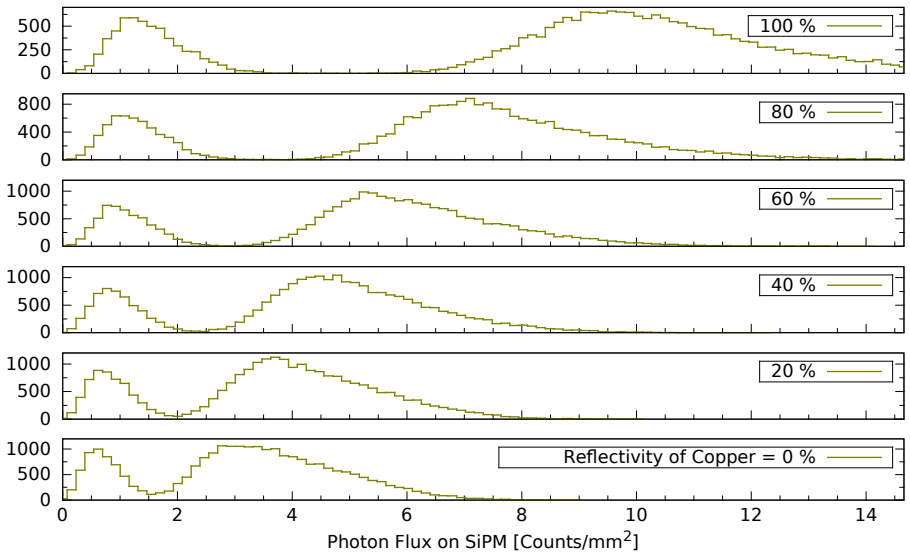

Figure 5.3.: Histogram of the SiPM photon flux depending on the reflectivity of the copper wall. Increasing reflections yield increasing flux.

5.3. Determination of the Correction Factor

For a complete surface investigation not only the reflections from the copper wall need to be taken into account but from the aluminum part as well. Its influence can not be neglected for the analysis for there are over $8\,\mathrm{cm}^2$ aluminum surface contributing to the inner cell's surface. Therefore, both reflectivities were ramped in steps of 10 % between 0 and 100 % and a simulation of 25000 events was performed for all these 121 parameter combinations. For each alpha event a certain number of photons is counted by the SiPM and the PMT and the flux ratio is calculated. Figure 5.4 shows an example of the simulated SiPM-to-PMT flux ratios $\frac{F_{SiPM}}{F_{PMT}}$ for one combination of coefficients, namely a copper reflectivity of 40% and an aluminum reflectivity of 60 %. The data is presented as a histogram using a bin width of 0.01. On the y-axis the fraction of events contributing to each of the bins is plotted. The asymmetric set-up manifests in the mean value of the distribution which is 0.778 ± 0.001, in accordance to the larger average photon flux expected for the PMT compared to the SiPM. The standard deviation of the distribution of about 0.191 is quite large but can be explained by the alpha particle emitting photons in random directions all along its trajectory and the source expansion as already mentioned earlier at the beginning of chapter 5. The different alpha energies causing different amounts of photons produced within each event also contribute to a broadening of the distribution, too. The anti-correlation of the PMT and SiPM signal can be observed in the right of figure 5.4 in the right pile up of events. This observation phenomenon can be reread to its full extend in section 4.4. However, it is worth mentioning that the anti-correlation seems to get washed out with higher reflectivity.
The mean value of all photon flux ratios of one run is equal to the requested factor R for each specific combination of parameters $(i,\, j)$, where $i, j \in \{0\,\%,\ 10\,\%\ldots,\ 100\,\%\}$ denoting the reflectivity of copper and aluminum respectively. For one specific configuration the equation for the correction factor yields

$$R_{ij} = \frac{1}{N}\sum_{k=1}^{N}\left(\frac{F_{\mathrm{SiPM}}}{F_{\mathrm{PMT}}}\right)_k\Bigg|_{\substack{i=\text{Cu-Refl.}\\ \text{j}=\text{Al-Refl.}}} \tag{5.2}$$

This factor was calculated for all configurations to investigate the behaviour of the correction factor, depending on the combination of reflectivities. The result can be seen in figure 5.5 where the coefficients are plotted on the x- and y-axis respectively and the z-axis shows the correction factor R. For clarification and improved visualization the R-values are projected onto the x-y-plain as a colour map. R varies only within a relatively small range between a minimum of 0.747 ± 0.001 and 0.831 ± 0.002 as maximum value. An important remark is that the standard deviation of R_{ij} decreases with increasing reflections. While having a deviation of 0.378 for zero reflectivity, this value drops to a minimum of 0.087 for 100 % reflection on both surfaces. This behaviour can be explained as follows: The effect of the alpha trajectory causing an anti-correlation in the signal stays intact for small reflectivities, however, gets more and more reduced with increasing reflections. This is due to the fact that even if the alpha was emit-

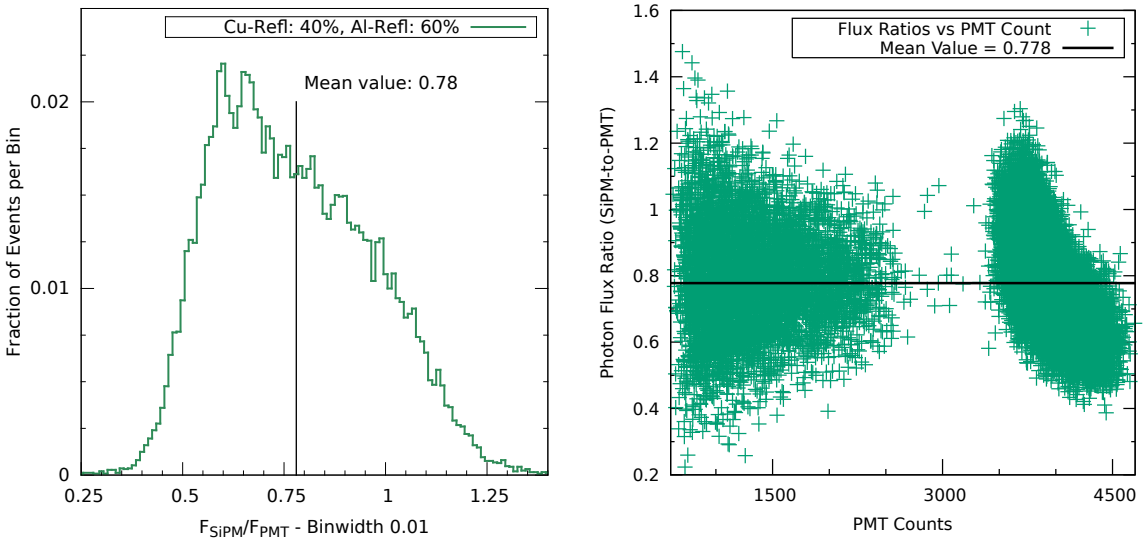

Figure 5.4.: Left: Sample histogram of the photon flux ratio SiPM-to-PMT with reflectivities of 40 % for copper and 60 % for aluminum. 25000 alpha events are used. Asymmetric geometry, alpha trajectory and the extended source cause the mean value to be unequal to one. On the right-hand side: The corresponding scatter plot showing the photon flux ratio of each event depending on the PMT photon count. The anti-correlation of the SiPM-to-PMT signal can be seen in the right accumulation.

ted straight towards one detector reflected photons from the wall contribute to the signal of the other detector and vice versa. These contributions grow with increasing reflectivity. The anti-correlation gets smeared out and the standard deviation decreases.

As a first impression one finds that the reflectivity does not seem to have large influence on the *mean value* of the photon flux ratio. To analyse this presumption quantitatively one has to calculate the mean value for all 121 combinations:

$$R = \frac{1}{(i \cdot j)} \sum_{i=0\,\%}^{100\,\%} \left(\sum_{j=0\,\%}^{100\,\%} R_{ij} \right) \tag{5.3}$$

and calculate the scattering of the R-values around its mean. The overall correction factor R is the *mean value of the photon flux ratios* of all 121 combinations of surface parameters. It has a dispersion around the mean value of only 3.22 %. The calculated mean value is

$$R = 0.776 \ \pm \ 0.002 \qquad \sigma = 0.025 \tag{5.4}$$

Although the deviation of R is very small, one can still optimize the result by excluding unreasonable reflectivities. With some certainty one can say that neither the copper wall nor the aluminum holder of the alpha source have reflectivites close to 0 % or

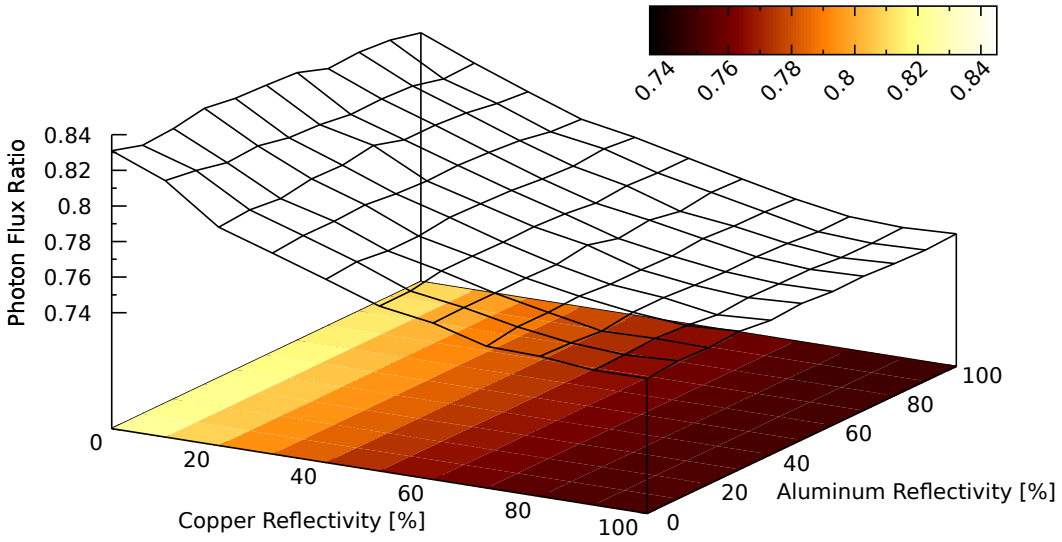

Figure 5.5.: Three-dimensional colour map showing the photon flux ratio depending on the combination of reflectivity for the copper wall and the aluminum holder.

100 %. Furthermore, it was assumed that the reflections from aluminum are in general higher than the ones from copper. Thus, a region of relevant parameter configurations was defined by shrinking the relevant range of coefficients to [10 %, 90 %] for copper and to [20 %, 90 %] for aluminum. Thus, only 72 possible combinations of reflectivities are taken into account. This improves the above result from (5.4) to a new correction factor R_r with a deviation of only 2.59 %:

$$R_r = 0.773 \ \pm 0.002 \qquad \sigma_r = 0.020 \tag{5.5}$$

The small r in the index denotes that this recalculated value relates to the $r$elevant region in the parameter space unlike the value from above which includes all 121 combinations. Figure 5.6 shows the colour map seen in figure 5.5 in two dimensions and highlights the relevant parameter space.

Future plans of the Erlangen nEXO group envisage an upgrade to the set-up enabling xenon liquefaction. A simulation of LXe was performed as well within the scope of this work yielding the following results for the correction factor:

$$R^{\mathrm{LXe}} = 0.782 \ \pm 0.002 \qquad \sigma = 0.017 \tag{5.6}$$

$$R_r^{\mathrm{LXe}} = 0.825 \ \pm 0.002 \qquad \sigma_r = 0.014 \tag{5.7}$$

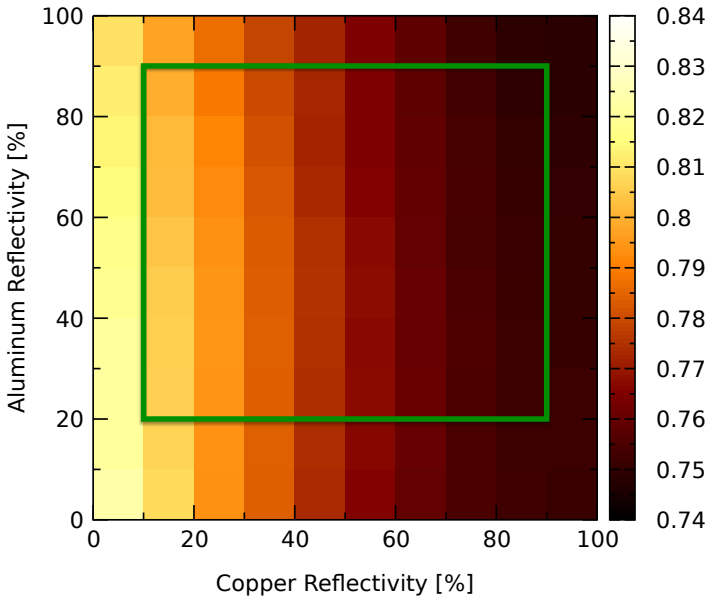

Figure 5.6.: Colour-map of the simulated photon flux ratio. Highlighted in green: The combinations of relevant reflection parameters.

In the following section the correction factor is used for the determination of the photon detection efficiency of a silicon photo multiplier in GXe. A test for the applicability of R to this process is performed and the reliability of results is tested.

5.4. Performing a PDE Determination

In section 3.3, the principle of a PDE determination was outlined which shall be performed in the following using the correction factor R obtained in the previous section. R provides a correction to the assumption that the photon fluxes on both detectors are equal. Only if this factor has been calculated the fluxes can be compared and a PDE can be determined. For the following steps the improved correction factor R_r from equation (5.5) including only relevant combinations of reflections will be used. The set-up and the measurement principle explained in chapter 3 require that the reference PMT has a well-known photon counting efficiency. Recalling section 3.3 the measured flux and the PDE are linked to the actual photon flux Φ on the sensitive area as follows:

$$M = PDE \cdot \Phi$$

After measuring the photon fluxes M_{SiPM} and M_{PMT} respectively the photon detection efficiency of the SiPM can then be calculated by

$$PDE_{\mathrm{SiPM}} = \frac{M_{\mathrm{SiPM}}}{M_{\mathrm{PMT}}} \cdot PDE_{\mathrm{PMT}} \cdot \frac{1}{R} \tag{5.8}$$

This equation has been motivated in section 3.3. In the following *simulated data* is used to check if a given PDE of the SiPM can be reproduced using the optimized correction factor R_r. To this end, another 25000 events were simulated in gaseous xenon. The goal is to gather realistic data by simulating a measurement which will then be analysed using R_r. As combination of reflectivities for this "simulated measurement", a tuple close to the boundary of the relevant parameter space was chosen: A copper reflectivity of 10 % and an aluminum reflectivity of 30 %. This is a rather extreme combination close to the boundary of the relevant range. A successful test of this combination is a promising prerequisite for the reliable production of good results for other parameters as well. For the simulation of the detector response, a PDE was implemented for the SiPM and a photon counting efficiency $\varepsilon_{\mathrm{PMT}}$ for the PMT respectively. Only 32,1 % of all photons impinging on the PMT were counted according to the quantum efficiency (QE) of this device[1]. The SiPM was equipped with a detection efficiency of 10 % using the same method. The goal was to take the simulated "measurement data", apply the process of PDE determination to them using R_r from section 5.3 and find out if the efficiency can be reproduced. The simulated events can be seen in figure 5.4 where the counts on each detector are plotted. The line structure of the SiPM counts originates in the discreetness of photons. This actually applies for the PMT as well, but its number of counts is too high to make it visible in this plot.

[1]The collection efficiency ε_D of the dynodes was not considered for this simulation and can be assumed to be 100 %. For details on QE, ε_D and the detection efficiency of PMTs see section 3.2.2

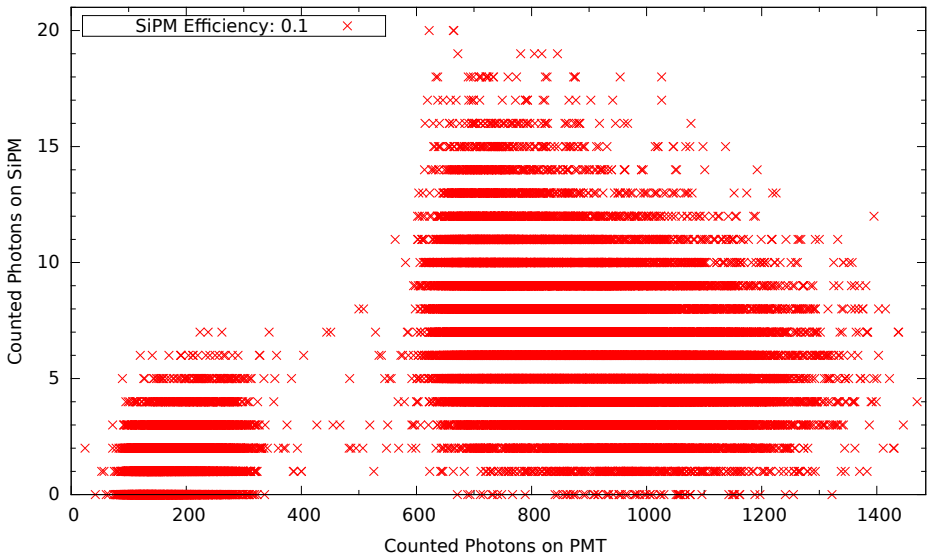

Figure 5.7.: Simulated measurement of a SiPM with a PDE of 10 % and a reference PMT with a photon collection efficiency of 32.1 %. The fact that photons can only be counted in whole-numbered multiples causes the line structure.

The mean value of the photon flux ratio from all simulated events was calculated:

$$\frac{M_{\mathrm{SiPM}}}{M_{\mathrm{PMT}}} = 0.253 \ \pm 0.010 \tag{5.9}$$

Together with a difference in the size of the detector surfaces of about a factor of 34.4 (compare details on the set-up in 3.2.2 and 4.2.2) this means that on average about 128.2 times more photons were measured by the PMT than by the SiPM. The calculated flux ratio in (5.9) is about a factor of 3 smaller than the value from (5.5). To quantify the SiPM's efficiency this result is then plugged in equation 5.8, with $R_r = 0.773 \ \pm 0.002$, which yields

$$PDE_{\mathrm{SiPM}} = 10.511\,\% \ \pm 0.042\,\%$$

The PDE that was set before which was used to produce a "simulated measurement" could be reproduced with only little deviation. The obtained value for the efficiency of the SiPM was just 5.11 % higher than the set value of 10 %.

There is, however, a huge improvement to the PDE determination if the surface properties were well-known. In this case the correction factor simulated for the combination chosen above (10 %, 30 %) could be used. In the course of the analysis in 5.3 a value of 0.814 could be determined for this parameter tuple. Using this as R one obtains much better results:

$$PDE_{\mathrm{SiPM}} = \frac{M_{\mathrm{SiPM}}}{M_{\mathrm{PMT}}} \cdot PDE_{\mathrm{PMT}} \cdot \frac{1}{R_{(10\,\%,\ 30\,\%)}} = 9.982\,\% \pm 0.040\,\%$$

This improved PDE shows a the deviation of only 0.18 % from the set value. Unfortunately, without having more details on the surface structures and the reflectivities this result can not be achieved in the real experiment. Applying the correction factor of a specific parameter configuration to the simulated data is of course mainly a test of the self-consistency of the simulation: This procedure reproduces a result originating from the exact same parameters used to determine the correction factor of that very configuration. Although no real measurement data for further tests are available that reliably have the same parameters this method remains at least a promising one.

There is, yet, another option that could possibly improve the result of the PDE calculation. One can see in figure 5.8 that the photon flux ratio has a large dispersion around the mean value following a specific topology. The flux ratio changes depending on the PMT photon count. Especially for those events in the right cluster following the anti-correlated relationship of the distribution there is a significant deviation from the mean value. The idea is to use this behaviour of the event distribution to calculate the correction factor depending on the PMT count. That means that the x-axis (PMT photon counts) is divided into bins with a fixed width – here 100. Then, the correction factor is calculated for each of the bins separately using the data from the run with parameter combination (10 %, 30 %). This is done by allocating the events to the bins corresponding to the number of photons arriving at the sensitive PMT area. Afterwards, the photon flux ratio for each bin is calculated. The mean value of all the ratios in one bin gives the mean correction factor of that bin according to equation 5.1. The result is a correction factor for the parameter combination (10 %, 30 %) depending on the PMT photon count.

The expectation is to make the PDE determination more precise when the fluctuating photon flux ratios are compensated with a correction factor that depends on the PMT photon count. It was assumed that any measured data has the same topology than the simulation which is quite likely since the physical validity of this simulation program was demonstrated in 4.4. The events of the measurement are divided into the same number of bins and the PDE is then calculated for each bin separately.

Unfortunately, it turns out that this method can not meet the expectations. While the PDE of the SiPM can be reproduced, it is not quite as precise as with the first method and by far not as good as with the correction factor for one specific parameter configuration. For the PDE of the SiPM one obtains:

$$PDE_{\mathrm{SiPM}} = \frac{1}{\text{Num of bins}} \sum_{i}^{\substack{\text{Number}\\ \text{of bins}}} (PDE)'_i = 10.600\,\% \pm 0.001(3)\,\%$$

Discussion of the methods

The result of the third method was no improvement which was mainly for one reason: It basically just calculates a PDE that is PMT-count dependent. One can conclude

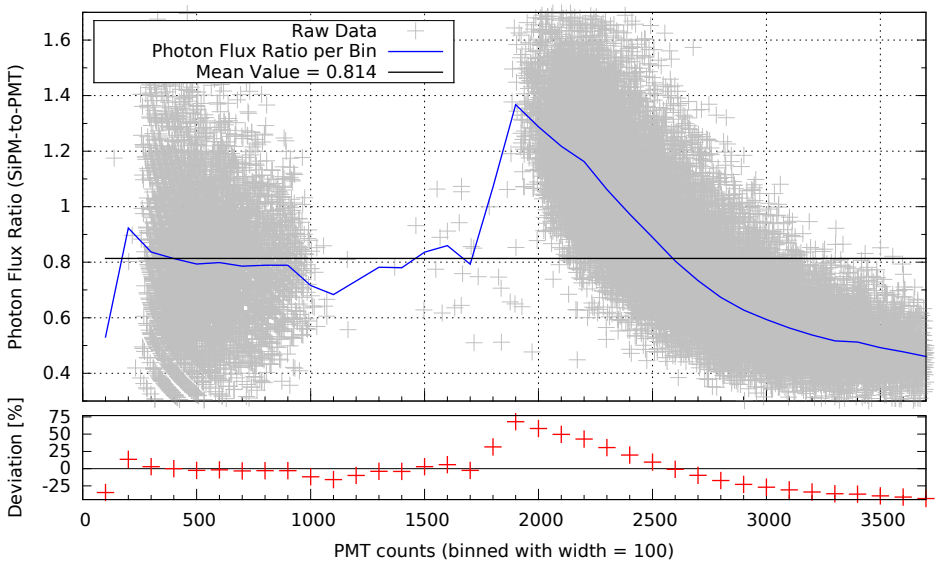

Figure 5.8.: Mean values of the photon flux ratio for the reflectivity combination (10 %, 30 %) as a function of PMT photon count. The ratio shows vast fluctuations around the mean value. The lower graph shows this deviation in percent.

that it can indeed calculate the PDE more precisely, but just for one bin covering only a specific range of PMT counts. However, the PDEs of the bins still show large fluctuations. Therefore, this method results in a better overall deviation but the mean value does not improve.

Due to the lack of information on the surfaces, the second method is hardly practicable. Furthermore, it could be shown that a more precise determination of the correction factor by introducing a dependence on PMT photon count does not result in a more precise PDE determination the only valid method is to use the overall correction factor calculated in 5.3. This method is able to reproduce a PDE which was set beforehand within acceptable accuracy.

6. Conclusion

6.1. Summary

The present work examined the Erlangen set-up for the characterization of Silicon Photomultipliers (SiPMs) for nEXO using GEANT4 simulations for the production and propagation of alpha particle scintillation light in liquid and gaseous xenon. The main purpose of the set-up is the determination of the photon detection efficiency (PDE) of SiPMs at cryogenic temperatures to investigate their applicability in the nEXO experiment for the search for the neutrinoless double beta decay. An introduction to this hypothetical second order weak interaction and a range of detection methods were given in chapter 2. Using a detailed description of the xenon cell, its design and components it could be shown that a correct and reliable PDE determination is not possible without the help of simulations. Since the measurement method of the set-up includes the comparison of photon fluxes on the SiPM and a reference PMT, possible influences on the flux ratio R were discussed (see chapter 3).

In consideration of well researched physical principles the simulation programme was set up and optimized (details can be found in chapter 4). The physical validity of the simulation was tested and results were compared to cited literature. The simulation is able to reproduce correct particle ranges and photon numbers for the liquid and the gaseous phase. These quantities also show sensible behaviour under variation of particle energy or density of the medium. A precise examination of the geometrical properties of the set-up and the nature of the alpha source enabled a detailed description of the topology of a measurement (Compare chapter 4.4).

The simulation of 25000 alpha events per run was performed for various surface properties in order to investigate the influence of reflections on the photon flux on the detector surfaces as well as on the flux ratio. The analysis of the simulation data yields a rising photon flux with increasing reflectivities. However, the photon flux ratio R is almost independent of the reflectivity of the surfaces of the copper wall and the aluminum holder. Using simulations of 121 parameter configurations of the reflectivities a correction factor for the photon flux could be calculated that enables a PDE determination with the Erlangen set-up. A further improvement of that value was possible by limiting the parameter space to the relevant range.

The results from the simulation were then applied to calculate the PDE of a simulated SiPM which had a fixed detection efficiency of 10 %. Using the deduced correction

factor the PDE that was set beforehand could be reproduced. The result could be improved significantly if more information on the surface properties were available. A correction factor that was calculated depending on the photon count on the PMT, however, could bring no further improvements.

6.2. Discussion and Prospect

In some cases the characterization of different SiPMs requests modifications of the internal design of the xenon cell. Then, size and position of the SiPM can change as well as position and geometry of the amplifier board. Unfortunately, redesigning the internals of the cell requires some changes in the simulation as well. Since the flux ratio depends on the distance of the detectors from the source the simulation needs to be performed again with the new geometric measures. This also applies to variations in density or phase of the xenon. However, the structure of the code allows for an easy modification of the most important values including the SiPM position. In order to gain more flexibility for future applications of the simulation the creation of a three dimensional *light map* for the cell might be promising. The aim of such a map is to provide expectation values for the photon flux on a surface depending on the position of that surface inside the cell. For each voxel in the map the correction factor R could easily be calculated and applied to the PDE determination. Since building such a map is a computationally expensive undertake only a certain parameter range could be considered. This includes the number of accepted combinations of reflectivities as well as the spatial resolution of the light map (i.e. the number of positions in the cell for which the photon number should be calculated).

A further reduction of the considered combinations of reflectivities would result in an improved calculation of R. One way to gain information on surface properties is to measure the reflection behaviour in a special test stand. However, one would need a sample of the material that had received the same surface treatment as the actual materials in the cell. Furthermore, the test stand would have to provide the same conditions as present in the cell. Another possible way of getting information on the surface properties might be the investigation of other, so far unused, surface-dependent quantities. A more accurate analysis of the general topology of the distribution of measurement points would be one example (for details on the topology see section 4.4). Or the ratio of the peak positions in the histogram (i.e. the mean value of the photon count contributing to that peak). As seen in figure 6.1 the left-to-right-peak ratio of the simulation is not constant and shows a significant minimum for low aluminum and high copper reflectivity. A comparison of this quantity with real measurement data might provide further information on the surface conditions in the set-up.

In chapter 5.4 the PDE determination based on a correction factor depending on PMT photon counts was discussed. It could be shown that this method does not provide an improvement towards other procedures. However, another possibility might consist in

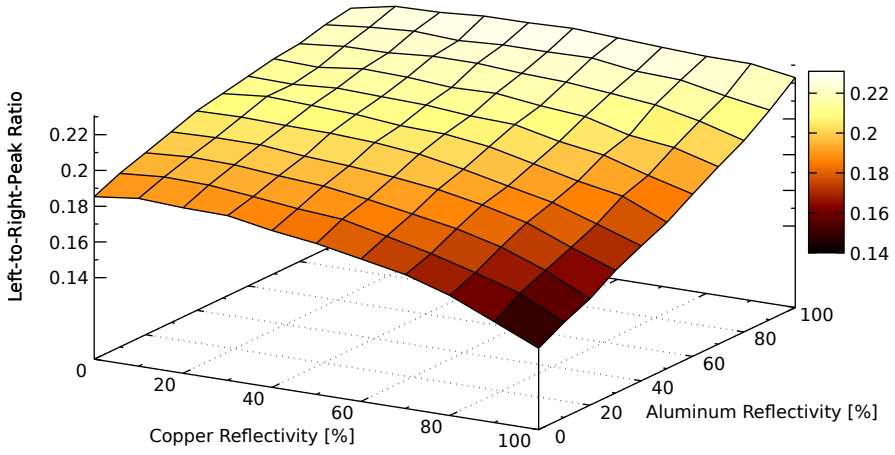

Figure 6.1.: Ratio of the peak positions of the PMT photon count histogram from the simulation depending on the reflectivities. A comparison of this quantity with measurement data could provide information on the surface structure inside the chamber and therefore improve the calculation of the correction factor.

calculating the correction factor for each of the accumulations separately and then apply that result to the PDE determination.

For the PMT used in the Erlangen set-up a quantum efficiency of 32.1 % was reported by the manufacturer [Ham], which is closely related to the photon counting efficiency. However, this quantity might only be applicable for perpendicular incidence of light and potentially decreases for flat angles. Since the entrance window of the PMT is made of quartz glass reflection and refraction occurs at the border between xenon and glass. The contribution of flat angles to the total number of photons on the detectors might change with the reflection behaviour of the copper wall and the aluminum holder. Thus, better knowledge of the angular dependence of the detector response is desirable. However, at the current stage of the simulation programme an angular-dependent treatment of photon detection is not implemented and might constitute an important part of future work on this topic. Maybe a close cooperation with SiPM and PMT manufacturers to determine the angular dependence of the detection efficiency is advisable as well.

One big issue in the experiment is the unknown xenon purity which limits the absorption length λ_{abs} of scintillation light. For the simulation λ_{abs} was set to a very high value of 2000 cm representing ideal, ultra pure xenon conditions. By using different values for λ_{abs} in the simulation the impact of impurities on the measurement could be estimated. Also, the density plays a role in the experiment since it influences the total number of produced scintillation photons. In section 4.4 it could be shown that the

anti-correlation of the SiPM and PMT light signal diminishes with increasing density. This might also improve the accuracy of the calculation of the correction factor R.

Despite a series of still existing uncertainties and unknown influences the simulation in its present form constitutes the foundation of a good understanding of the Erlangen set-up. Other researchers might use and extend the existing programme and its capabilities for new applications and investigations. This provides the possibility for promising contributions to the characterization of silicon photomultipliers for their use in the nEXO experiment for the search for the neutrinoless double beta decay.

A. Addendum

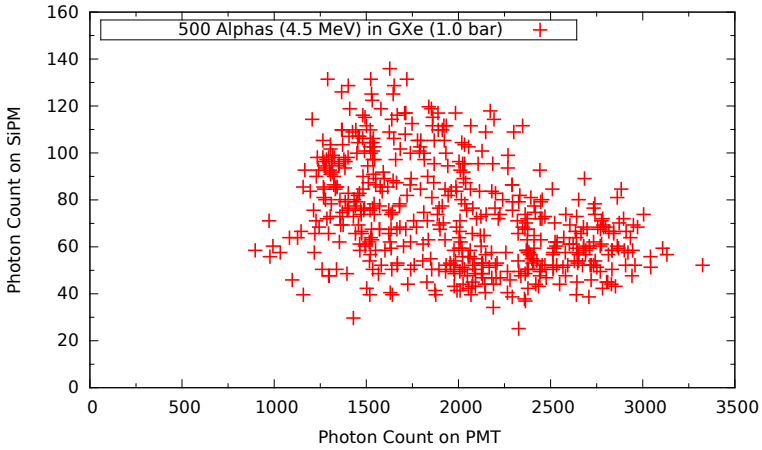

Figure A.1.: Scatterplot of the SiPM-vs-PMT photon count for a test run *without* the aluminum holder. The left cluster at small photon numbers has vanished.

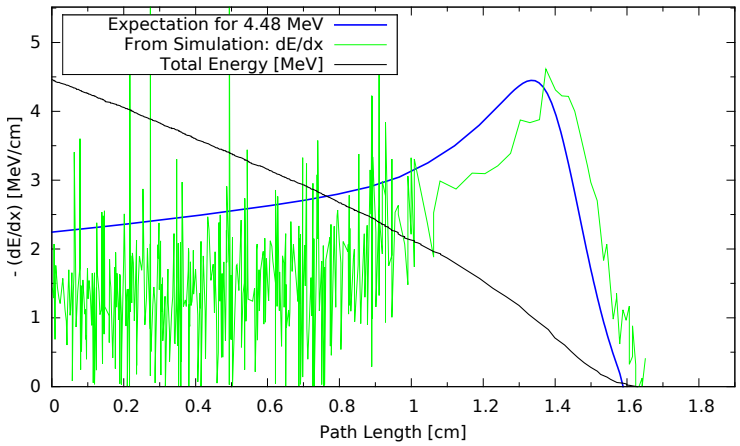

Figure A.2.: Expected and simulated stopping power versus path length. The expected total range can be reproduced. The strong fluctuation (green curve) originates in the step size chosen by GEANT4.

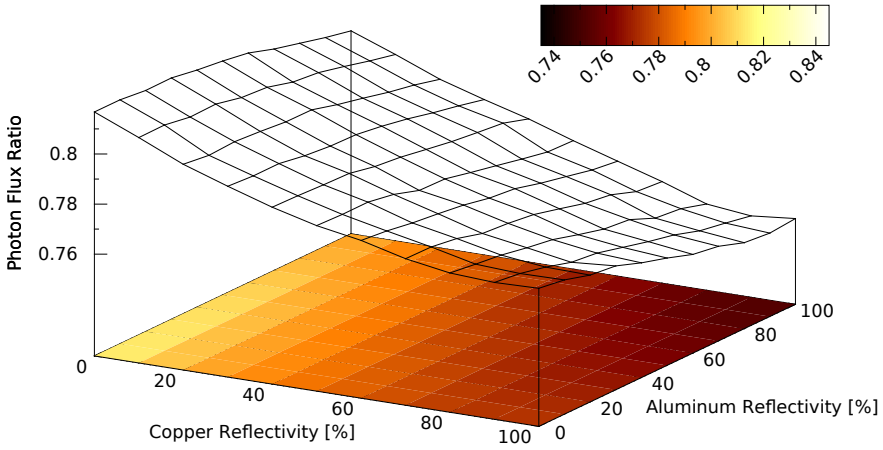

Figure A.3.: Three-dimensional colour map in LXe: Photon flux ratio depending on the reflectivity of the copper and the aluminum surface. Mean value for all 121 parameter combinations: $R = 0.782 \pm 0.002$; $\sigma = 0.017$

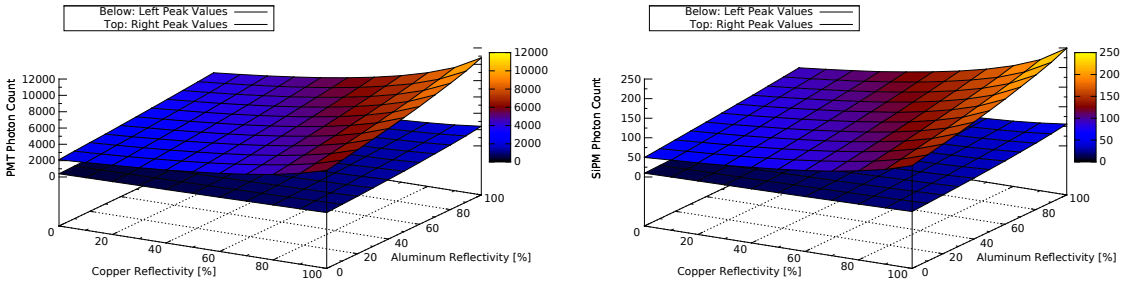

Figure A.4.: Peak positions of the PMT (left) and the SiPM photon count depending on the reflectivities of the copper and the aluminum surface. Also compare the peak ratio for PMT in figure 6.1.

Density [g/cm^3]	**Expected Range** [cm]	**Simulation** [cm]	**abs. dev.** [cm]	**rel. dev.** %
0.8	2.185	2.313	0.128	5.9
1.0	1.748	-	-	-
1.1	1.588	1.681	0.093	5.9
1.5	1.165	1.234	0.069	5.9
1.8	0.971	1.029	0.058	6.0
2.5	0.699	0.743	0.044	6.3
4.0	0.437	0.466	0.029	6.6
8.0	0.219	0.236	0.017	7.8
12.0	0.146	0.160	0.014	9.6

Table A.1.: Ranges of alpha particles with 4.48 MeV in GXe depending on the density. Simulated results are compared to expectation values (from [Ber+05a]) and the absolute and relative deviation are given. The values are also shown in figure 4.13.

B. List of Abbreviations

$0\nu\beta\beta$	Neutrinoless double beta decay
$2\nu\beta\beta$	Neutrino accompanied double beta decay
APD	Avalanche Photodiode
BG	Background
CAD	Computer-aided design
C.L.	Confidence Level
CP	Charge-parity (as in CP violation)
GXe	Gaseous Xenon
LXe	Liquid Xenon
MARCI	Measurement Analysis and Run Control Interface
NME	Nuclear Matrix Element
PDE	Photon Detection Efficiency
PMT	Photomultiplier Tube
ppm	Parts per million
QE	Quantum efficiency
ROI	Region of interest
SiPM	Silicon Photomultiplier
TPC	Time projection chamber
VUV	Vacuum Ultra-Violet

C. List of Figures

D. List of Tables

References

[Aal+02] C. E. Aalseth et al. "Comment on *Evidence for Neutrinoless Doublebeta Decay*". In: *Modern Physics Letters A* 17.22 (2002), pp. 1475–1478. DOI: 10.1142/S0217732302007715. URL: http://www.worldscientific.com/doi/abs/10.1142/S0217732302007715.

[Ago+03] S. Agostinelli et al. "Geant4 — a simulation toolkit". In: *Nuclear Instruments and Methods in Physics Research Section A: Accelerators, Spectrometers, Detectors and Associated Equipment* 506.3 (2003), pp. 250 –303. ISSN: 0168-9002. DOI: http://dx.doi.org/10.1016/S0168-9002(03)01368-8. URL: http://www.sciencedirect.com/science/article/pii/S0168900203013688.

[Ago+16] M. Agostini et al. "Search of Neutrinoless Double Beta Decay with the {GERDA} Experiment". In: *Nuclear and Particle Physics Proceedings* 273–275 (2016). 37th International Conference on High Energy Physics (ICHEP), pp. 1876 –1882. ISSN: 2405-6014. DOI: http://dx.doi.org/10.1016/j.nuclphysbps.2015.09.303. URL: http://www.sciencedirect.com/science/article/pii/S2405601415007920.

[AD10] E. Aprile and T. Doke. "Liquid Xenon Detectors for Particle Physics and Astrophysics". In: *Rev. Mod. Phys.* 82 (2010), pp. 2053–2097. DOI: 10.1103/RevModPhys.82.2053. arXiv: 0910.4956 [physics.ins-det].

[Apr+12] E Aprile et al. "Measurement of the quantum efficiency of Hamamatsu R8520 photomultipliers at liquid xenon temperature". In: *Journal of Instrumentation* 7.10 (2012), P10005. URL: http://stacks.iop.org/1748-0221/7/i=10/a=P10005.

[Apr+07] Elena Aprile et al. *Noble Gas Detectors*. Weinheim: John Wiley & Sons, 2007.

[Aug+12a] M. Auger et al. "Search for Neutrinoless Double-Beta Decay in ^{136}Xe with EXO-200". In: *Phys. Rev. Lett.* 109 (3 2012), p. 032505. DOI: 10.1103/PhysRevLett.109.032505. URL: http://link.aps.org/doi/10.1103/PhysRevLett.109.032505.

[Aug+12b] M. Auger et al. "The EXO-200 detector, part I: Detector design and construction". In: *JINST* 7 (2012), P05010. DOI: 10.1088/1748-0221/7/05/P05010.

[Aul+02] Brian F Aull et al. “Geiger-mode avalanche photodiodes for three-dimensional imaging”. In: *Lincoln Laboratory Journal* 13.2 (2002), pp. 335–349.

[Bal+05] A. Baldini et al. “Absorption of scintillation light in a 100 l liquid xenon -ray detector and expected detector performance”. In: *Nuclear Instruments and Methods in Physics Research Section A: Accelerators, Spectrometers, Detectors and Associated Equipment* 545.3 (2005), pp. 753 –764. ISSN: 0168-9002. DOI: http://dx.doi.org/10.1016/j.nima.2005.02.029. URL: http://www.sciencedirect.com/science/article/pii/S0168900205008259.

[Ber+05a] M.J. Berger et al. *ESTAR, PSTAR, and ASTAR: Computer Programs for Calculating Stopping-Power and Range Tables for Electrons, Protons, and Helium Ions (version 1.2.3)*. National Institute of Standards and Technology. [online; accessed August 12, 2016]. Gaithersburg, MD, 2005. URL: http://physics.nist.gov/PhysRefData/Star/Text/ASTAR.html.

[Ber+05b] Paolo Bernardini et al. “NOW 2004 The GERmanium Detector Array (Gerda) for the search of neutrinoless double beta decays of 76Ge at LNGS”. In: *Nuclear Physics B - Proceedings Supplements* 145 (2005), pp. 242 –245. ISSN: 0920-5632. DOI: http://dx.doi.org/10.1016/j.nuclphysbps.2005.04.014. URL: http://www.sciencedirect.com/science/article/pii/S0920563205005116.

[BR99] Aleksey Bolotnikov and Brian Ramsey. “Studies of light and charge produced by alpha-particles in high-pressure xenon”. In: *Nuclear Instruments and Methods in Physics Research Section A: Accelerators, Spectrometers, Detectors and Associated Equipment* 428.2–3 (1999), pp. 391 –402. ISSN: 0168-9002. DOI: http://dx.doi.org/10.1016/S0168-9002(99)00173-4. URL: http://www.sciencedirect.com/science/article/pii/S0168900299001734.

[BR97] Aleksey Bolotnikov and Brian Ramsey. “The spectroscopic properties of high-pressure xenon”. In: *Nuclear Instruments and Methods in Physics Research Section A: Accelerators, Spectrometers, Detectors and Associated Equipment* 396.3 (1997), pp. 360 –370. ISSN: 0168-9002. DOI: http://dx.doi.org/10.1016/S0168-9002(97)00784-5. URL: http://www.sciencedirect.com/science/article/pii/S0168900297007845.

[CA13] V. Chepel and H. Araujo. “Liquid noble gas detectors for low energy particle physics”. In: *JINST* 8 (2013), R04001. DOI: 10.1088/1748-0221/8/04/R04001. arXiv: 1207.2292 [physics.ins-det].

[Chu01] D.D.L Chung. “Materials for thermal conduction”. In: *Applied Thermal Engineering* 21.16 (2001), pp. 1593 –1605. ISSN: 1359-4311. DOI: http://dx.doi.org/10.1016/S1359-4311(01)00042-4. URL: http://www.sciencedirect.com/science/article/pii/S1359431101000424.

[Col] Geant4 Collaboration. *Geant4 User's Guide for Application Developers*. [online; accessed August 07, 2016]. URL: http://geant4.web.cern.ch/geant4/UserDocumentation/UsersGuides/ForApplicationDeveloper/html/index.html.

[Col14a] Geant4 Collaboration. *Physics Reference Manual*. Version 10.1. [online; accessed August 10, 2016]. 2014. URL: http://geant4.web.cern.ch/geant4/UserDocumentation/UsersGuides/PhysicsReferenceManual/fo/PhysicsReferenceManual.pdf.

[Col14b] Planck Collaboration. "Planck 2013 results. I. Overview of products and scientific results". In: *Astronomy & Astrophysics* 571 (2014).

[Col16] The nEXO Collaboration. *Official Plots*. 2016.

[Col14c] The EXO-200 Collaboration. "Search for Majorana neutrinos with the first two years of EXO-200 data". In: *Nature* (2014). DOI: 10.1038/nature13432. URL: http://dx.doi.org/10.1038/nature13432.

[Dat] GESTIS Substance Databank. *Xenon*. [Data Sheet, online; accessed August 06, 2016]. Institute for Occupational Safety and Health of the German Social Accident Insurance. URL: http://gestis-en.itrust.de/nxt/gateway.dll/gestis_en/007540.xml?f=templates$fn=default.htm$3.0.

[Din13] N. Dinu. "Instrumentation on silicon detectors: from properties characterization to applications". Accreditation to supervise research. Université Paris Sud - Paris XI, Oct. 2013. URL: https://tel.archives-ouvertes.fr/tel-00872318.

[Dok+02] Tadayoshi Doke et al. "Absolute Scintillation Yields in Liquid Argon and Xenon for Various Particles". In: *Japanese Journal of Applied Physics* 41.3R (2002), p. 1538. URL: http://stacks.iop.org/1347-4065/41/i=3R/a=1538.

[Eck+10] Patrick Eckert et al. "Characterisation studies of silicon photomultipliers". In: *Nuclear Instruments and Methods in Physics Research Section A: Accelerators, Spectrometers, Detectors and Associated Equipment* 620.2–3 (2010), pp. 217 –226. ISSN: 0168-9002. DOI: http://dx.doi.org/10.1016/j.nima.2010.03.169. URL: http://www.sciencedirect.com/science/article/pii/S0168900210008156.

[Era+07] P. Eraerds et al. "SiPM for fast Photon-Counting and Multiphoton Detection". In: *Opt. Express* 15.22 (2007), pp. 14539–14549. DOI: 10.1364/OE.15.014539. URL: http://www.opticsexpress.org/abstract.cfm?URI=oe-15-22-14539.

[Fur39] W. H. Furry. "On Transition Probabilities in Double Beta-Disintegration". In: *Phys. Rev.* 56 (12 1939), pp. 1184–1193. DOI: 10.1103/PhysRev.56.1184. URL: http://link.aps.org/doi/10.1103/PhysRev.56.1184.

[Gan+12] A. Gando et al. “Measurement of the double beta decay half-life of ^{136}Xe with the KamLAND-Zen experiment”. In: *Phys. Rev. C* 85 (4 2012), p. 045504. DOI: 10.1103/PhysRevC.85.045504. URL: http://link.aps.org/doi/10.1103/PhysRevC.85.045504.

[Gan+16] A. Gando et al. “Search for Majorana Neutrinos Near the Inverted Mass Hierarchy Region with KamLAND-Zen”. In: *Phys. Rev. Lett.* 117 (8 2016), p. 082503. DOI: 10.1103/PhysRevLett.117.082503. URL: http://link.aps.org/doi/10.1103/PhysRevLett.117.082503.

[GM35] M. Goeppert-Mayer. “Double Beta-Disintegration”. In: *Phys. Rev.* 48 (6 1935), pp. 512–516. DOI: 10.1103/PhysRev.48.512. URL: http://link.aps.org/doi/10.1103/PhysRev.48.512.

[GC+12] J. J. Gomez-Cadenas et al. “The Search for neutrinoless double beta decay”. In: *Riv. Nuovo Cim.* 35 (2012), pp. 29–98. DOI: 10.1393/ncr/i2012-10074-9. arXiv: 1109.5515 [hep-ex].

[Gri08] D. Griffiths. *Introduction to Elementary Particles*. Physics textbook. Wiley, 2008. ISBN: 9783527406012. URL: https://books.google.de/books?id=w9Dz56myXm8C.

[GC+11] J.J. Gómez-Cadenas et al. “Sense and sensitivity of double beta decay experiments”. In: *Journal of Cosmology and Astroparticle Physics* 2011.06 (2011), p. 007. URL: http://stacks.iop.org/1475-7516/2011/i=06/a=007.

[Ham] Hamamatsu Photonics K.K. [Data Sheet, online; accessed August 05, 2016]. URL: https://www.hamamatsu.com/us/en/product/category/3100/3001/R8520-406/index.html.

[Hec98] Eugene Hecht. *Hecht Optics Third Edition*. Adelphi University, United States: Addison Weswley Longman, Inc., 1998.

[Hit+05] Akira Hitachi et al. “New approach to the calculation of the refractive index of liquid and solid xenon”. In: *The Journal of Chemical Physics* 123.23, 234508 (2005). DOI: http://dx.doi.org/10.1063/1.2136879. URL: http://scitation.aip.org/content/aip/journal/jcp/123/23/10.1063/1.2136879.

[Jor+65] Joshua Jortner et al. “Localized Excitations in Condensed Ne, Ar, Kr, and Xe”. In: *The Journal of Chemical Physics* 42.12 (1965), pp. 4250–4253. DOI: http://dx.doi.org/10.1063/1.1695927. URL: http://scitation.aip.org/content/aip/journal/jcp/42/12/10.1063/1.1695927.

[Keta] Ketek GmbH. [Online; accessed August 03, 2016]. München. URL: www.ketek.net/products/sipm-technology/microcell-construction/.

[Ketb] Ketek GmbH. [Online; accessed August 02, 2016]. München. URL: www.ketek.net/ketek/ketek-33.jpg.

[Ketc] Ketek GmbH. [Online; accessed August 04, 2016]. URL: http://www.ketek.net/products/sipm/pm3350/.

[K.K07] Hamamatsu Photonics K.K. *Photomultiplier Tubes - Basics and Applications Third Edition*. [online; accessed August 04, 2016]. Electron Tube Division, Editorial Committee, 2007. URL: https://www.hamamatsu.com/resources/pdf/etd/PMT_handbook_v3aE.pdf.

[KK+01] Klapdor-Kleingrothaus et al. "Evidence for Neutrinoless Double Beta Decay". In: *Modern Physics Letters A* 16.37 (2001), pp. 2409–2420. DOI: 10.1142/S0217732301005825. URL: http://www.worldscientific.com/doi/abs/10.1142/S0217732301005825.

[Kob+04] S. Kobayashi et al. "Scintillation luminescence for high-pressure xenon gas". In: *Nuclear Instruments and Methods in Physics Research Section A: Accelerators, Spectrometers, Detectors and Associated Equipment* 531.1–2 (2004). Proceedings of the 5th International Workshop on Radiation Imaging Detectors, pp. 327 –332. ISSN: 0168-9002. DOI: http://dx.doi.org/10.1016/j.nima.2004.06.024. URL: http://www.sciencedirect.com/science/article/pii/S0168900204011891.

[Kod+01] K. Kodama et al. "Observation of tau neutrino interactions". In: *Phys. Lett.* B504 (2001), pp. 218–224. DOI: 10.1016/S0370-2693(01)00307-0.

[LM96] A. Levin and C. Moisan. "A more physical approach to model the surface treatment of scintillation counters and its implementation into DETECT". In: *Nuclear Science Symposium, 1996. Conference Record., 1996 IEEE*. Vol. 2. 1996, 702–706 vol.2. DOI: 10.1109/NSSMIC.1996.591410.

[Lic16] Caio Licciardi. *The Sensitivity of the nEXO Experiment to Majorana Neutrinos*. Neutrino Conference 2016. [online; accessed September 08, 2016], Poster P4.056 On behalf of the EXO-200 and nEXO Collaborations. Imperial College London, July 2016. URL: http://neutrino2016.iopconfs.org/postersession4.

[Mim+09] Mitsuteru Mimura et al. "Average Numbers of Scintillation Photons and Electrons Produced by an Alpha Particle in High-Density Xenon Gas". In: *Japanese Journal of Applied Physics* 48.7R (2009), p. 076501. URL: http://stacks.iop.org/1347-4065/48/i=7R/a=076501.

[Ost+15] I. Ostrovskiy et al. "Characterization of Silicon Photomultipliers for nEXO". In: *IEEE Transactions on Nuclear Science* 62.4 (2015), pp. 1825–1836. ISSN: 0018-9499. DOI: 10.1109/TNS.2015.2453932.

[Phy15] The Official Web Site of the Nobel Prize The Nobel Prize in Physics. [online; accessed September 01, 2016]. 2015. URL: https://www.nobelprize.org/nobel_prizes/physics/.

[QV15] X. Qian and P. Vogel. "Neutrino mass hierarchy". In: *Progress in Particle and Nuclear Physics* 83 (2015), pp. 1 –30. ISSN: 0146-6410. DOI: http://dx.doi.org/10.1016/j.ppnp.2015.05.002. URL: http://www.sciencedirect.com/science/article/pii/S0146641015000307.

[Ret16] C. Rethmeier. "Characterization of VUV sensitive SiPMs for nEXO". In: *Journal of Instrumentation* 11.03 (2016), p. C03002. URL: http://stacks.iop.org/1748-0221/11/i=03/a=C03002.

[Sai+02] K Saito et al. "Absolute number of scintillation photons emitted by alpha particles in rare gases". In: *IEEE Transactions on Nuclear Science* 49.4 (2002), pp. 1674–1680.

[SNM04] M. Saito, T. Nishikawa, and M. Miyajima. "Electric field dependence of luminescence due to alpha particles in gaseous xenon and the energy expended per photon". In: *IEEE Transactions on Nuclear Science* 51.5 (2004), pp. 2125–2130. ISSN: 0018-9499. DOI: 10.1109/TNS.2004.836030.

[Sch97] N. Schmitz. *Neutrinophysik*. Teubner Studienbücher Physik. Vieweg+ Teubner Verlag, 1997. ISBN: 9783519032366. URL: https://books.google.de/books?id=UYDvnQEACAAJ.

[Sla16] Slawomir Piatek. Hamamatsu Corporation & New Jersey Institute of Technology. [Online; accessed August 04, 2016]. Feb. 2016. URL: http://www.hamamatsu.com/jp/en/community/optical_sensors/sipm/what_is_sipm_pde/index.html.

[Sol+04] V.N Solovov et al. "Measurement of the refractive index and attenuation length of liquid xenon for its scintillation light". In: *Nuclear Instruments and Methods in Physics Research Section A: Accelerators, Spectrometers, Detectors and Associated Equipment* 516.2–3 (2004), pp. 462 –474. ISSN: 0168-9002. DOI: http://dx.doi.org/10.1016/j.nima.2003.08.117. URL: http://www.sciencedirect.com/science/article/pii/S0168900203024331.

[Icr] *Stopping Powers for Electrons and Positrons*. International Commission on Radiation Units and Measurements. Report 37. Bethesda, MD, U.S.A., 1984.

[Szy+11] M. Szydagis et al. "NEST: A Comprehensive Model for Scintillation Yield in Liquid Xenon". In: *JINST* 6 (2011), P10002. DOI: 10.1088/1748-0221/6/10/P10002. arXiv: 1106.1613 [physics.ins-det].

[VOS83] Adriaan Van Oosterom and Jan Strackee. "The solid angle of a plane triangle". In: *IEEE transactions on Biomedical Engineering* 2.BME-30 (1983), pp. 125–126.

[Yam+06] K. Yamamoto et al. "Development of Multi-Pixel Photon Counter (MPPC)". In: *2006 IEEE Nuclear Science Symposium Conference Record*. Vol. 2. 2006, pp. 1094–1097. DOI: 10.1109/NSSMIC.2006.356038.

[Yan+14] Seul Ki Yang et al. “Precision measurement of the photon detection efficiency of silicon photomultipliers using two integrating spheres”. In: *Opt. Express* 22.1 (2014), pp. 716–726. DOI: 10.1364/OE.22.000716. URL: http://www.opticsexpress.org/abstract.cfm?URI=oe-22-1-716.

[Yia16] Liang Yiang. *Status and Prospects for the EXO-200 and nEXO Experiments*. Neutrino Conference 2016. [online; accessed September 08, 2016]. Imperial College London, July 2016. URL: http://neutrino2016.iopconfs.org/programme#Friday.

Acknowledgements

First of all, I would like to thank Prof Gisela Anton for the opportunity to write my Master thesis at the Erlangen Centre for Astroparticle Physics. It is a great institute with a lot of great people. Thank you also for your support with the application process for my PhD position!

A big thank you goes out to Thilo Michel for the support in difficult moments and for giving me the chance to turn my focus on a different topic when there was a dead end ahead.

I would like to thank Patrick Hufschmidt, Judith Schneider, Gerrit Wrede and the whole nEXO Erlangen group for all those great moments, funny stories and special events in and outside the office. I had so much fun working with you guys!

Thanks a lot to Michael Wagenpfeil, Ako Jamil and Tobias Ziegler for their help with final corrections and layout issues.

Thank you, Jason Brodsky, Caio Licciardy, Max Müller and Lev Classen for answering important questions on GEANT4! It would have been much more difficult without your help!

Thanks to all nEXO and EXO-200 collaboration members. It's a great community with high goals. Go for it!

Thank you Matthew Szydagis for answering questions on the NEST add-on and helping me making the code applicable for alpha particles in xenon gas. Also, thanks to Alexis Schubert for sorting out problems with photon numbers.

I would also like to thank Mrs Jutta Dziwis for being the most helpful and most friendly secretary one could imagine. Bureaucracy would be a much worse monster if we couldn't rely on your experience!

And thanks to Kay Graf for the help with IT issues, Henry Schott for his technical support and all his interesting stories, Clancy James the "runner", Thorsten Kühn for helping me repair my bike (twice!) and all the other ECAP members that I've been in contact with throughout the last year.

Thanks to Katharina Witzman for being the sunshine of the everyday office life.

A big thank you goes to all my friends and especially my family for the steady support in all life situations!

Thanks to my dear friends Simon Kreuzer, Julian Wechs and Markus Poetzsch for walking all the way with me from the first semester until today!

Thanks to all my dear British friends. It's been the time of my life!

Thanks to my band colleagues, my friends from VDSt and TSV 1846 Nuremberg Rugby. If I did one thing right, then it was spending my free time with you guys!

And thanks to Marci.

Declaration/Erklärung

Herewith, I declare that the present work was written exclusively by myself. No other but the cited literature and resources have been used.

Ich bestätige hiermit, dass ich die vorliegende Arbeit selbst verfasst und keine anderen als die angegebenen Quellen und Hilfsmittel verwendet habe.

Erlangen, Signature/Unterschrift: